STRUCTURED GROWTH OF ZINC OXIDE NANORODS ON PLASTIC OPTICAL FIBER AND LIGHT SIDE COUPLING TOWARDS SENSING APPLICATIONS

HAZLI RAFIS BIN ABDUL RAHIM

FACULTY OF ENGINEERING
UNIVERSITY OF MALAYA
KUALA LUMPUR

2017

STRUCTURED GROWTH OF ZINC OXIDE NANORODS ON PLASTIC OPTICAL FIBER AND LIGHT SIDE COUPLING TOWARDS SENSING APPLICATIONS

HAZLI RAFIS BIN ABDUL RAHIM

THESIS SUBMITTED IN FULFILMENT OF THE REQUIREMENTS FOR THE DEGREE OF DOCTOR OF PHILOSOPHY

FACULTY OF ENGINEERING
UNIVERSITY OF MALAYA
KUALA LUMPUR

2017

UNIVERSITY OF MALAYA

ORIGINAL LITERARY WORK DECLARATION

Name of Candidate: Hazli Rafis Bin Abdul Rahim (I.C No.: [redacted])

Registration/Matric No: KHA140007

Name of Degree: Doctor of Philosophy

Title of Thesis: Structured Growth of Zinc Oxide Nanorods on Plastic Optical Fiber and Light Side Coupling Towards Sensing Applications

Field of Study: Electronic (Engineering and Engineering Trades)

I do solemnly and sincerely declare that:

(1) I am the sole author/writer of this Work;
(2) This Work is original;
(3) Any use of any work in which copyright exists was done by way of fair dealing and for permitted purposes and any excerpt or extract from, or reference to or reproduction of any copyright work has been disclosed expressly and sufficiently and the title of the Work and its authorship have been acknowledged in this Work;
(4) I do not have any actual knowledge nor do I ought reasonably to know that the making of this work constitutes an infringement of any copyright work;
(5) I hereby assign all and every rights in the copyright to this Work to the University of Malaya ("UM"), who henceforth shall be owner of the copyright in this Work and that any reproduction or use in any form or by any means whatsoever is prohibited without the written consent of UM having been first had and obtained;
(6) I am fully aware that if in the course of making this Work I have infringed any copyright whether intentionally or otherwise, I may be subject to legal action or any other action as may be determined by UM.

Candidate's Signature Date:

Subscribed and solemnly declared before,

Witness's Signature Date:

Name:

Designation:

ABSTRACT

A simple and cost effective optical fiber sensor using side coupling of light into the core modes of plastic optical fiber (POF) coated with zinc oxide (ZnO) nanorods is reported here. Nanorods coating enhanced coupling inside the fiber by scattering light but were also capable of causing leakage. Structuring the growth to specific regions allowed scattering from different segments along the fiber to contribute to the total coupled power. A uniform, densed and highly aligned spiral patterned ZnO nanorods were grown on the POF using the hydrothermal method and its effect was investigated. ZnO nanorods growth time of 12 h and temperature of 90 °C provided the best coupling voltage. Side coupling was measured to be a factor of 2.2 times better for spiral patterned coatings as opposed to unpatterned coatings. The formation of multiple segments was used for multiple-wavelength channels excitation where different bands were side coupled from different segments. It was found that visible white light source significantly coupled the light into the POF compared with infrared laser sources. A first order theoretical model was derived to simulate the impact of millimeter (mm) scale spiral patterns on coupling efficiency by varying the width and spacing of the coated and uncoated regions. The width of spiral patterned ZnO nanorod coatings on POF was optimized theoretically for light side coupling and was found to be 5 mm. An experimental validation was performed to complete the optimization and the experimental results showing a well correlation with simulation. Optimized width of spiral patterned ZnO nanorods grown on large core POFs was used for the purpose of temperature and multiple optical channel alcohol vapor sensing. Spiral patterned ZnO nanorods coating exhibited a significant response to temperature change from 20 ˚C to 100 ˚C based on extinction concept which is the attenuation of light by scattering and absorption as it traverses the ZnO nanorods. Sensitivity was measured to be a factor of 1.3 times better for spiral patterned coatings as opposed to unpatterned coating. The multiple optical channel alcohol sensing mechanism

utilized changes in the output signal due to adsorption of methanol, ethanol and isopropanol vapors. Three spectral bands consisting of red (620-750 nm), green (495-570 nm) and blue (450-495 nm) were applied in measurements. The range of relative intensity modulation (RIM) was determined to be between 25 to 300 ppm. Methanol presented the strongest response compared to ethanol and isopropanol in all three spectral channels. With regard to alcohol detection RIM by spectral band, the green channel demonstrated the highest RIM values followed by the blue and red channels respectively.

ABSTRAK

Satu penderia optik yang mudah dan kos efektif menggunakan gandingan sisi cahaya ke dalam ragam-ragam teras gentian optik plastik (POF) disalut dengan zink oksida (ZnO) nanorods dilaporkan di sini. Salutan nanorod-nanorod mempertingkatkan gandingan dalam gentian oleh serakan cahaya tetapi juga boleh menyebabkan kebocoran. Penstrukturkan pertumbuhan ke kawasan-kawasan tertentu membolehkan penyerakan daripada ruas yang berbeza di sepanjang gentian yang menyumbang kepada jumlah kuasa terganding. Satu pilin corak ZnO nanorod yang seragam, tumpat dan terjajar dengan tinggi dan yang ditumbuhkan di atas teras POF menggunakan kaedah hidroterma dan kesannya disiasat. ZnO nanorod yang mempunyai masa pertumbuhan 12 jam dan suhu 90 °C telah menyediakan gandingan voltan terbaik. Gandingan sisi diukur dengan faktor sebanyak 2.2 kali lebih baik untuk lapisan pilin corak berbanding dengan lapisan tidak tercorak. Pembentukan berbilang ruas telah juga digunakan untuk pengujaan saluran-saluran pelbagai panjang gelombang di mana jalur-jalur digandingkan secara sisi daripada ruas yang berbeza. Didapati sumber cahaya putih boleh nampak dengan ketara menggandingkan cahaya ke dalam POF berbanding dengan sumber laser infra-merah. Satu model teori tertib pertama diterbitkan untuk menyelakukan kesan corak-corak pilin berskala milimeter (mm) terhadap kecekapan gandingan dengan mengubah lebar dan jarak kawasan bersalut dan tidak bersalut. Lebar lapisan corak pilin ZnO nanorod pada POF teras telah dioptimumkan secara teori untuk gandingan sebelah cahaya dan didapati 5 mm adalah lebar tersebut. Satu pengesahan ujikaji telah dilakukan untuk melengkapkan pengoptimuman dan keputusan ujikaji menunjukkan satu hubungan sekaitan yang baik dengan penyelakuan. Lebar corak pilin ZnO nanorod yang ditunbuhkan atas POF teras besar telah digunakan untuk penderiaan suhu dan wap alkohol pelbagai saluran optik. Lapiran pilin corak ZnO nanorod mempamerkan satu tindak balas yang ketara kepada perubahan suhu dari 20 ˚C hingga 100 ˚C berdasarkan konsep pemupusan yang

merupakan pengecilan cahaya oleh serakan dan penyerapan apabila ia merentasi ZnO nanorod. Kepekaan diukur yang menunjukan faktor 1.3 kali lebih baik untuk lapiran corak pilin yang bertentangan dengan lapiran tidak bercorak. Mekanisme penderiaan wap alkohol pelbagai saluran optik telah menggunakan perubahan-perubahan di dalam isyarat keluaran disebakan oleh penyerapan wap-wap methanol, etanol dan isopropil. Tiga jalur spektrum terdiri daripada merah (620-750 nm), hijau (495-570 nm) dan biru (450-495 nm) telah digunakan dalam pengukuran ini. Julat nisbi pemodulatan keamatan ditentukan antara 25 hingga 300 ppm. Metanol menunjukkan tindakbals yang kuat berbanding etanol dan isopropil dalam ketiga-tiga saluran spektrum. Dengan mengambil kira nisbi pemodulatan keamatan pengesanan alkohol oleh jalur spektrum, saluran hijau menunjukkan nilai nisbi pemodulatan keamatan tertinggi diikuti dengan masing-masing oleh saluran biru dan merah.

ACKNOWLEDGEMENTS

It is with immense gratitude that I would like to acknowledge the support and help of my supervisor, Prof. Dr. Sulaiman Wadi Bin Harun. He has been a source of inspiration and has convincingly conveyed a spirit of adventure in regard to research. The initial ideas he suggested and his vast knowledge on optical sensor were invaluable in helping me get set on the right track. The successful completion of my task would not have been possible without his constant encouragement and guidance throughout the whole period of my research work.

I am also indebted to my co-supervisor Prof. Dr. Waleed S. Mohammed who helped me in building up a positive work attitude. His mastery over the subject and the freedom he provided in carrying out my research were instrumental in gaining a lot of confidence. I owe my deepest gratitude to Prof. Dr. Louis Gabor Hornyak, Director of Center of Excellence in Nanotechnology, Asian Institute of Technology (AIT), Bangkok, Thailand and Prof. Dr. Joydeep Dutta, Chair of Functional Materials division, KTH Royal Institute of Technology, Stockholm, Sweden for reading my reports, commenting on my views and helping me understand and enrich my ideas.

I share the credit of my work with Mr. Manjunath, PhD student, Bangkok University, Thailand and Siddharth Thokchom, master student, Assam Don Bosco University, India for their constant involvement and inspiring advice.

Most importantly, I would like to express my heart-felt gratitude to my parents Abdul Rahim and Hasnah, thank you for your encouragement and prayers. My deepest appreciations from bottom of my heart go to my wife Siti Khatijah for all your love and support, and to our children Rayyan and Rayqal for being such as wonderful sons.

Lastly, I would like to thank Universiti Teknikal Malaysia Melaka (UTeM) and Ministry of Higher Education Malaysia (MOHE) for sponsoring my PhD program under SLAB/ SLAI scholarship.

TABLE OF CONTENTS

Abstract iii

Abstrak v

Acknowledgements vii

Table of Contents viii

List of Figures xii

List of Tables xviii

List of Symbols and Abbreviations xix

List of Appendices xxii

CHAPTER 1: INTRODUCTION 1

1.1 General 1

1.2 The Role of Nanotechnology in Optical Sensor 2

1.3 Problem Statement 4

1.4 Hypothesis 5

1.5 Objectives of the Study 6

1.6 Limitation of the Study 6

1.7 Organization of the Thesis 7

CHAPTER 2: LITERATURE REVIEW 9

2.1 Introduction 9

2.2 Optical Fiber 10

2.3 Plastic Optical Fiber (POF) 13

2.3.1 Optical Properties of POF 14

2.3.2 Mechanical Properties of POF 15

2.3.3 Thermal Properties of POF 17

2.3.4 Chemical Infiltration 18
2.4 Optical Sensor Using Plastic Optical Fiber 19
2.4.1 Optical Loss 20
2.4.2 Interferometry-Based Sensors 22
2.4.3 OTDR, OFDR and Scattering 24
2.4.4 Fiber Bragg Grating (FBG) 25
2.5 Zinc Oxide Nanorod-Structure 25
2.6 Hydrothermal Synthesis Method of Zinc Oxide Nanostructure 29
2.7 Zinc Oxide in Global Applications 34
2.8 Light Scattering and Side Coupling 37
2.9 Recent Research on Temperature and Gas Sensing Using Optical Fiber 46

CHAPTER 3: OPTIMIZATION OF ZINC OXIDE NANOROD COATINGS ON LARGE CORE PLASTIC OPTICAL FIBER THROUGH HYDROTHERMAL GROWTH……..... 50

3.1 Introduction 50
3.2 Optimization parameters for the hydrothermal method 51
3.3 ZnO Nanorods through Hydrothermal Growth 52
3.3.1 Fiber Preparation 53
3.3.2 Seeding Process 54
3.3.3 ZnO Nanorod Growth Process 59
3.4 Optimization of ZnO Nanorod Growth on POF 60
3.4.1 Spiral Patterned Growth of Zno Nanorods on POF Using the Optimized Growth Duration. 69
3.5 Optimization of Seeding Methods to Improve the Growth of Zno Nanorods on POF…. 72
3.6 Summary 76

CHAPTER 4: CHARACTERIZATION OF LIGHT SIDE COUPLING TOWARDS MULTIPLE OPTICAL CHANNEL AND OPTIMIZATION OF SPIRAL PATTERNED WIDTH OF ZINC OXIDE NANOROD COATING FOR OPTIMAL SIDE COUPLING 78

4.1 Introduction 78

4.2 Mechanism of Light Scattering by ZnO Nanorod 80

4.3 Mechanism of Light Scattering For Unpatterned and Spiral Patterned ZnO Nanorod Layers and For the Multi-Channel Optical Fiber 81

4.4 Experimental Characterization of Multi-Channel Optical Fiber towards Light Side Coupling 84

4.5 Modeling of Coupling Efficiency for Spiral Patterned and Unpatterned Coating by Varying the Width of the Coated Region towards Light Side Coupling 86

4.6 Theoretical Optimization of Spiral Patterned Width for Optimal Side Coupling . 93

4.7 Experimental Optimization of Spiral Patterned Width for Optimal Side Coupling…. 99

4.8 Summary 102

CHAPTER 5: APPLIED LIGHT SIDE COUPLING WITH OPTIMIZED SPIRAL PATTERNED ZINC OXIDE NANOROD COATINGS FOR TEMPERATURE AND MULTIPLE OPTICAL CHANNEL ALCOHOL VAPOR SENSING 104

5.1 Introduction 104

5.2 SEM images of Optimized Spiral Patterned Zinc Oxide Nanorod Coatings for Sensing Applications 105

5.3 Applied Light Side Coupling With Optimized Spiral Patterned Zinc Oxide Nanorod Coatings for Temperature Sensing 107

5.3.1 Experiment of Temperature Sensing 109

5.3.2 Results and Discussions 110

5.4 Applied Light Side Coupling With Optimized Spiral Patterned Zinc Oxide Nanorod Coatings for Multiple Optical Channel Alcohol Vapor Sensing. 113

5.4.1 Experiment of Multiple Optical Channel for Alcohol Vapor Sensing ... 114

5.4.2 Results and Discussions 117

5.5 Summary 125

CHAPTER 6: CONCLUSION AND FUTURE WORK 127

6.1 Conclusion 127

6.2 Future work 129

References 130

List of Publications, Papers Presented And patents 147

Appendix 151

LIST OF FIGURES

Figure 2.1 Some applications of optical fiber sensors in industry (Rajan, 2015) 10

Figure 2.2 The parts of optical fiber..... 11

Figure 2.3 Phenomena of light refraction and reflection inside optical fiber. 12

Figure 2.4 (a) Multimode and (b) single mode 13

Figure 2.5 Attenuation loss of common POF as a function of wavelength (Zubia & Arrue, 2001) 15

Figure 2.6 The measurement of true stress versus strain for single-mode PMMA-doped core (Kiesel et al., 2007) 16

Figure 2.7 The results of Dynamic Young's modulus for PMMA MPOF, step index POF and silica SMF28 (Stefani, Andresen, Yuan, & Bang, 2012) 17

Figure 2.8 The responses of two POF FBG sensors with RH varied from 80% to 70% at a temperature of 25°C (W. Zhang, Webb, & Peng, 2012) 19

Figure 2.9 Schematic of POF-based accelerometer. The inset shows a magnification of the fiber gap region. (Antunes et al., 2013)..... 21

Figure 2.10 (a) Schematic of VCO interrogator used for time-of-flight measurements and (b) Image of upper side of aircraft flap with POF adhered to surface and prototype instrumentation. (Gomez et al., 2009)..... 23

Figure 2.11 Wurtzite structure of ZnO..... 26

Figure 2.12 3D ZnO structures (a) nanorods (Dedova et al., 2007), (b) nanowires (Shan et al., 2008), (c) nanoflowers (Miles et al., 2015) and (d) snowflakes (Jing et al., 2012). 28

Figure 2.13 Growth morphologies of ZnO 1D nanostructures. (Z. L. Wang, 2004) 29

Figure 2.14 SEM images of ZnO nanostructures grown with different aqueous solutions of pH value of (a) 1.8, (b) 4.6, (c) 6.6, (d) 9.1, (e) 10.8 and (f) 11.2. (Amin et al., 2011) 30

Figure 2.15 SEM images of ZnO nanorods on Si substrate with different precursor concentrations of the growth aqueous solution (a) at 25 mM, (b) 50 mM, (c) 100 mM, (d) 300 mM. (Amin et al., 2011)..... 31

Figure 2.16 SEM image of ZnO nanorods grown using $Zn(NO_3)_2$ and HMT (Baruah & Dutta, 2008) 34

Figure 2.17 Various applications of ZnO (Kołodziejczak-Radzimska & Jesionowski, 2014) 35

Figure 2.18 Illustration of light scattering from one ZnO nanorod..... 38

Figure 2.19 Schematic representation of two possible configurations of side coupling to cladding modes with guided and leakage intensity responses of light paths in the side coupling configuration (H Fallah et al., 2013)..... 39

Figure 2.20 Optical characterization setup for the light side coupling (Hoorieh Fallah et al., 2014)..... 41

Figure 2.21 The coupling intensity of different concentration of zinc acetate for ZnO nanorods grown on wet etched optical fiber (H Fallah et al., 2013)..... 42

Figure 2.22 The measurement of coupling intensity (y- left axis), the average scattering coefficient (y- right axis) and versus the concentration of zinc acetate (H Fallah et al., 2013) 43

Figure 2.23 The coupling intensity for cladding mode and core mode at different excitation location on the optical fiber (Hoorieh Fallah et al., 2014) 44

Figure 2.24 Optical nephelometer setup for testing scattering properties of ZnO grown on glass substrate (Hoorieh Fallah et al., 2014)..... 45

Figure 2.25 The measurement of (a) normalized angular power spectra and (b) density, ρ_a respect to the concentrations of zinc acetate used for preparing the ZnO seed layer on glass substrate (Bora et al., 2014) 46

Figure 2.26 The setup of liquid temperature sensor. (S. Kumar & Swaminathan, 2016) 47

Figure 2.27 Optical fiber sensor based on SPR for chemical sensing. (Michel et al., 2016) 49

Figure 3.1 Optimization parameters for the ZnO nanorods growth on POF using hydrothermal method 51

Figure 3.2 General procedures of ZnO nanorods synthesis using hydrothermal..... 52

Figure 3.3 The process of fiber preparation (a) POF with black jacket (b) POF is exposed with length of 10 cm for ZnO coating (c) 3M water proof tape is used to create spiral template (d) manually creating spiral pattern on POF and (e) POF with spiral template before the synthesis process. 53

Figure 3.4 Procedures of seeding process on POF..... 54

Figure 3.5 Process of 1mM ZnO nanoparticle solution preparation 55

Figure 3.6 Preparation of the pH controlled solution using NaOH 55

Figure 3.7 Alkaline process of ZnO nanoparticles solution by NaOH 56

Figure 3.8 (a) Tween 80 preparation and (b) POF surface treatment 57

Figure 3.9 Dip and Dry method in seeding process 57

Figure 3.10 Drop and Dry method in seeding process 58

Figure 3.11 Slow stirring method in seeding process 59

Figure 3.12 The process of ZnO nanorod growth on POFs 60

Figure 3.13 Flow of the optimization process of ZnO nanorod growth on POF through hydrothermal 61

Figure 3.14 Low magnification SEM images of the POF coated with ZnO nanorods with (a) surface treatment (Tween 80) and (b) without surface treatment 62

Figure 3.15 V_{pp} characterisation setup to measure the side coupling of ZnO nanorods for unpatterned and spiral patterned POFs 62

Figure 3.16 The modulated LED red light source used in the optical characterization .. 63

Figure 3.17 The exposed regions on the unpatterned type of POF (a) interface, (b) middle and (c) tip 64

Figure 3.18 Average V_{pp} for 15 and 20 hours growth time with backscattering effects. 65

Figure 3.19 ZnO nanorods grown on POF (a) 15 hours (b) 20 hours 65

Figure 3.20 Backscattering effect is eliminated at interface regions after reducing the growth time to 8, 10, and 12 hours 66

Figure 3.21 Average V_{pp} at interfacial area for all growth times 67

Figure 3.22 The SEM images for growth durations: 8 hours (top left), 10 hours (top right) and 12 hours (bottom) 68

Figure 3.23 The specified regions on the spiral patterned POF for optical characterization. 69

Figure 3.24 Average Vpp for the spiral patterned growth for 12 h which has more than one interface and ZnO regions. The inset shows the regions covered by the aperture when characterisation the structured and unstructured ZnO growth on POF 70

Figure 3.25 (a) 13 kX SEM image of ZnO spiral patterned growth after synthesis (b) 25.0 kX SEM image of the nanorods and Inset: The ZnO nanorods at 60.0 kx magnification for 12 hours 71

Figure 3.26 EDX spectrum of ZnO nanorods showing zinc and oxygen peaks 72

Figure 3.27 The growth of ZnO nanorods using the drop and dry method (a) 5 kX SEM image of spiral patterned growth on POF and (b) the morphology of ZnO nanorods at a high magnification 73

Figure 3.28 Schematic diagram showing the possible agglomeration of ZnO nanoparticles upon evaporation of the solvent (a) thin layer of ZnO nanoparticles (b) agglomerated clumps of ZnO nanoparticles with various orientations and (c) ZnO nanorods grow from the seed crystallites in the different directions 74

Figure 3.29 The continuous slow stirring process 75

Figure 3.30 The growth of ZnO nanorods using the continuous slow stirring method (a) 5 kX SEM image of spiral patterned growth on POF and (b) the morphology of ZnO nanorods at 10.0 kX 76

Figure 4.1 Mechanism of light scatters into POF by ZnO nanorods at angle larger than critical angle, θ_c 80

Figure 4.2 Schematic diagram of light scattering for (a) Unpatterned growth of ZnO nanorods with the coupling light (b) Spiral patterned growth of ZnO nanorods with more interface and ZnO regions with the coupling light (c) Spiral patterned growth of ZnO nanorods for a multi-channel excitation 82

Figure 4.3 Spectral analysis setup to determine wavelength coupling maxima 84

Figure 4.4 Transmittance of the visible white light spectrum 85

Figure 4.5 Spectrum for near infrared (850 and 980 nm) for spiral patterned and unpatterned growth 86

Figure 4.6 (a) Spirally patterned coating of ZnO nanorods on POF and (b) unpatterned coating of ZnO nanorods on POF with a visible light source 87

Figure 4.7 Definition of polar coordinate 88

Figure 4.8 (a) Dividing the POF coated with ZnO nanorods into discrete sections of width Δz for both coating schemes (b) Optical Intensity components around a segment h of the ZnO coated POF 90

Figure 4.9 The scheme of light propagation for unpatterned continuous and spiral patterned coating where ZnO coating region was fixed to 3 segments (3 mm) 92

Figure 4.10 The normalized coupling output for unpatterned and spiral patterned coating by varying the width of ZnO nanorod coating on POFs 94

Figure 4.11 (a) Spirally patterned coating of ZnO nanorods on POF and (b) unpatterned coating of ZnO nanorods on POF with a laser light source (Gaussian beam) 96

Figure 4.12 The coupling efficiencies for spiral patterned and unpatterned coating excited by a laser light source 97

Figure 4.13 Spiral patterned coating of ZnO nanorods (b) unpatterned coating of ZnO nanorods with varied uncoated spacing 98

Figure 4.14 The effects on coupling efficiency by varying the uncoated region 99

Figure 4.15 Coating schemes (a) unpatterned POFs (b) Spiral patterned POFs 100

Figure 4.16 Optimization setup to measure the output voltage for unpatterned and spiral patterned ZnO nanorods 101

Figure 4.17 The experimental result of spiral patterned and unpatterned coating for 3, 5, 7 and 100 mm 102

Figure 5.1 (a) The optimized spiral patterned ZnO nanorod coatings, (b) the perpendicular growth of ZnO nanorods on POF at low magnification (c) at high magnification (d) hight and diameter of the ZnO nanorod and (e) ZnO continuous coating on unpatterned POF 106

Figure 5.2 Experimental setup for the proposed temperature sensor towards light side coupling 110

Figure 5.3 The response of spiral patterned coating and unpatterned coating in temperature sensing 111

Figure 5.4 The temperature sensing mechanism (a) before light illumination (b) upon light illumination and (c) aluminum rod in close proximity to ZnO nanorods coating layer. 112

Figure 5.5 The sensitivity of spiral patterned and unpatterned coating in temperature sensing 113

Figure 5.6 Experimental setup to validate the alcohol sensing activities of spiral patterned POF as multiple optical channels 115

Figure 5.7 Spectroscopy responses of multiple optical channels sensor in blue, green, and red wavelengths for (a) methanol, (b) ethanol and (c) isopropanol 118

Figure 5.8 Schematic diagram of the alcohol sensing mechanism activated using visible white light illumination (a) in air at room temperature (b) with visible white light and (c) with methanol exposure 120

Figure 5.9 The responses of multiple optical channels sensor in channel (a) blue (b) green and (c) red 121

Figure 5.10 The relative intensity modulation (RIM) of multiple optical channels sensor exposed to ethanol, methanol and isopropanol vapors..... 123

Figure 5.11 The validation of the multiple optical channels sensor for (a) channel blue/ channel red (b) channel green/ channel red..... 124

LIST OF TABLES

Table 2.1 Properties of Zinc Oxide 27

Table 4.1 Differences of normalized coupling output, ΔI between spiral patterned and unpatterned POFs for different widths of ZnO coating from 0 to 7 mm 95

LIST OF SYMBOLS AND ABBREVIATIONS

˚C	:	Degree Celsius
µm	:	Micrometer
nm	:	Nanometer
cm	:	Centimeter
g	:	Gram
mM	:	Mili mole
C_2H_5OH	:	Ethanol
CH_3OH	:	Methanol
C_3H_8O	:	Isopropanol
$C_6H_{12}N_4$	:	Hexamethylenetetramine
HCL	:	Hydrochloric acid
CO	:	Carbon monoxide
O_2	:	Oxygen
CO_2	:	Carbondioxide
H_2O	:	Water
NaOH	:	Sodium hydroxide
ZAH	:	Zinc acetate hydrate
$Zn(CH_3COO)_2$	:	Zinc acetate
$Zn(NO_2)_3$	:	Zinc Nitrate hexahydrate
$Zn(OH)_2$	:	Zinc hydroxide
$ZnCl_2$	:	Zinc chloride
ZnO	:	Zinc oxide
Zn^{2+}	:	Zinc ions
O^{2-}	:	Oxygen ions

OH^-	:	Hydroxyl ions
dB/km	:	Decibels/kilometer
V_{pp}	:	Peak-to-peak Voltage
σ	:	Beam waist
r	:	Distance from the center of the beam
C_{sc}	:	Scattering cross section
ρ_a	:	Rods density
ψ	:	Portion of Scattered Light
θ_{inc}	:	Incident angle
θ_c	:	Critical angle
Δz	:	Width of Segment
η_z.	:	Coupling coefficient
I_p	:	Coupling output of spiral pattern
I_{up}	:	Coupling output of unpatterned
n	:	Refractive index
ΔI	:	Normalized coupling output
ϕ	:	Azimuthal angle

HMT	:	Hexamethylenetetramine
MMF	:	Multimode Fiber
SOF	:	Silica Optical Fiber
OFSs	:	Optical Fiber Sensors
POF	:	Plastic Optical Fiber
AI	:	Artificial intelligence
PMMA	:	Polymehyl Methacrylate

SEM	:	Scanning Electron Microscope
LED	:	Light Emitting Diode
FBG	:	Fiber Bragg Grating
DI	:	Deionized
DC	:	Direct Current
1D	:	One Dimensional
2D	:	Two Dimensional
3D	:	Three Dimensional
ZAH	:	Zinc Acetate Hydrate
EDX	:	Energy-dispersive X-ray
SPR	:	Space Plasmon Resonance
RH	:	Relative Humidity
CTOP	:	Specialty Amorphous Fluorinated Polymer
DMA	:	Dynamic Mechanical Analysis
MPOF	:	Multimode Plastic Optical Fiber
OTDR	:	Optical Time-Domain Reflectometry
OFDR		Optical Frequency-Domain Reflectometry
VCO	:	Voltage-Controlled Oscillator
RI	:	Refractive Index
IR	:	Infrared
VZn	:	Zinc Vacancies
ca.	:	Around, about or approximately
RIM	:	Relative Intensity Modulation
GOF	:	Glass Optical Fiber

LIST OF APPENDICES

Publications and Papers Presented

Patent Filing Reports

CHAPTER 1: INTRODUCTION

1.1 General

Historically, the early research on optical fiber sensors (OFSs) was started in the 70s and related to medical instrument that was such as a fiber-optic endoscope consisting of a bundle of flexible glass fibres able to coherently transmit an image (Edmonson, 1991). Nowadays, various approaches and technologies have been developed to gain attention in sensing applications. Optical sensors using fiber optics definitely provide reliable solutions in many fields since optical fibers can measure physical properties such as strain (Ohno, Naruse, Kihara, & Shimada, 2001), displacement (Rahman, Harun, Yasin, & Ahmad, 2012), temperature (Tyler et al., 2009), pressure (W. Wang, Wu, Tian, Niezrecki, & Wang, 2010), velocity (Weng et al., 2006) and magnetism (Lv, Zhao, Wang, & Wang, 2014). Every year, exploring the potentials of OFSs keep receiving high interest because optical fibers offer well known advantages such as immunity to electrical and magnetic fields, low attenuation, wide transmission bandwidth, small physical size and weight, increased flexibility, analog and digital transmission, electrical insulation, immunity to electromagnetic interference and interception and receiver sensitivity. Beside these properties, FOSs also hold enormous potential for the use in chemical applications due to the high sensitivity and slightly invasive technique (Mescia & Prudenzano, 2013) which is important in monitoring environmental pollution, mainly if FOSs are applied in radiation zone.

This thesis is concerned with the development of a simple and cost effective system based on light scattering from zinc oxide (ZnO) nanorods grown in spiral pattern on plastic optical fiber (POF) for temperature and alcohol vapors sensing applications. The performance of the system is investigated based on the simulation and experimental

results. Artificial intelligence (AI) is suggested as an efficient technique for improving the capability of the sensor system.

1.2 The Role of Nanotechnology in Optical Sensor

Recently, interest in integrating OFSs with nanotechnology anonymously received global demands to increase sensitivity, repeatability, selectivity and stability of their performances. Nanotechnology literally means the ability to manipulate individual atoms and molecules to produce nanostructured materials and submicron objects that has applications in the real world. According to National Science Foundation and National Nanotechnology Initiative (NNI) (H. Chen et al., 2013), nanotechnology involves the production and application of physical, chemical and biological systems at scales ranging from individual atoms or molecules to about 100 nm, as well as the integration of the resulting nanostructures into larger systems with fundamentally new properties and functions because of their small structure. Nano-systems include micro/ nano-electromechanical systems (MEMS/NEMS), micro-mechatronics, optoelectronics, micro-fluidics and systems integration. These systems can sense, control and activate on the micro/nano-scale and can function individually or in arrays to generate effects on the macro-scale. Nanotechnology plays an important role in fabrication of sensors. Its usage leads to new findings for the mechanism of reactions as well as fabrication of new types of sensors.

Zinc oxide has gained substantial interest in the research community in part because of its versatile wide-bandgap (3.37eV) semiconductor material that has contributed to the development of numerous applications over the past few years. Depending on its doping condition, ZnO can be conductive (including n-type and p-type conductivity), semi-conductive, insulating, transparent and show piezoelectric behavior, room temperature ferromagnetism, and huge magneto-optic and chemical sensing

properties (Kołodziejczak-Radzimska & Jesionowski, 2014). The paramount importance is the transparency of ZnO to visible light that is in part responsible for exploring this material for optoelectronics applications (Janotti & Van de Walle, 2009; Pauporté & Lincot, 2000; Shinde, Shinde, Bhosale, & Rajpure, 2008; Xiang et al., 2007), biosensors (Chang et al., 2010; T. Kong et al., 2009; S. A. Kumar & Chen, 2008), resonators (Cao et al., 1998), medical devices (Rasmussen, Martinez, Louka, & Wingett, 2010), imaging (Zvyagin et al., 2008) and wireless communication (J. Chen, Zeng, Li, Niu, & Pan, 2005).

As a rule, the optical signal in gas sensor arises from the interaction of gas molecules with an incident electromagnetic radiation, which can take place at all frequency and wavelength ranges. Every gas has specific properties and therefore has specific interaction with electromagnetic radiation. This means that the results of these interactions can be used for gas molecule identification. It was found that various methods can be used for gas analysis (Sberveglieri, 2012). However, absorption spectroscopy is still one of the most commonly used methods in optical gas sensing (Kraft, 2006). It has been established that for many applications and absorption spectroscopic detection is a reliable method of detecting various gases. Recently, the method has been widely used by coating optical fiber with ZnO for detection of gases such as oxygen, O_2 (Vanheusden, Seager, Warren, Tallant, & Voigt, 1996), carbon dioxide, CO_2 (Samarasekara, Yapa, Kumara, & Perera, 2007), ammonia, NH_3 (Aslam et al., 1999) and methane, CH_4 (Bhattacharyya, Basu, Saha, & Basu, 2007).

Generally, temperature measurement systems are very important for many industries and according to World Health Organization (WHO), the impact of climate and temperature on health has been receiving increased attention in recent years. Accurate and continuous temperature monitoring is a critical task for a wide variety of industries. Controlling temperature levels is needed to eliminate harmful bacteria in cooking (McWilliams & Lamb, 1994), cooling (Schmidt & Notohardjono, 2002), storing

(Seaman, 1997), shipping, displaying and production (Sugaya et al., 2002). From food processing to medical applications, even a single degree can affect the quality of products, reaction rate of molecules and health. Due to these demands, research on temperature sensors continues to grow rapidly in order to improve the quality of life.

1.3 Problem Statement

Over the years, a bulk of the work has been done on the synthesis of ZnO nanorods on flat surface such as metal, plastic and glass substrates (X. Wang, Summers, & Wang, 2004). The growth of ZnO on these flat surfaces promises a high guarantee for easily controlling the morphological parameters such as alignment, density and uniformity. In addition, the synthesis of ZnO nanorods on these flat surfaces typically promotes extensive growth using hydrothermal method which involves a simple aqueous solution at temperature below the boiling point of water compare with gas phase synthesis (Ayouchi, Martin, Leinen, & Ramos-Barrado, 2003). Various ZnO nanorod structures have been synthesized on these flat surfaces such as 1D nanorods (S. Xu & Wang, 2011), 2D nanoplate (Giri et al., 2015) and 3D nanoflowers (Wahab, Kim, Mishra, Yun, & Shin, 2010). However, patterned growth of ZnO nanorods on cylindrical surfaces with small diameter such as optical fiber still remains an issue for optical sensing applications. Commonly, unpatterned growth is preferable to do due to less time consumption and reducible complexity for fabrication. Hence, there are many research reports about the unpatterned growth of ZnO nanorods on POF for sensing applications (Baruah, K Pal, & Dutta, 2012; Batumalay et al., 2014) but the backscattering of light occurs due to the high density of ZnO nanorods presents all over the exposed core. Although the unpatterned growth of ZnO nanorods enhances optical guidance in optical fiber, it is also responsible for light leakage due to the very same scattering property (Hoorieh Fallah, Harun, Mohammed, & Dutta, 2014). Consequently, these two situations have resulted low

coupling power which is undesirable in sensing applications. This open up the possibilities in exploring new approach to increase the coupling power and minimize backscattering from ZnO nanorods coating.

The work behind this research was initiated from the need to develop a low-cost, high sensitivity and an uncomplicated sensor system. Generally, most optical sensing applications are operated with laser light source by launching light from one end of the optical fiber and output signal is collected from other end (Aneesh & Khijwania, 2011). This is surely expensive and needs other mechanical supports to align properly the laser beam into the fiber. Applying laser source onto ZnO nanorods coating to utilize scattering of light into POF provided also less sensitivity caused by the inequality of beam structure which has different distribution of intensity along the ZnO coating (Dickey, Weichman, & Shagam, 2000) and the laser beam only focuses on specific coating area instead of entire coating area. With this background and abstraction, a research work is needed to provide another alternative of light source towards light side coupling applications. This research work certainly can bring contribution to many fields such as in optoelectronics, telecommunication and material engineering.

1.4 Hypothesis

1. ZnO crystal is transparent in the visible wavelength range and acts as a waveguide for light.
2. Higher coupling of optical power for the patterned coating on POF than the unpatterned coating.
3. Spiral pattern of ZnO nanorods showing a uniform decay and providing higher coupling power.
4. Simple and efficient device as an optical transducer for sensing applications.

1.5 Objectives of the Study

The main objective of this research study is to investigate the possibility of the use of a simple and inexpensive sensing device towards light side coupling using plastic optical fiber. The following sub objectives have to be met:

1. To optimize the synthesis process of ZnO nanorods growth on POF using hydrothermal method.
2. To fabricate spiral patterned ZnO nanorods coating on POF using hydrothermal method.
3. To optically characterize and optimize the spiral patterned ZnO nanorods coating on POF using light side coupling method.
4. To develop a new theoretical model in analysing the width of spiral patterned ZnO nanorod coating on POF for achieving maximum coupling.
5. To validate experimentally the sensing of spiral patterned ZnO nanorods coating on POF.

1.6 Limitation of the Study

As the growth of ZnO nanorods were performed on a cylindrical surface of an optical fiber the alignment as well as the distribution of the nanorods was an issue and the fibers needed to be handled carefully. Also the fragile nature of the fibers made it prone to breakage during fiber preparation and structuring. Achieving a uniform structuring of the fibers using the plastic tape was difficult and had to be done accurately. The hydrothermal process being a low temperature process, the crystal growth rate was low and the duration of growth took more than ten hours to obtain the optimized ZnO nanorod morphology. Due to low POF thermal specification (< 100 ˚C), temperature effects on physical POF should be considered in synthesis process and sensing applications.

1.7 Organization of the Thesis

The thesis is organized into six chapters, each of which is then subdivided into sections and subsections. **Chapter 1** presents an introduction of this work comprising the background study, statement of the problem, hypothesis, objectives of the research and limitations of the study. In **Chapter 2,** the theoretical review of related research including a thorough study on the optical fiber technology, its types and designs and the implementation of optical fiber as an optical sensor will be presented. The chapter will also discuss the structures of ZnO nanorod and the hydrothermal growth process. The global applications of ZnO nanorods in various fields is also given. A detailed study on the previous work of light side coupling into an optical fiber and its potential application as an optical sensor will be presented. The last part of this chapter gives an overview of recent research on temperature and gas sensing using optical fiber.

Chapter 3 will explain in detail the two main procedures in chemically growing ZnO nanorods on POF and the implementation of it is presented by describing the materials and methods involved. The physical and optical characterization utilized for analyzing the structure of the ZnO nanorods and for optimizing the growth duration and seeding method for maximum side coupling is also presented in this chapter. **Chapter 4** will discuss the characterization results of light side coupling for spiral patterned and unpatterned coatings using spectra analysis. Second part will present a new theoretical model of light side coupling to analyze the width of spiral patterned ZnO nanorod coating on POF for maximum side coupling. An experimental validation was performed using light side coupling method for different width of spiral ZnO nanorods coating and the results are compared to the modelling in order to optimize the width of spiral patterned ZnO nanorod coating on POF.

Chapter 5 will discuss and analyze two sensing applications of spiral patterned ZnO nanorods coating on POF using light side coupling. First, temperature sensing was carried out by varying temperature from 20 ˚C to 100 ˚C. Second, the sensor probe was used as multiple optical channel for alcohol vapors sensing in visible wavelength. The performances of the optical sensor were analyzed in three particular channels: blue (450 – 495 nm), green (495 – 570 nm) and red (620 – 750 nm). The results are presented in graphs to compare the relative intensity modulation (RIM) of the sensing. Finally, in **Chapter 6** the conclusions are drawn and the future works to improve the proposed technique are suggested.

CHAPTER 2: LITERATURE REVIEW

2.1 Introduction

In the past several decades since the invention of the laser in 1960 (Maiman, 1960) and the development of modern low-loss optical fibers in 1966, optical fiber technology has made a transition from the experimental stage to practical applications (K. Grattan & Sun, 2000) . The main focus of the development of optical fiber has always been on telecommunications, but the early 1970s saw some of the first experiments on low-loss optical fibers being used for sensing purposes (Sathitanon & Pullteap, 2007). The field of optical fiber sensing has continued to progress and has developed enormously since that time. Magnetic (Dandridge, Tveten, Sigel, West, & Giallorenzi, 1980), pressure (Budiansky, Drucker, Kino, & Rice, 1979; Hocker, 1979; Lagakos & Bucaro, 1981), temperature (Yariv & Winsor, 1980), acceleration (Arditty, Papuchon, & Puech, 1981), displacement, fluid level, current (Dandridge, Tveten, & Giallorenzi, 1981; Tangonan, Persechini, Morrison, & Wysocki, 1980), and strain optical fiber sensors (Giallorenzi et al., 1982) were among the first few types extensively investigated and explored for sensing and measurement. For instance, distributed fiber-optic sensors have now been installed in bridges and dams as shown in Figure 2.1 to monitor the performance and structural damage of these facilities. OFSs are used to monitor the conditions within oil wells and pipelines, railways, wings of airplanes and wind turbines. Compared with other types of sensors, optical fiber sensors exhibit a number of advantages, such as immunity to electromagnetic interference, applicability in high-voltage or explosive environments, a very wide operating temperature range, multiplexing capabilities, and chemical passivity (B. Lee, 2003).

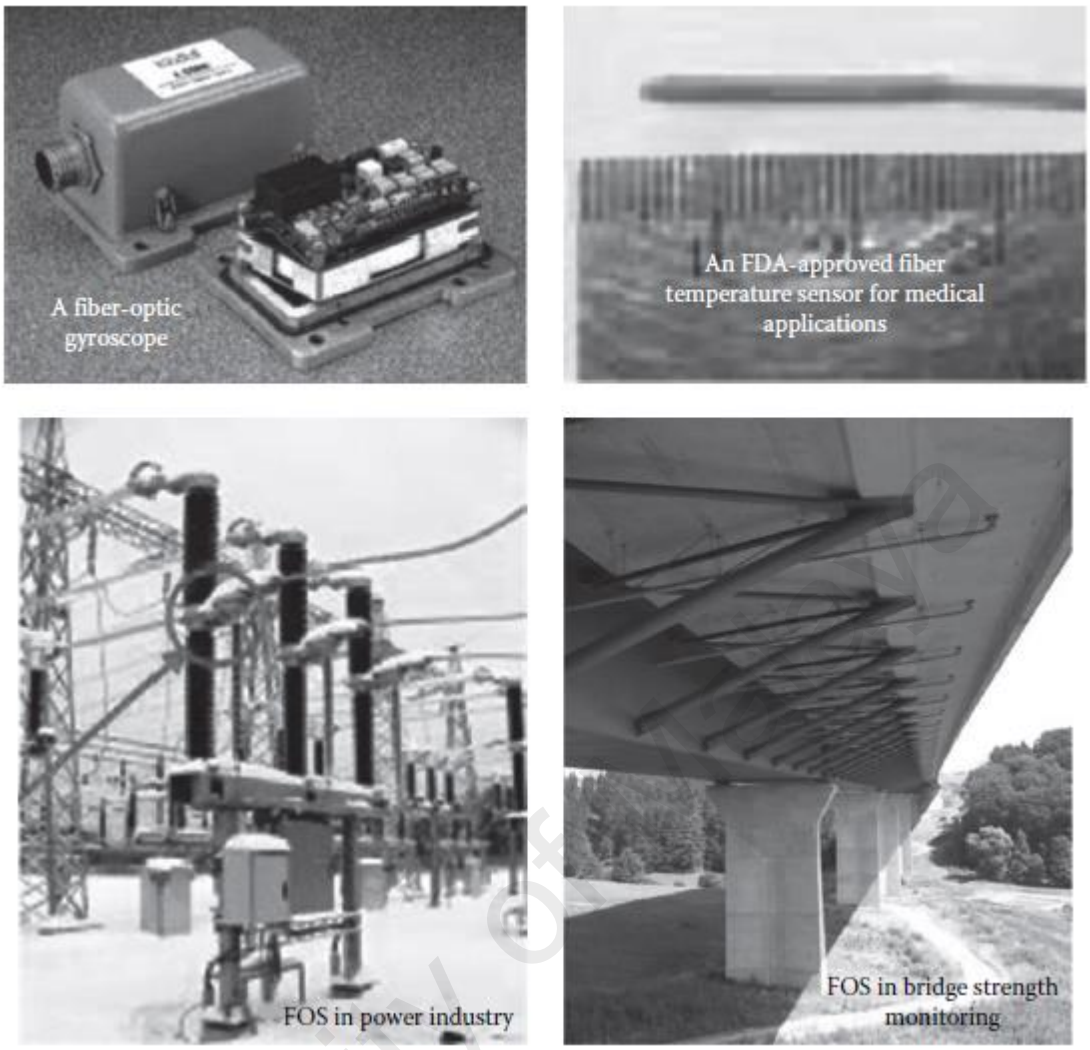

Figure 2.1 Some applications of optical fiber sensors in industry (Rajan, 2015)

2.2 Optical Fiber

Generally, an optical fiber consists of a core, cladding, buffer and jacket as illustrated in Figure 2.2 (J.-R. Lee, Dhital, & Yoon, 2011). Light travels through a material and it is called the core. The core is surrounded by a dark material called the cladding which reflects back any light that escapes the core. Finally, a plastic coating called the buffer around each cladding protects the fiber from wear and tear. Hundreds or thousands of these fibers are placed together in one cable protected by an outside covering called the jacket.

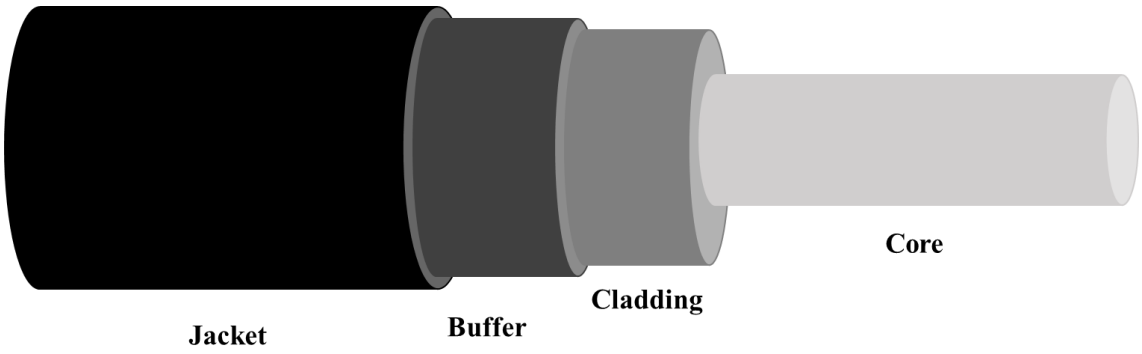

Figure 2.2 The parts of optical fiber

The core and cladding of the fiber is composed of highly pure solid glass. A protective layer then surrounds the cladding. In most of the optical fibers this protective layer is made up of multilayer composition. The protective layer can be comprised of two layers: a soft inner layer that cushions the fiber and allows the coating to be stripped from the glass mechanically and a harder outer layer that protects the fiber during handling and termination process (Kao, 1983). From the context of optical waveguiding it is clear that there should be a variation of refractive index inside the fiber between the core and the cladding. Therefore, the core and cladding are made up of two slightly different materials which are transparent to light over the operating wavelength. To achieve the phenomenon of total internal reflection which is the driving principle behind the operation of optical fibers the core has a higher refractive index than the cladding.

The application of both reflection and refraction is used in the operation of a fiber optic cable. When light falls on a shiny or mirrored surface it bounces off while when it travels from one medium to another having different thickness or density it bends. The bending depends on the angle at which light strikes the surface. At certain angle whole of the light is reflected in the original medium completely. This phenomenon is called total internal reflection which is the principle of operation of optical fiber (Cherin, 1983; Hentschel, 1983; Keiser, 2000). Figure 2.3 shows the critical angle which is the minimum angle required for light to reflect in the first medium completely. For all those angles greater than the critical

angle light rays will be totally internally reflected in the first medium. Therefore, when a light ray is sent into the fiber, it is sent at an angle towards the side of the fiber that will reflect.

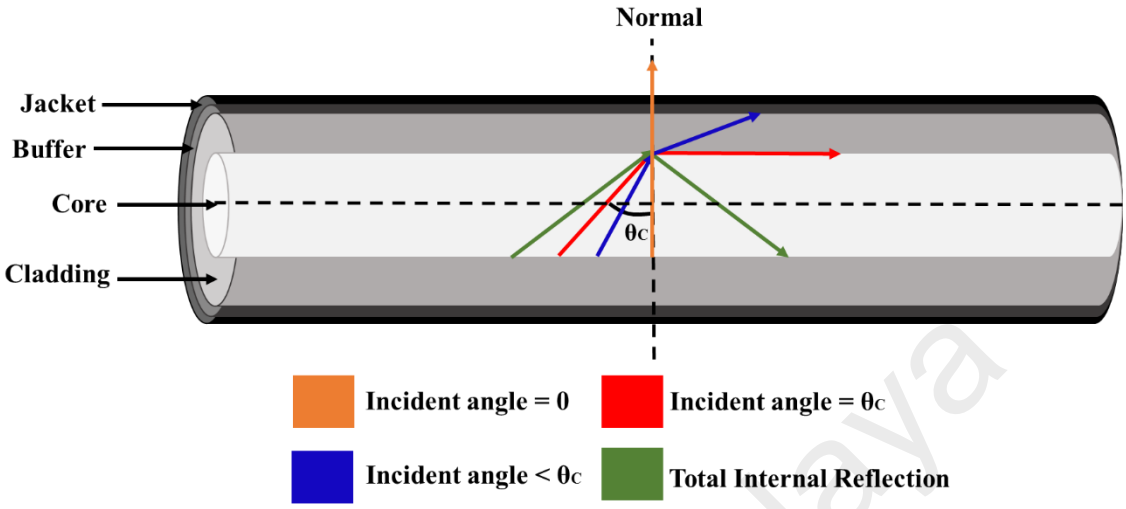

Figure 2.3 Phenomena of light refraction and reflection inside optical fiber.

There are generally two types of optical fibers: single mode and multimode as depicted in Figure 2.4 (Lacy, 1982). The multimode fibers have a larger core than the single mode fibers and it allows hundreds of modes of light to propagate through it. The larger core diameters of multimode fibers facilitate the use of lower cost optical transmitters such as light emitting diode (LED) and connectors. The single mode fibers on the other hand has a much smaller diameter than the multimode fibers and allows only one mode also called as the fundamental mode to pass through it. Single mode fibers are designed to maintain spatial and spectral integrity of each optical signal over longer distances, allowing more information to be transmitted. Its tremendous information carrying capacity and low intrinsic loss have made single mode fiber the ideal transmission medium for a multitude of applications (Jeunhomme, 1983). Single mode fiber is typically used for longer distance and higher bandwidth applications. Multimode fiber is used primarily in systems with short transmission distances (under 2km) such as premises communications, private data networks and parallel optic applications.

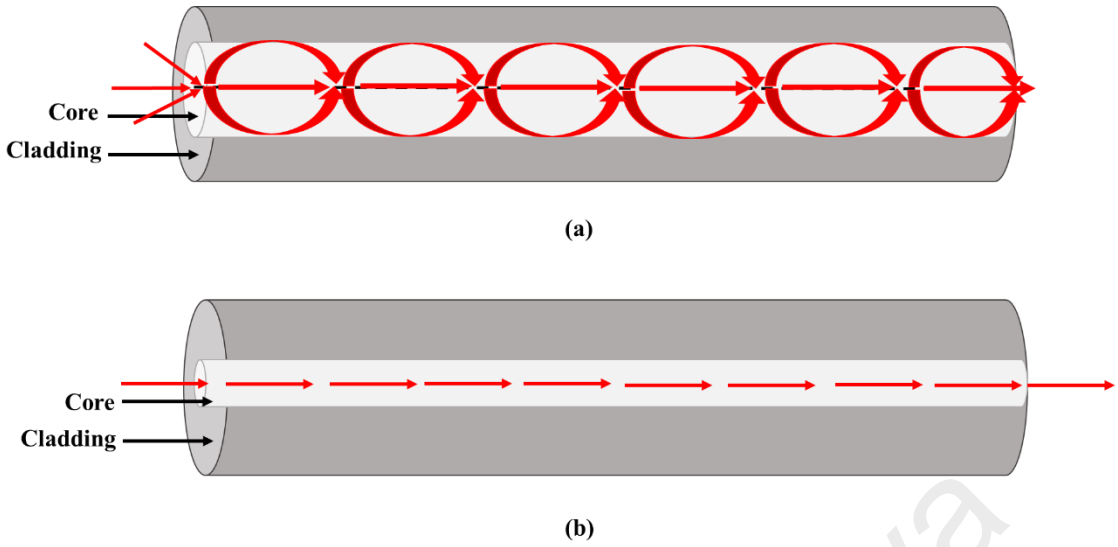

Figure 2.4 (a) Multimode and (b) single mode

2.3 Plastic Optical Fiber (POF)

Commonly, OFSs are based on silica optical fibers (SOFs) due to their wide use in telecommunication applications and the high availability of components, equipment and optical fiber specifications. Nowadays, POFs have practically experienced a stream in applications for short distance telecommunication systems. Many researchers have noticed their unique properties for sensing of strain, temperature, humidity, gas etc. Simultaneously, researchers are also developing POFs with new properties including single-mode fibers (Woyessa, Fasano, et al., 2016) and micro-structured fibers (Cordeiro et al., 2006). These unique properties have been utilized to expand the range of sensing applications beyond those previously realized with SOF sensors. There are several great advantages of POF over SOFs, including their large elastic and plastic strain deformation capabilities (Kiesel, Peters, Hassan, & Kowalsky, 2007), negative thermal sensitivities (Peters, 2010), high numerical aperture (Ishigure, Horibe, Nihei, & Koike, 1995) and lower stiffness (Rothmaier, Luong, & Clemens, 2008). Typically, POF materials include polymethyl methacrylate (PMMA), polystyrene (PS) and amorphous fluorinated polymer (CYTOP) (Olaf Ziemann, Krauser, Zamzow, & Daum, 2008a). Commercially, POFs are

typically available in multimode at their operating wavelength due to the challenges in its fabrication. As a result, these POFs are low cost and easier to cut and connects as compared to single mode SOFs. In market, multimode POFs are available with different cross-sectional index distributions, including both step index and gradient index configurations. Moreover, a large variety of POF diameters are available which are larger than conventional single-mode silica optical fibers. Due to the large core diameter (0.25mm-1mm) connectivity issues also does not rise, reducing the total cost of the system.

2.3.1 Optical Properties of POF

Figure 2.5 presents the intrinsic attenuation loss of common POF as a function of wavelength. In applications, multimode POF sensor are commonly operated in three different wavelengths; the visible wavelength range (400–700 nm) where the intrinsic attenuation is low, near 850 nm where common telecommunication and low-cost components are available and the near-infrared range (above 1300 nm) where the specialty amorphous fluorinated polymer (CTOP) has low attenuation. At all wavelengths, the intrinsic attenuation of POF materials are significantly higher than that of SOF.

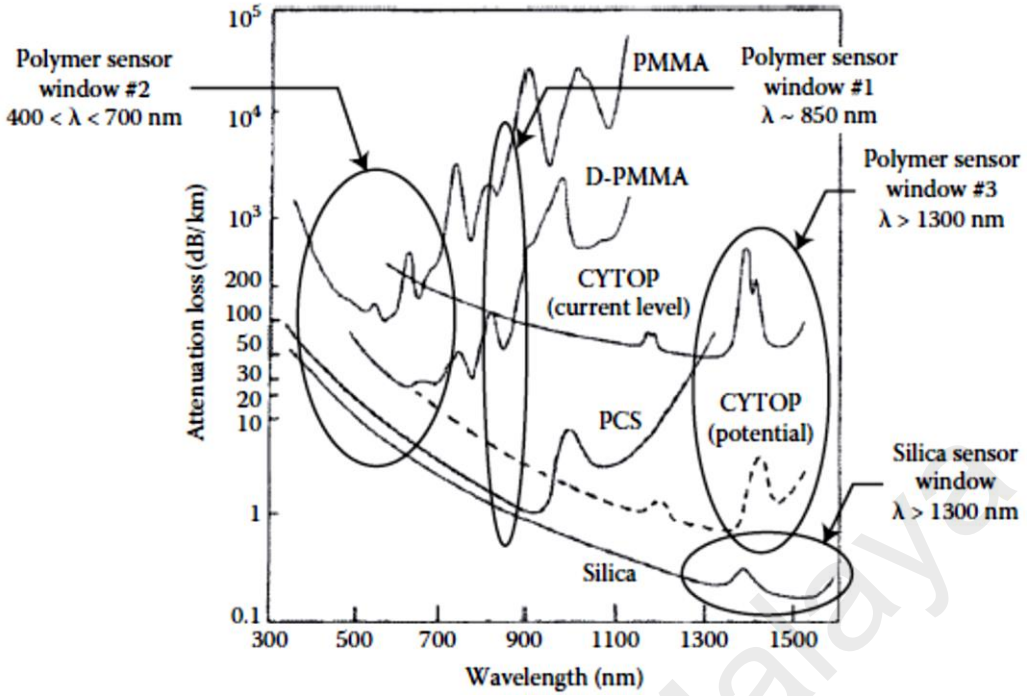

Figure 2.5 Attenuation loss of common POF as a function of wavelength (Zubia & Arrue, 2001)

2.3.2 Mechanical Properties of POF

The mechanical properties of POFs are highly influenced by the fiber manufacturing process and dopant concentration that is used to increase the core index of refraction (Bosc & Toinen, 1993; Jiang, Kuzyk, Ding, Johns, & Welker, 2002). Due to the annealing process to remove internal residual stresses and anisotropy in polymer during manufacturing process, the mechanical and thermal behavior of a specific POF is critical to calibrate prior to its use as a sensor. The mechanical properties of POFs are also dependent upon loading condition and affected by environmental conditions such as high temperature and humidity (O Ziemann, Daum, Bräuer, Schlick, & Frank, 2000; Olaf Ziemann, Krauser, Zamzow, & Daum, 2008b). Figure 2.6 shows the measurement of true stress (MPa) versus strain (%) for a PMMA optical fiber. POF properties characteristically fall in the ranges of initial elastic modulus of 1 to 5 GPa, yield strain of

1%–6% and ultimate strains of 6%–100% as compared to 1%–5% for SOFs (Hayashi, Mizuno, & Nakamura, 2012).

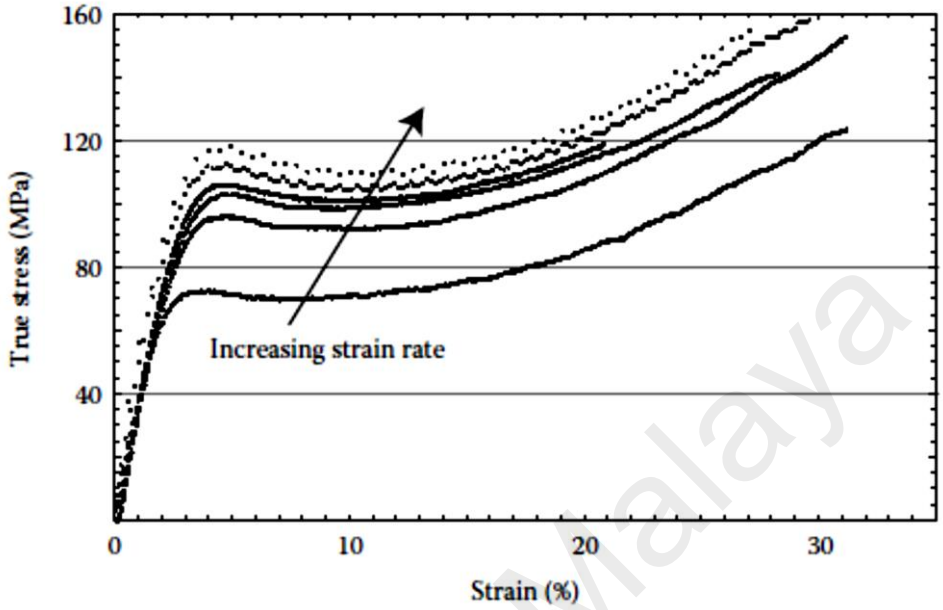

Figure 2.6 The measurement of true stress versus strain for single-mode PMMA-doped core (Kiesel et al., 2007)

It was reported that the yield strain and initial stiffness of the material are both a function of the applied strain rate. Moreover, the material behavior is nonlinear beyond the yield strain and therefore the loading history is also critical to predict hysteresis and cyclic behavior of the material. When POFs were strained beyond their yield limit, plastic deformation occured in the fiber, resulting in a residual deformation even when the fiber was unloaded. For sensing applications, this residual deformation can be considered a shape memory effect that can store the maximum strain information to be extracted later (Hayashi et al., 2012). PMMA also has a lower density (1195 kg m−3) than silica (2200 kg m−3), reducing the weight of distributed optical fiber sensors (van Eijkelenborg et al., 2001).

Second, dynamic mechanical analysis (DMA) was reported to reveal the dependence of the material behavior on applied loading rates by applying cyclic loads to

the materials at different frequencies. Young's modulus at different frequencies can be obtained from DMA. Young's modulus starting from 7 Hz was observed in different frequency responses for a solid POF, a micro-structured POF and a SOF for comparison as shown in Figure 2.7. As compared to the silica fiber, it was presented that the lower Young's modulus at low frequencies of the polymer materials and the start of a frequency-dependent modulus at lower frequencies in the polymer materials.

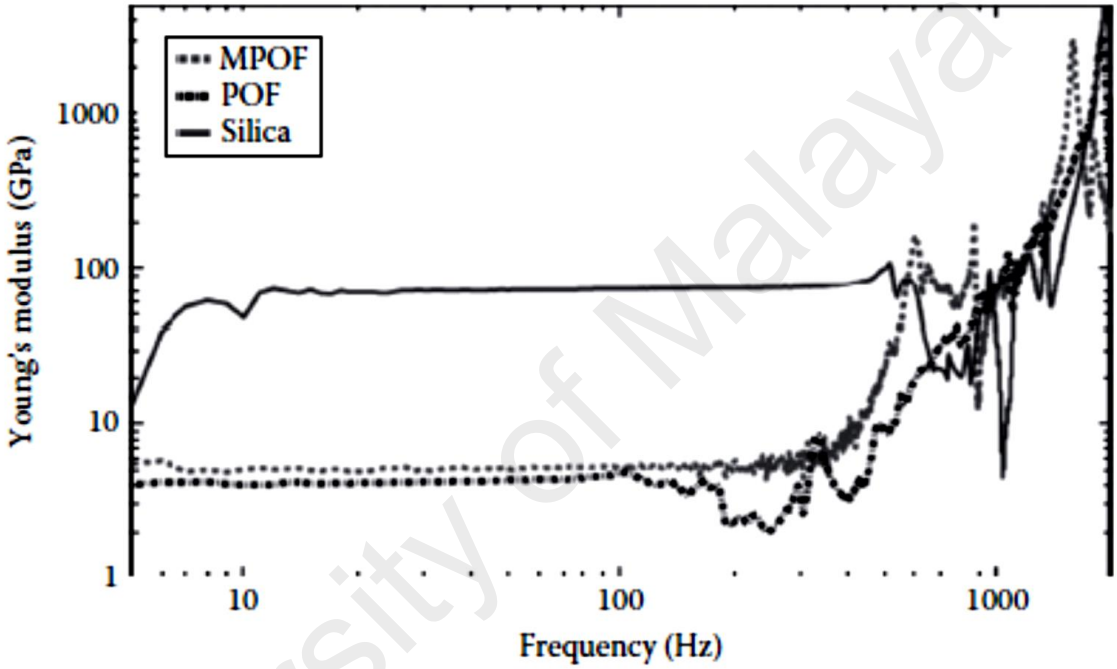

Figure 2.7 The results of Dynamic Young's modulus for PMMA MPOF, step index POF and silica SMF28 (Stefani, Andresen, Yuan, & Bang, 2012)

2.3.3 Thermal Properties of POF

The temperature sensitivity of POF was defined to be the phase shift per unit change in temperature per unit length of the POF. Typically, the thermal sensitivity of bulk PMMA is -154.3 rad/m/k (Silva-López et al., 2005). As for SOF, the intrinsic temperature response of a POF must be a known variable for temperature compensation of strain measurements. For instance, strain temperature cross talk in a multimode POF of 33 με/ ˚C (J. Huang et al., 2012). Recent research has also reported the coupling

between the response of the POF to the temperature and humidity. The coefficient of thermal expansion (COT) of POF is approximately -1×10^{-4}/ °C and SOF is 5×10^{-7}/ °C. A report found that when relative humidity (RH) is accurately controlled as temperature is varied, the COT is nonlinear with temperature (Z. F. Zhang & Tao, 2013).

2.3.4 Chemical Infiltration

The inherent performance of POFs to absorb moisture can also make them sensitive to chemical infiltration. In a previous work, the effect of vinyl ester and epoxy resins on the integrity were measured using signal transmission of perfluorinated POFs embedded in these resin systems as sensing applications (Hamouda, Peters, & Seyam, 2012). The more investigation of the two resin systems, vinyl ester was penetrated into the POF during curing of the resin, resulting a significant increase in backscattering level in the POF and eventual signal transmission loss. Figure 2.8 shows the visible change in the POF cross section before and after exposure to the vinyl ester resin.

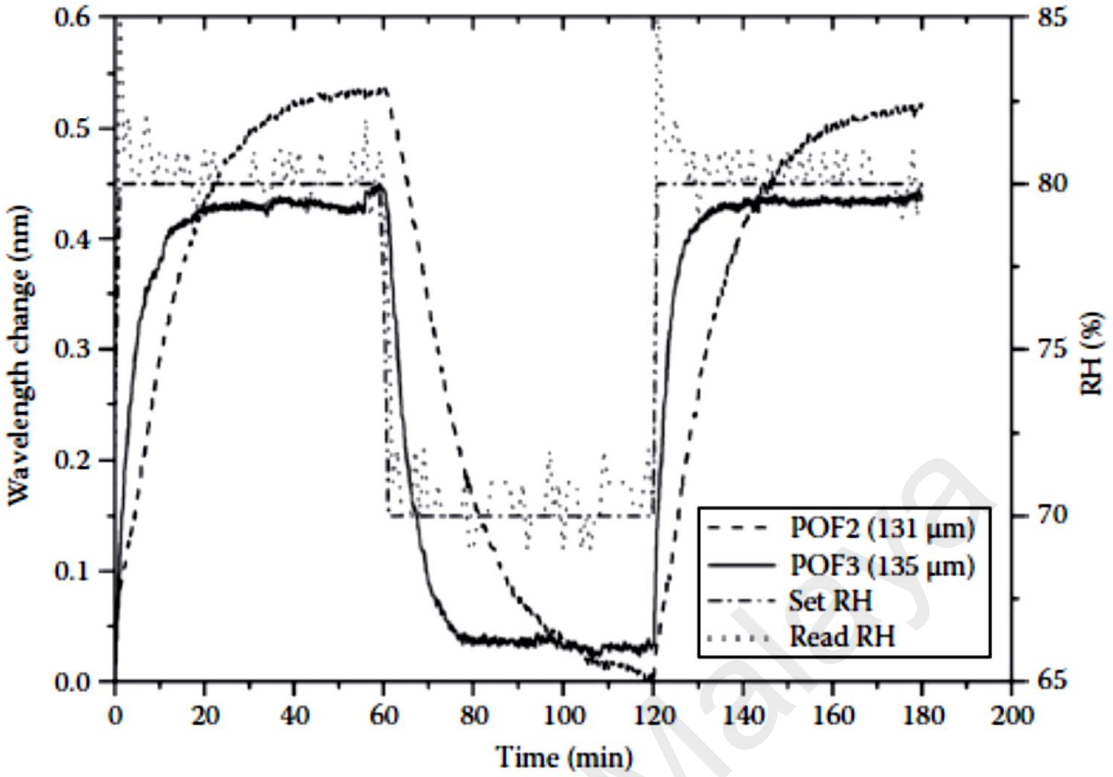

Figure 2.8 The responses of two POF FBG sensors with RH varied from 80% to 70% at a temperature of 25°C (W. Zhang, Webb, & Peng, 2012)

In contrast, the epoxy resin did not penetrate the POF during cure, giving no increase in backscattering level. POF3 (135µm) shows a faster response more closely following the humidity change.

2.4 Optical Sensor Using Plastic Optical Fiber

POFs provides a low cost and efficient medium to be used as sensors. The sensors fabricated using POF has potential applications in the field of medicine, environment, chemical and biological area. Conventional POFs are used to make sensors for measuring distance, position, shape, color, brightness, opacity, density, turbidity etc. Sophisticated sensors that are used for particle tracking are made possible with the development of fluorescent POFs. The studies of POF based sensors were started in early 70s and they were first implemented in medical and industrial field (Fischer, Haupt, Reinboth, & Just, 2015). Wide area research has been going on already for the production of improved versions of

POF based sensors to be used in applications where the traditional systems cannot apply. Also the entire operating principle is based on optical domain and there is absolute immunity to electromagnetic and radio frequency interference. The sensors are grouped by the particular sensing mechanisms that they use to convert the physical parameters into properties of propagating lightwaves which includes optical loss, optical time-domain reflectometry (OTDR) (Liehr, Lenke, et al., 2009; Liehr, Nöther, & Krebber, 2009; Liehr, Wendt, & Krebber, 2010), optical frequency-domain reflectometers (OFDR), scattering and long period grating (Banerjee et al., 2003; Peters, 2010). POF based sensors are frequently used in structural health monitoring, medicine and in environmental applications (Witt, Schukar, & Krebber, 2008; Yokota, Okada, & Yamaguchi, 2007).

2.4.1 Optical Loss

A simple and low cost POF-based sensor is typically based on the measurement of optical power losses. Commercially, the cost of such sensor is low because multimode POF is usually preferable and inexpensive light sources can be used compare to SOF. Moreover, a simple photodetector is required to convert the optical fiber power transmitted the optical fiber into a voltage output. Figure 2.9 shows an example of POF accelerometer based on the transfer of lightwaves between two multimode POFs (Antunes, Varum, & Andre, 2013).

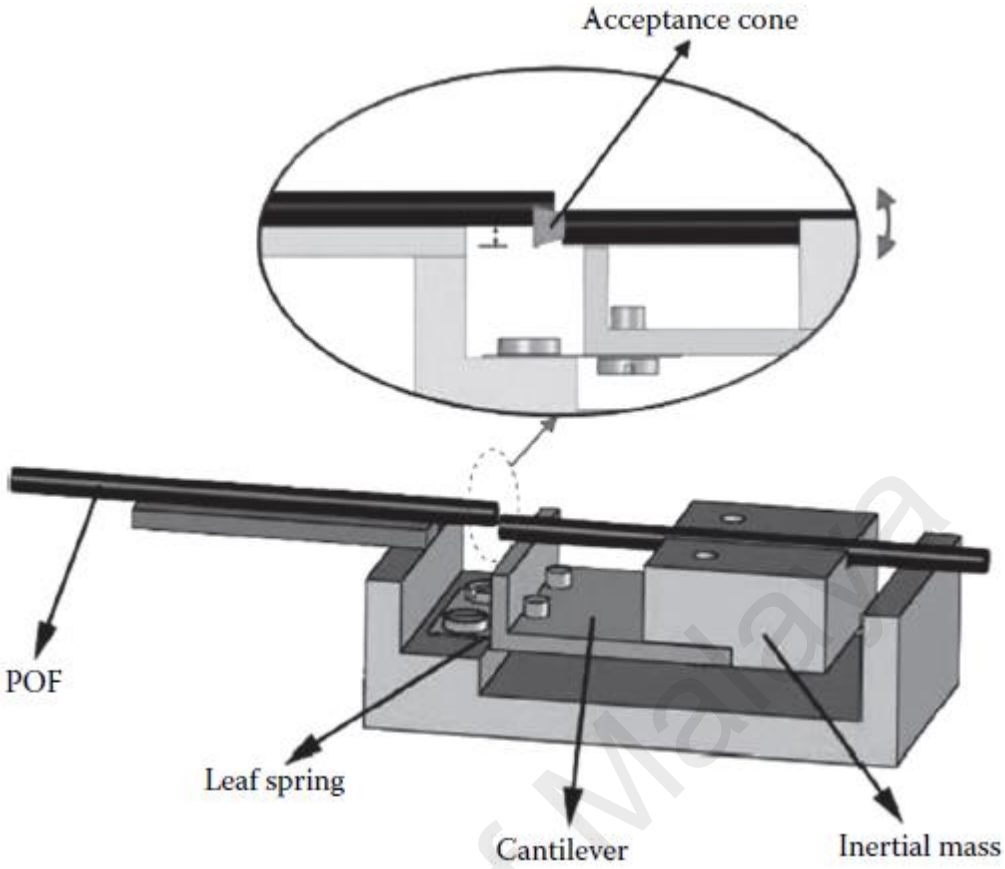

Figure 2.9 Schematic of POF-based accelerometer. The inset shows a magnification of the fiber gap region. (Antunes et al., 2013)

In the setup, one POF was fixed to the inertial frame and the other moved with the object whose acceleration is to be measured. Acceleration of the object moved the POF mounted on the cantilever beam in a direction parallel to the cross section, creating a coupling loss into the sensor fiber. This accelerometer offers some advantages which are low cost, ease of fabrication and small size. Therefore, the accelerometer provides the low resolution inherent in the power coupling measurements.

The measurement of power losses can be implemented by creating bending losses in the POF using the geometry of U-shaped POF sensor. In the experiment, the radius of the curved portion is well controlled such that the bending losses are repeatable in the POF. By changing the index of refraction of a fluid external to the POF, the fraction of light coupled into the surrounding fluid is changed. Therefore, this low-cost sensors can

be applied as a liquid level sensor such as fuel level monitoring (Montero, Lallana, & Vázquez, 2012). The advantage here is that the optical sensor does not create a spark hazard near the fuel.

2.4.2 Interferometry-Based Sensors

The time of flight interferometer takes advantage of low cost and ease of use of multimode POFs. Due to an incoherent interferometer configuration, it does not require phase measurement. For some structural applications, it is sufficient to measure the integrated strain along the POF. The time-of-flight measurement system provides sufficient displacement resolution for a full-scale structure. In previous works, time-of-flight measurements was applied to monitor the global displacement of a vibrating aircraft wing flap (Durana et al., 2009; Gómez et al., 2008). Figure 2.10 shows a diagram of the voltage-controlled oscillator (VCO)-driven interrogator along with a photograph of the aircraft flap with the surface mounted sensor POF. The interrogator is entirely constructed of low-cost telecommunication components. The system is also portable and durable and has relatively low power requirements. The measurement displacement range is determined by the oscillator modulation frequency and can be quite large compared to other interrogation methods.

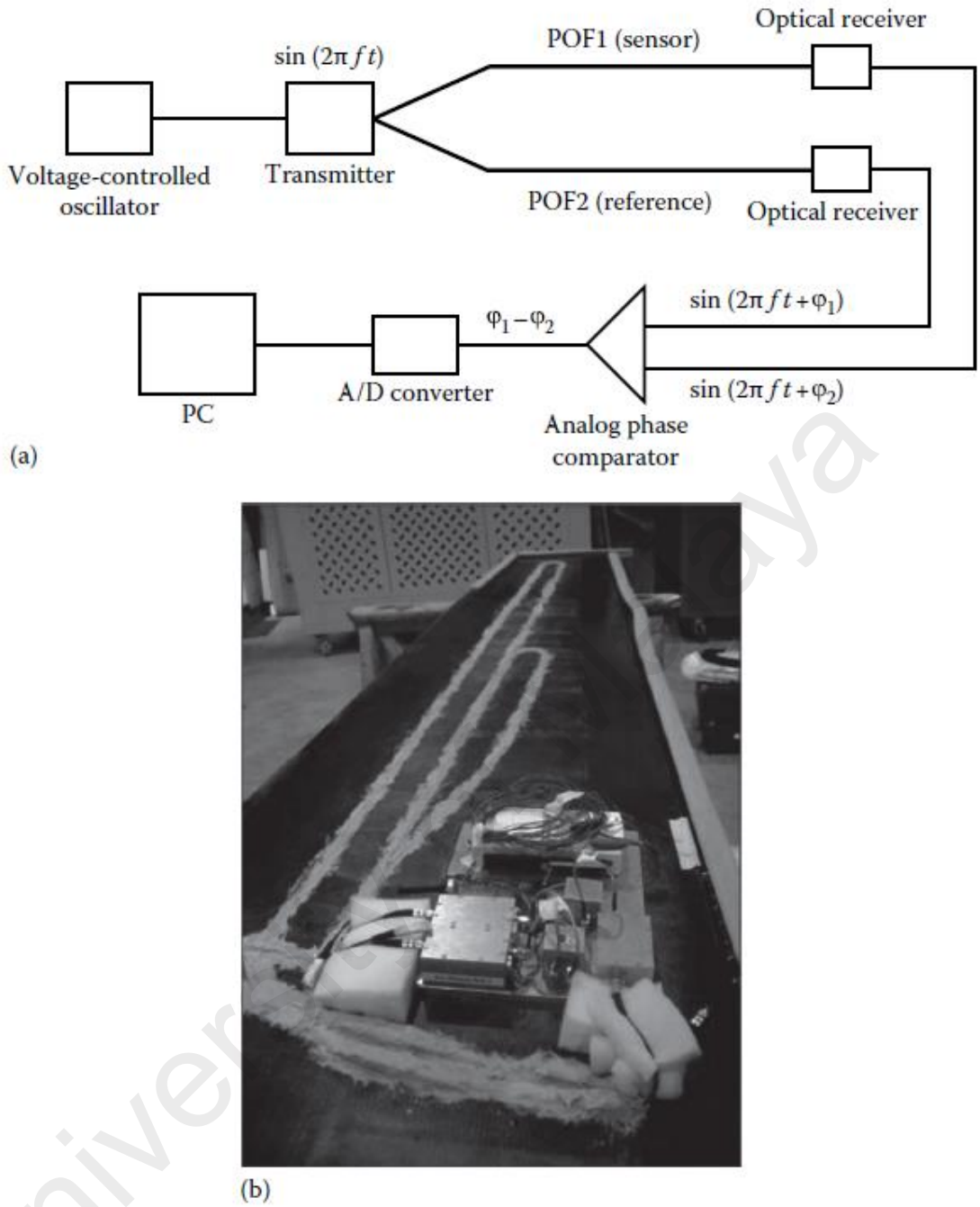

Figure 2.10 (a) Schematic of VCO interrogator used for time-of-flight measurements and (b) Image of upper side of aircraft flap with POF adhered to surface and prototype instrumentation. (Gomez et al., 2009)

2.4.3 OTDR, OFDR and Scattering

Recently, several researches have also demonstrated POF-based sensor by exploiting the unique properties of POF. The nonlinear stress–strain behavior of POFs at large strain values as shown in Figure 2.6 is encoded along the POF and can be measured through the scattering or other loss profiles along the POF, for example, through OTDR (Liehr, Lenke, et al., 2009). In the work, multimode POFs with large diameter is embedded into geotextiles for the monitoring of geotechnical and masonry structures. The geotextiles were embedded in a railway embankment for monitoring of soil displacements. The large core diameter allowed easy connection to handling of the sensors at the construction site, while the use of the standard POF itself as the sensor permitted monitoring of a large area at low cost. In addition, the high ultimate strain of the PMMA allowed the POF to elongate with the large soil deformations. The OTDR measurements were limited by the attenuation and dispersion characteristics of the POF. Replacing the POF with a low loss, graded-index perfluorinated POF (PF-GIPOF) significantly improved both the measurement resolution and maximum fiber length, up to 500 m, as a result of the reduced dispersion and attenuation in the fiber. The resolution and speed of such measurements can also be enhanced by applying incoherent OFDR rather than OTDR (Liehr & Krebber, 2012). The authors demonstrated OFDR measurements along a POF at 2 kHz data acquisition rates with high spatial resolution on the order of a few micrometers. The POF signal was sensitive to large strain magnitudes; therefore, this technique was applied to the measurement of seismic induced strains (up to 125%).

2.4.4 Fiber Bragg Grating (FBG)

FBG sensors are one of the most widely applied silica optical fiber sensors as they can provide local sensing information and can be multiplexed in large numbers along a single optical fiber. In addition, the fact that the sensing information is wavelength encoded means that it is invariant to fluctuations in laser power and coupling losses. Based on this success, numerous researchers have developed techniques to inscribe FBGs in POFs with the motivation to exploit the large tuning range of POF FBGs as compared to those in silica optical fibers. One demonstration that highlights the unique properties of FBGs in POFs is that of high-sensitivity pressure measurements to detect small pressure changes. In 2013, FBG POF was used as pressure sensor (Rajan, Liu, Luo, Ambikairajah, & Peng, 2013). The cladding of the POF was etched to significantly reduce the cladding diameter. Combining the low elastic modulus of the polymer and small cladding diameter produced an FBG with high sensitivity to small axial loads on the POF. The authors then attached the POF to a vinyl diaphragm to transfer the surrounding pressure to an axial force on the POF and demonstrated a complete sensor with the extremely high pressure sensitivity of 1.32 pm Pa^{-1} over the range of 0.1–5.0 kPa. Challenges still are present in the application of POF FBG sensors. Some of these challenges come from the inherent properties of the POF, including the low maximum temperature threshold and viscoelastic strain response (Peters, 2010). In addition, thermal erasing of POF FBGs can occur when the grating is exposed to thermal loads for extended periods of time.

2.5 Zinc Oxide Nanorod-Structure

ZnO possesses a wurtzite structure that lacks a center of symmetry and thus it exhibits strong piezoelectric and pyroelectric properties (Baruah & Dutta, 2008). The conductivity of ZnO can also be increased through doping. ZnO also finds its uses in the fields of acoustic wave filters, photonic crystals, photodetectors, light emitting diodes,

photodiodes, gas sensors, optical modulator waveguides, solar cells and varistors (Yi, Wang, & Park, 2005). The transparency of ZnO nanrods in the visible wavelength range coupled with its wide bandgap (3.37eV) is suitable for optoelectronic applications. ZnO crystal also possesses high exiton binding energy (60meV) which allows efficient exitonic emission at room temperature. Because of its hardness and rigidity, ZnO plays a very important role in ceramics industry while its less toxicity, biocompatibility and biodegradability make ZnO a best material in biomedicine and pre-ecological systems (Kołodziejczak-Radzimska & Jesionowski, 2014).The crystal of ZnO has a hexagonal wurtzite structure with lattice parameters of a = 0.3296 and c = 0.52065 nm. The piezoelectric and pyroelectric properties are inherent from the tetrahedral arrangement of Zn^{2+} and O^{2-} ions as shown in the Figure 2.11. The piezoelectric and pyroelectric properties are the resultant of the tetrahedral coordination and the absence of inversion symmetry respectively.

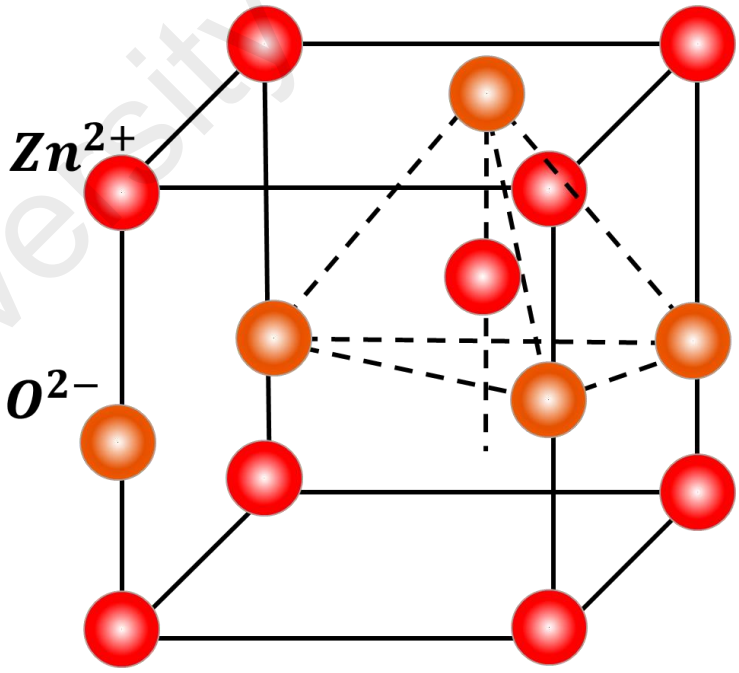

Figure 2.11 Wurtzite structure of ZnO

Crystallography is used to determine the plain of ZnO nanorod structure. ZnO possesses polar and non-polar facets with the basal plane (0001) being the most common polar facet. Oppositely charged ions of Zn^{2+} (0001) and O^{2-} $(000\bar{1})$ occupy the ends of the plane forming a dipole moment resulting in the variance of energy. ZnO ± (0001) are quite peculiar in the sense that they are atomically flat, stable and exhibit no reconstruction. The non-polar facets include the $(2\bar{1}\bar{1}0)$ and $(01\bar{1}0)$ which have lower surface energy than (0001) (Z. L. Wang, 2004). Table 1 show different properties of bulk ZnO.

Table 2.1 Properties of Zinc Oxide

Crystal structure	Hexagonal wurtzite
Lattice constant	a=3.264 A°, c=5.207 A°
Molecular weight	81.38
Density	5.67 g/cm^3
Melting point	1975 °C (3587 F)
Heat of fusion	4,470 cal/ mole
Thermal Conductivity	25 W/mK at 20 °C
Thermal expansion coefficient	4.3x10^{-6}/ K at 20 °C and 7.7 x10^{-6}/ K at 600 °C
Cohesive energy	1.89 eV
Band gap at room temperature	3.37 eV
Refractive index	2.008
Electron and hole effective mass	m_e*=0.28 m_0 , m_h*=0.59 m_0
Debye temperature	370 K
Lattice energy	964 kcal/mole
Dielectric constant	ε_0 = 8.75, ε_∞ = 3.75
Exciton binding energy	60 meV
Piezoelectric coefficient	12 pC/N
Pyroelectric constant	6.8 A/s/cm^2/K x 10^{10}
Solubility	1.6 mg/L (30^{o}C)
Standard enthalpy of formation	-348.0 kJ/mol
Standard molar entropy	43.9 J · K^{-1} mol^{-1}

The growth structures of ZnO nanostructures are quite varied. ZnO can occur in 1D (one dimentional), 2D (two dimentional) and 3D (three dimentional) structures. 1D structures consists of the largest group which includes nanorods, needles, helixes, springs and rings (Banerjee et al., 2003). 2D structures include nanoplates/nanosheets and

nanopellets (Chiu et al., 2010). Examples of ZnO 3D structures include nanorods (Dedova, Volobujeva, Klauson, Mere, & Krunks, 2007), nanowires (Shan, Liu, & Hark, 2008), nanoflowers (Miles, Cameron, & Mattia, 2015), snowflakes (Jing et al., 2012) as shown in Figure 2.12.

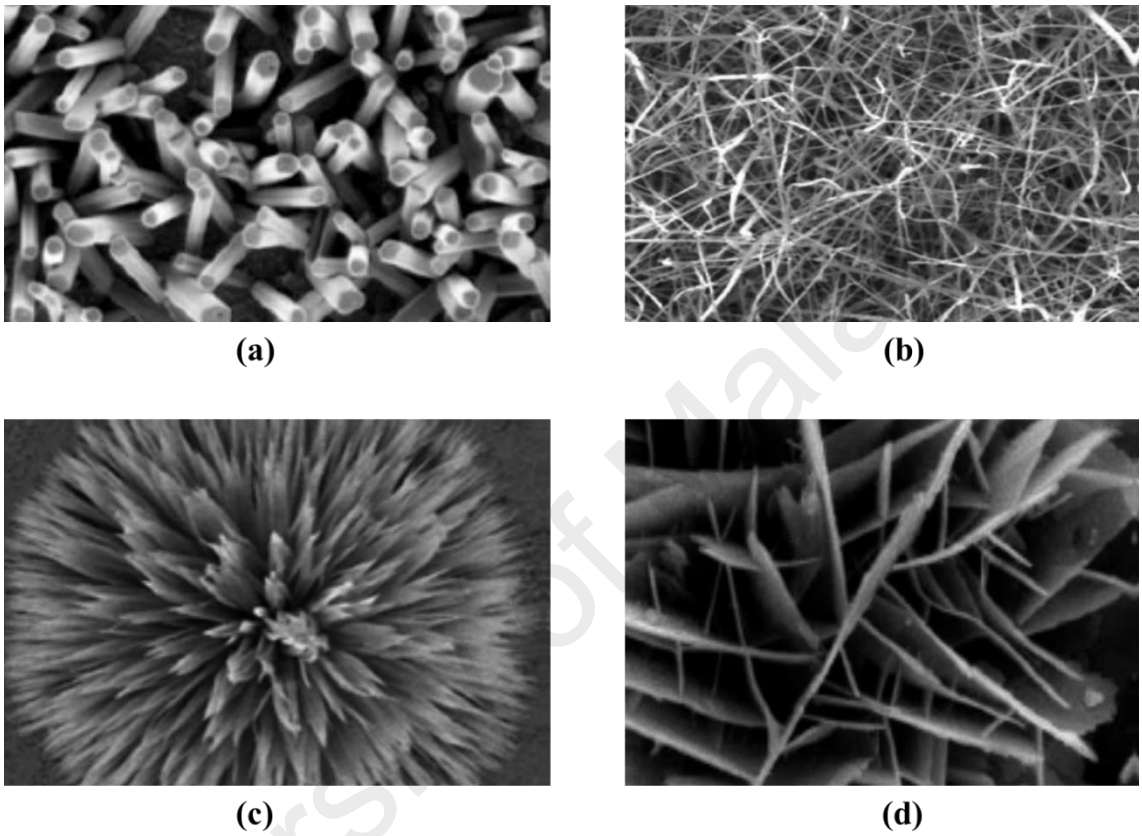

Figure 2.12 3D ZnO structures (a) nanorods (Dedova et al., 2007), (b) nanowires (Shan et al., 2008), (c) nanoflowers (Miles et al., 2015) and (d) snowflakes (Jing et al., 2012).

The growth rate of these variety of novel structures can be tuned along three fast growing directions: $< 2\bar{1}\bar{1}0 >$ ($\pm [\bar{1}2\bar{1}0]$, $\pm[2\bar{1}\bar{1}0]$, $\pm[\bar{1}\bar{1}20]$); $< 01\bar{1}\bar{0} >$ ($\pm[01\bar{1}\bar{0}]$, $\pm[10\bar{1}\bar{0}]$, and $\pm[0001]$. The surface morphologies of these structures depends on the relative surface activities of various growth facets and the kinetic parameters are controlled by the growth conditions. Some of the typical growth morphologies of 1D structures are given in Figure 2.13.

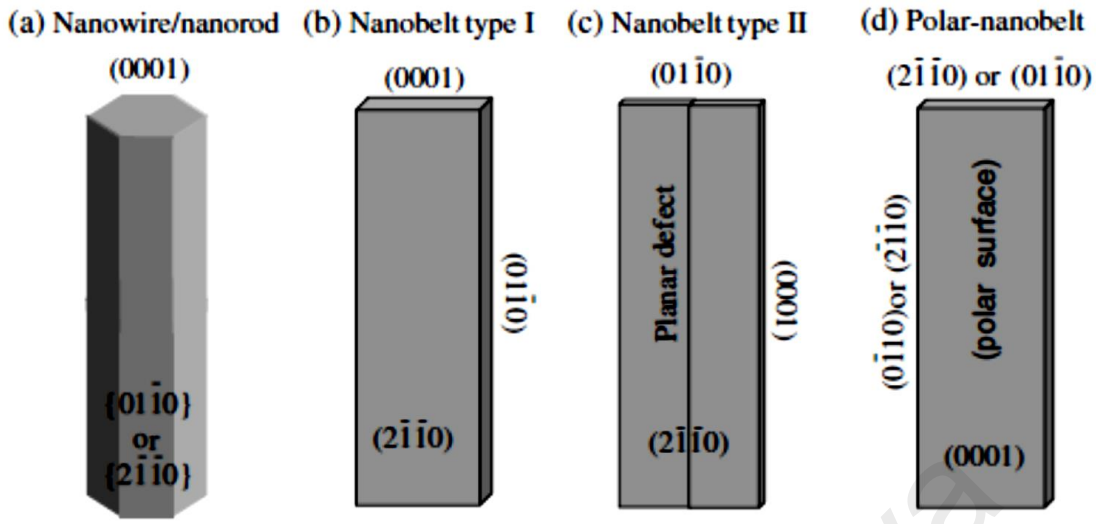

Figure 2.13 Growth morphologies of ZnO 1D nanostructures. (Z. L. Wang, 2004)

2.6 Hydrothermal Synthesis Method of Zinc Oxide Nanostructure

Extensive research for synthesis of ZnO nanoparticles in alcoholic medium using hydrothermal method has been reported and widely accepted (Baruah et al., 2012). The alcoholic medium growth provides faster nucleation and growth as compared to water (Koziol, Boskovic, & Yahya, 2011). The hydrothermal method does not require the use of organic solvents or additional processing of the product (grinding and calcination) which makes it a simple and environmentally friendly technique. This process has many advantages including the possibility of carrying out the synthesis at low temperatures the diverse shapes and dimensions of the resulting crystals depending on the composition of the starting mixture and the process temperature and pressure, the high degree of crystallinity of the product and the high purity of the material obtained (Polsongkram et al., 2008).

The hydrothermal method of ZnO nanorod synthesis is a solution based method. Several literatures exist where the aqueous synthesis of ZnO nanoparticles using Zinc nitrate hexahydrate ($Zn(NO_2)_3$) is reported. (Amin et al., 2011). ($Zn(NO_2)_3$) acts as the source of Zn^{2+} ions and the growth was carried out at temperature of about 100 to 150 ˚C.

pH also plays an important role in the growth of ZnO nanorods. In a previous work, with pH< 11 zinc hydroxide precursors are dissolved partially and ZnO powder is nucleated in a heterogeneous system while for pH>11 the Zinc hydroxide precursors are dissolved and a clear solution is formed with the ZnO powder nucleated in a homogeneous system (Amin et al., 2011). Figure 2.14 shows the effect of pH on the growth of ZnO nanostructures. When pH was increased, the growth rate increased due to the increases of hydroxyl ions (OH^-) concentration which gives arise to ZnO particles in the solution.

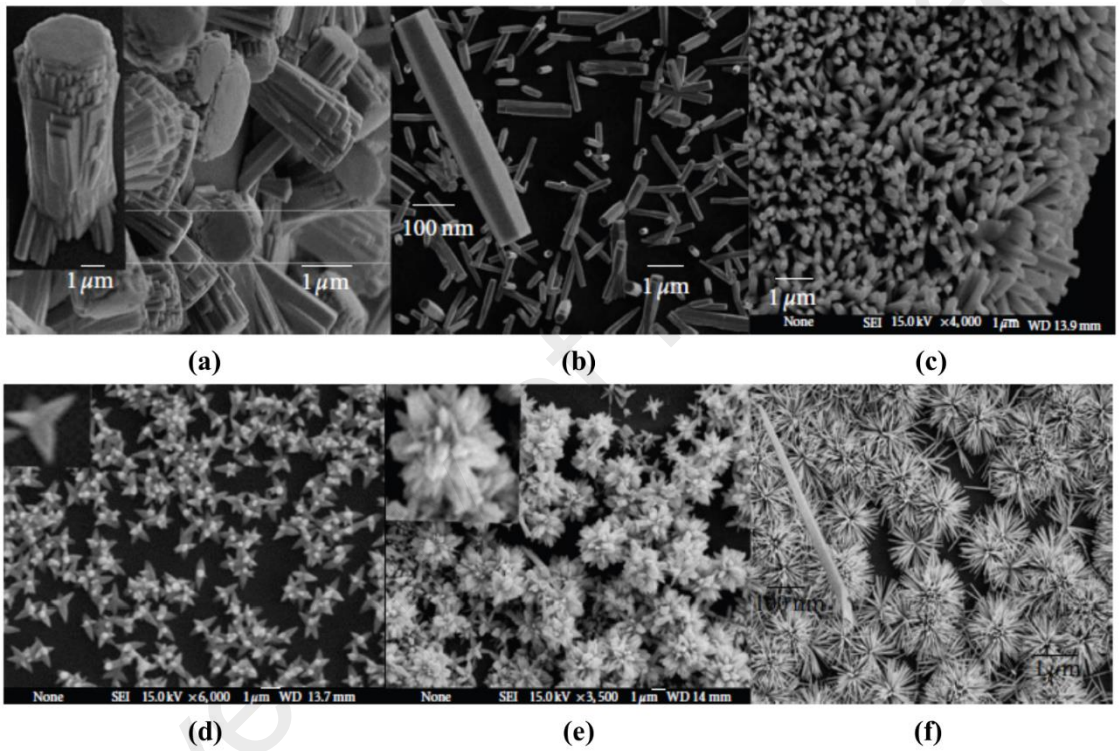

Figure 2.14 SEM images of ZnO nanostructures grown with different aqueous solutions of pH value of (a) 1.8, (b) 4.6, (c) 6.6, (d) 9.1, (e) 10.8 and (f) 11.2. (Amin et al., 2011)

It is well known that increasing or decreasing the concentration of the chemical reactants will eventually influence the resultant products. The density, length and diameter of the ZnO nanorods are varied with the concentration applied during the synthesis. Figure 2.15 shows the effect of different precursor concentrations on ZnO nanorods growth. A linear relation can be seen between the increase of the concentration

and the nanorods dimensions, interestingly the diameter of the nanorods increases gradually.

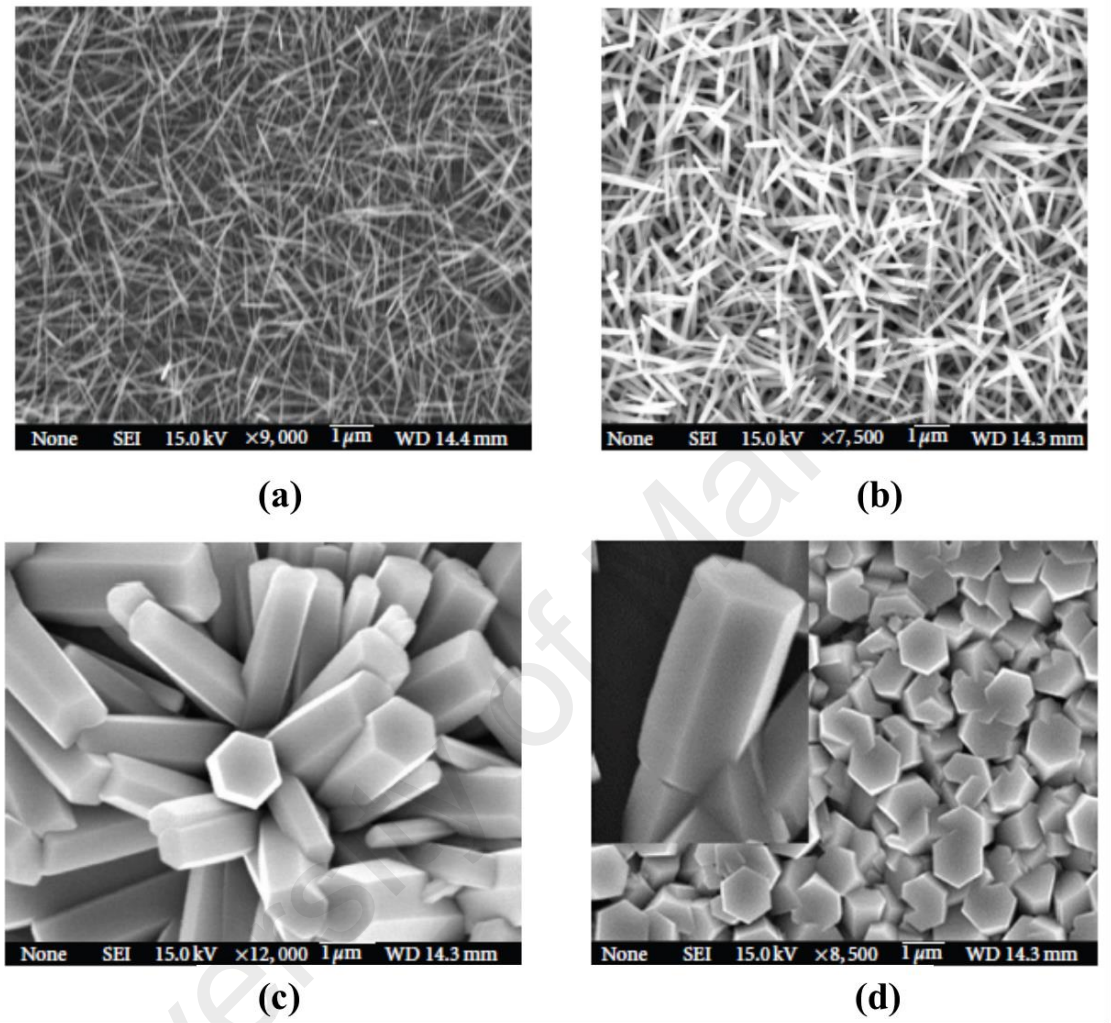

Figure 2.15 SEM images of ZnO nanorods on Si substrate with different precursor concentrations of the growth aqueous solution (a) at 25 mM, (b) 50 mM, (c) 100 mM, (d) 300 mM. (Amin et al., 2011)

An example of hydrothermal reaction is the synthesis of Zinc oxide using the reagents Zinc Choride ($ZnCl_2$) and Sodium Hydroxide (NaOH) in a ratio of 1:2 in an aqueous environment (D. Chen, Jiao, & Cheng, 1999). The chemical reaction is given as below

$$ZnCl_2 + 2NaOH \rightarrow Zn(OH)_2 + Na^{2+} + 2Cl^- \quad (2.1)$$

The white precipitate zinc hydroxide $Zn(OH)_2$ underwent filtration and washing and then the pH was controlled at around 5-6 using hydrochloric acid (HCl). The hydrothermal heating takes place at an autoclave with a set temperature followed by cooling. ZnO is obtained as the end product according to the equation

$$Zn(OH)_2 \rightarrow ZnO + H_2O \quad (2.2)$$

Another example of hydrothermal method was proposed by the following reaction (Ismail, El-Midany, Abdel-Aal, & El-Shall, 2005).

$$Zn(CH_3COO)_2 + 2NaOH \rightarrow Zn(OH)_2 + 2CH_3COONa \quad (2.3)$$

$$Zn(OH)_2 \xrightarrow{\text{Temperature}} ZnO + H_2O \quad (2.4)$$

The chemical reaction between $Zn(CH_3COO)_2$ and NaOH was carried out in the presence of hexamethylenetetramine (HMT) at room temperature. The resulting precipitate of $Zn(OH)_2$ was washed with water several times and then underwent thermal treatment in a Teflon-lined autoclave. Based on SEM images, the authors concluded that the HMT, as a surfactant, plays an important role in the modification of the ZnO particles. The shape of the particles is also affected by the time and temperature of the hydrothermal process. With an increase in time, temperature and surfactant concentration, the size of the particles increases. Hydrothermal processing of the precursor, followed by drying, produced spherical particles of ZnO with sizes in the range 55–110 nm depending on the conditions of synthesis.

In previous work, a thin layer of ZnO nanoparticles were grown on glass substrate by thermal decomposition of Zinc nitrate and HMT using the hydrothermal method (Ashfold, Doherty, Ndifor-Angwafor, Riley, & Sun, 2007; Vergés, Mifsud, & Serna, 1990). HMT is a non-ionic highly water soluble tertradentate cyclic tertiary amine. It

releases OH^- on thermal decomposition which reacts with Zn^{2+} ions to form ZnO. The chemical equation involved in the process is summarized as

$$(CH_2)6N_4 + 6H_2O \rightarrow 6HCHO + NH_3 \quad (2.5)$$

$$NH_3 + H_2O \rightarrow NH^{4+} + OH^- \quad (2.6)$$

$$2OH- + 2Zn^{2+} \rightarrow ZnO(S) + H_2O \quad (2.7)$$

The role of the HMT is manifold. It not only supplies hydroxyl ions to drive the precipitation reaction but also acts as a buffer as the rate of its hydrolysis decreases with increasing pH and vice versa. The role of HMT in the growth process of ZnO nanowire was also discussed in a very different manner in other literature (Sugunan, Warad, Boman, & Dutta, 2006). It was proposed that HMT will attach to the non-polar facets of zincite crystal preferably being a long chain polymer and a nonpolar chelating agent. It therefore cuts off the excess Zn^{2+} ions to them leaving only the polar (0001) face for epitaxial growth. HMT therefore acts like a shape inducing polymer surfactant rather than as a buffer. The morphology of ZnO nanostructures can be controlled by varying the amount of a soft surfactant, ethylenendiamine and the pH of the reaction mixture of zinc acetate, sodium hydroxide and the surfactant. Homogeneous growth was obtained at a pH of 12 and inhomogeneity occurs as the pH decreases. However, HMT to zinc nitrate relative concentrations and growth temperature were reported having a profound effect over density, orientation and growth of the ZnO nanorods (Mahmood, Bora, & Dutta, 2013). In the work, the effect of molar ratio of zinc nitrate and hexamine, ZnO nanorods were grown in precursors with 10 mM concentration of zinc nitrate hexahydrate and varying the HMT concentration (0 mM, 2 mM, 5 mM, 10 mM, 12 mM and 15 mM). As a result, the 1:1 molar ratio of zinc nitrate and HMT in the precursor solution exhibited the maximum photocatalytic efficiency. For synthesis temperature effect on the growth rate of ZnO nanorods, 10 mM precursor solution was prepared to grow ZnO nanorods for 15 hours at temperature 40 ˚C, 50 ˚C, 70 ˚C and 90 ˚C. It was found that ZnO nanorod

growth at 90 ˚C exhibited the highest photocatalytic efficiency. Figure 2.16 shows the scanning electron microscope (SEM) image of the hydrothermally grown ZnO nanorods using $Zn(NO_3)_2$ and HMT.

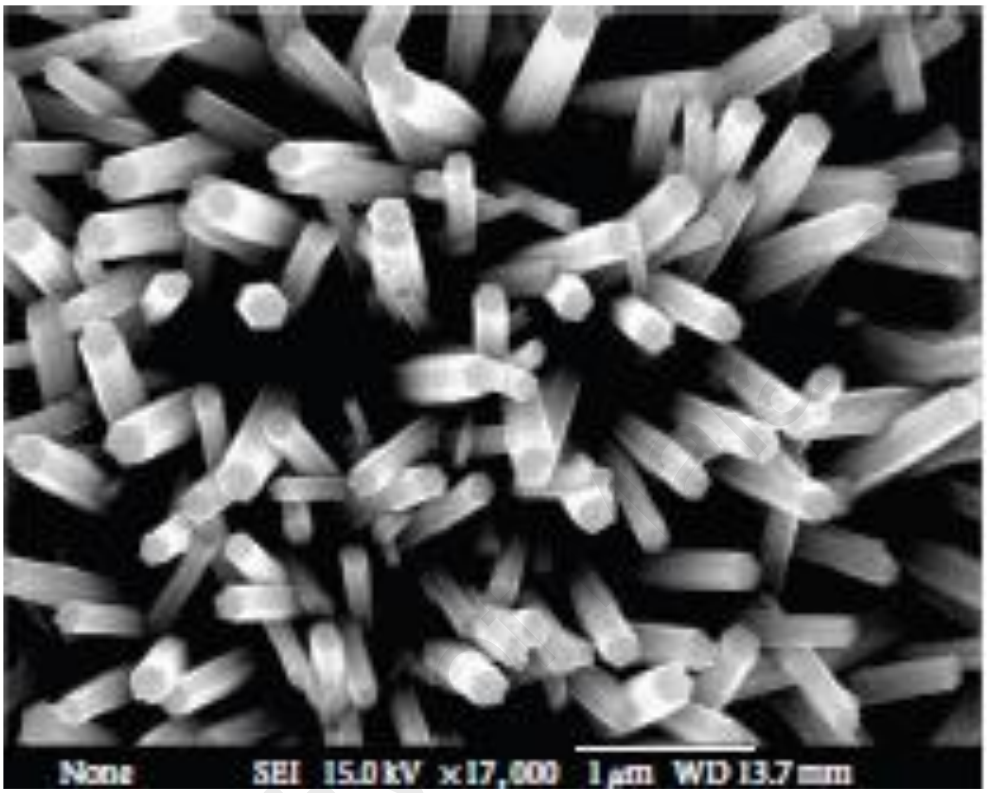

Figure 2.16 SEM image of ZnO nanorods grown using $Zn(NO_3)_2$ and HMT (Baruah & Dutta, 2008)

2.7 Zinc Oxide in Global Applications

Zinc oxide (ZnO) is widely used in many areas because of its diverse properties both physical and chemical. ZnO finds its uses in a variety of fields which include industries, pharmaceuticals, chemicals and paint industry. Figure 2.17 summarizes the various applications of zinc oxide and their uses. ZnO is widely used in rubber industry to improve the thermal conductivity of pure silicon rubber while retaining its high electrical resistance and are promising candidates as high performance engineering materials. The disinfecting and antibacterial properties of ZnO make it a suitable material for producing various kinds of medicines. ZnO can be applied locally in the form of cream

or ointments or can be administered orally. It also exhibits peeling effect at higher concentrations.

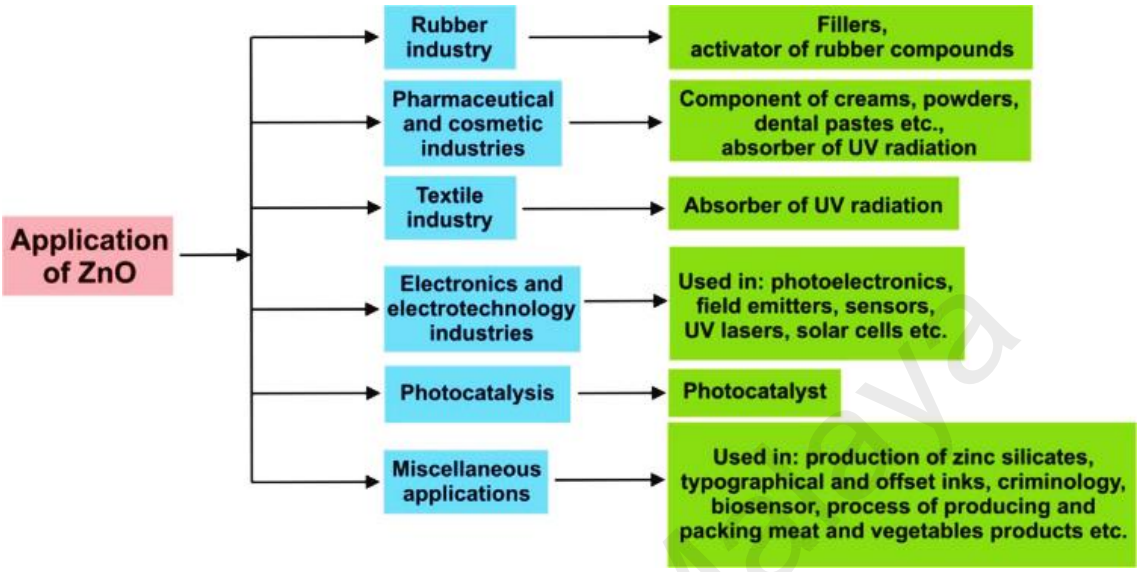

Figure 2.17 Various applications of ZnO (Kołodziejczak-Radzimska & Jesionowski, 2014)

ZnO is also used in various types of nutritional products and diet supplements, where it serves to provide essential dietary zinc. Due to their ability to absorb UVA and UVB radiation ZnO products are used in sun screen creams. Its wide energy band (3.37 eV) and high bond energy (60 meV) (Y. Kong, Yu, Zhang, Fang, & Feng, 2001; Venkatesh & Jeganathan, 2013) at room temperature mean that zinc oxide can be used in photoelectronic (Purica, Budianu, & Rusu, 2001) and electronic equipment (Aoki, Hatanaka, & Look, 2000), in devices emitting a surface acoustic wave (Gorla et al., 1999), in field emitters (Jo et al., 2003), in sensors (F.-C. Lin, Takao, Shimizu, & Egashira, 1995), in UV lasers (Tang et al., 1998) and in solar cells (Krebs, Thomann, Thomann, & Andreasen, 2008; Repins et al., 2008). ZnO also exhibits the phenomenon of luminescence (chiefly photoluminescence—emission of light under exposure to electromagnetic radiation). Because of this property it is used in FED (field emission display) equipment, such as televisions (Ihara et al., 2002). It is superior to the

conventional materials, sulfur and phosphorus (compounds exhibiting phosphorescence), because it is more resistant to UV rays and also has higher electrical conductivity.

Zinc oxide is also used in gas sensors (L. Wang et al., 2012; J. Xu, Pan, & Tian, 2000). It is a stable material whose weak selectivity with respect to particular gases can be improved by adding other elements. The working temperature of ZnO is relatively high (400–500 °C), but when nanometric particles are used this can be reduced to around 300 °C. The sensitivity of such devices depends on the porosity and grain size of the material; sensitivity increases as the size of zinc oxide particles decreases. It is most commonly used to detect CO and CO_2 (in mines and in alarm equipment), but can also be used for the detection of other gases (H_2, SF_6, C_4H_{10}, C_2H_5OH). Apart from the applications mentioned above, zinc oxide can also be used in other branches of industry, including for example concrete production. The addition of zinc oxide improves the process time and the resistance of concrete to the action of water. Also, the addition of ZnO to Portland cement slows down hardening and quenching (it reduces the gradual evolution of heat), and also improves the whiteness and final strength of the cement (Olmo, Chacon, & Irabien, 2001). It is also added to many food products, including breakfast cereals. ZnO is used as a source of zinc, which is an essential nutrient (Whittaker, 1998). Thanks to their special chemical and antifungal properties, zinc oxide and its derivatives are also used in the process of producing and packing meat products (e.g., meat and fish) and vegetable products (e.g., sweetcorn and peas) (Espitia et al., 2012).

2.8 Light Scattering and Side Coupling

Light scattering first captured the imagination of the ancients with observations of variations of colour in nature, including the blue sky, the rainbow and the dramatic colours seen at dusk and dawn (Lynch & Livingston, 2001; Minnaert, 2013). The first recorded light scattering observations date back to the 11th century when Alhasen of Basra attempted to explain the color of the blue sky (Singh & Riess, 2001). Many great scientific minds that followed pursued light scattering experiments, including Leonardo da Vinci (Hey, 1983) and Sir Isaac Newton (Lilienfeld, 2004). Lord Rayleigh was the first to provide a quantitative treatment of light scattering in the 19th century and the concept of Rayleigh scattering survives to this day (Rayleigh, 1917). While light scattering analysis is used in many fields of study, it is only recently that light scattering has become useful for biomedical applications (Mourant, Hielscher, Eick, Johnson, & Freyer, 1998; Murdock, Braydich-Stolle, Schrand, Schlager, & Hussain, 2008), optoelectronics (Müller et al., 2002) etc. Based on these great discoveries of light scattering, the concept was applied in optical field using ZnO nanostructures (H Fallah et al., 2013). Basically, this research work integrates photonics and nanotechnology to apply the behaviour of light scattering towards light side coupling that occurs due to the incident angle of the incoming light is greater than the critical angle between the surrounding and cladding or core coated with ZnO nanorods grown on the multimode optical fiber. Through this concept, light side coupling is practically impossible to be applied with the light incident angle larger than critical angle between core or cladding and air media. The only way to trap light inside fiber by applying another material on the optical fiber as scattering element. In the case, ZnO nanorods can excite the core or cladding mode which is very sensitive to surrounding environment and scatter light into the fiber core. The whole idea of side coupling is governed by the law of refraction. ZnO nanorods grown on has a higher refractive index ($n_{ZnO} \sim 2$) than the core material ($n_{Silica} \sim 1.5$) and allows

light coupling into nanorod waveguides. As light is launched at the side of the fiber the ZnO nanorods being a photonic crystal acts as a waveguide and scatters light in various angles. The part of the light whose incident angle, θ_i is greater than the critical angle is coupled inside the fiber as the condition for total internal reflection is achieved inside the core modes as indicated in Figure 2.18. This allows light propagation inside the optical fiber and light leakage from these modes, permitting two possible light coupling collection schemes which are light exits from the side and is collected either from the optical fiber end or through a side optical fiber probe. The nanorod arrays on the multimode optical fiber also provide a suitable environment for sensing applications due to their large surface to volume ratio. The optical scattering properties of the nanorods depends on its shape, density and uniformity and these parameters are tuned by choosing proper growth conditions.

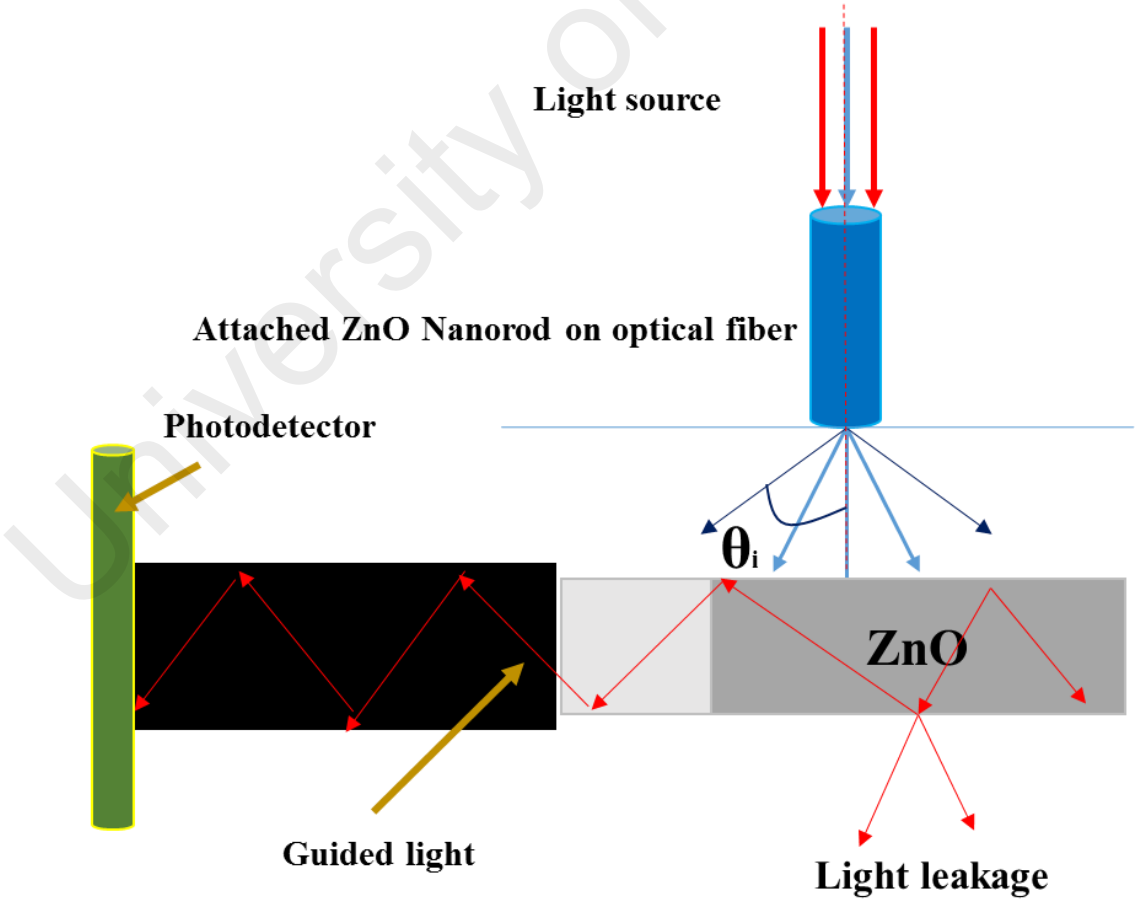

Figure 2.18 Illustration of light scattering from one ZnO nanorod

Figure 2.18 depicts the excitation of cladding modes leak while propagating due to the presence of nanorods. The total power inside the optical fiber decays exponentially due to scattering effects. In the case, the absorption of visible light was neglected which is minimal because ZnO is a wide band gap semiconductor. The total power is written as below:

$$P_{guided}(z) = P_o \exp\{-2\,\alpha_s\, X\,(z - z_o)\} + P_\infty \qquad (2.1)$$

Where

P_o and P_∞ = the coupled light power at ($z = z_o$) and background ($z \rightarrow \infty$)

α_s = nanorods scattering coefficient.

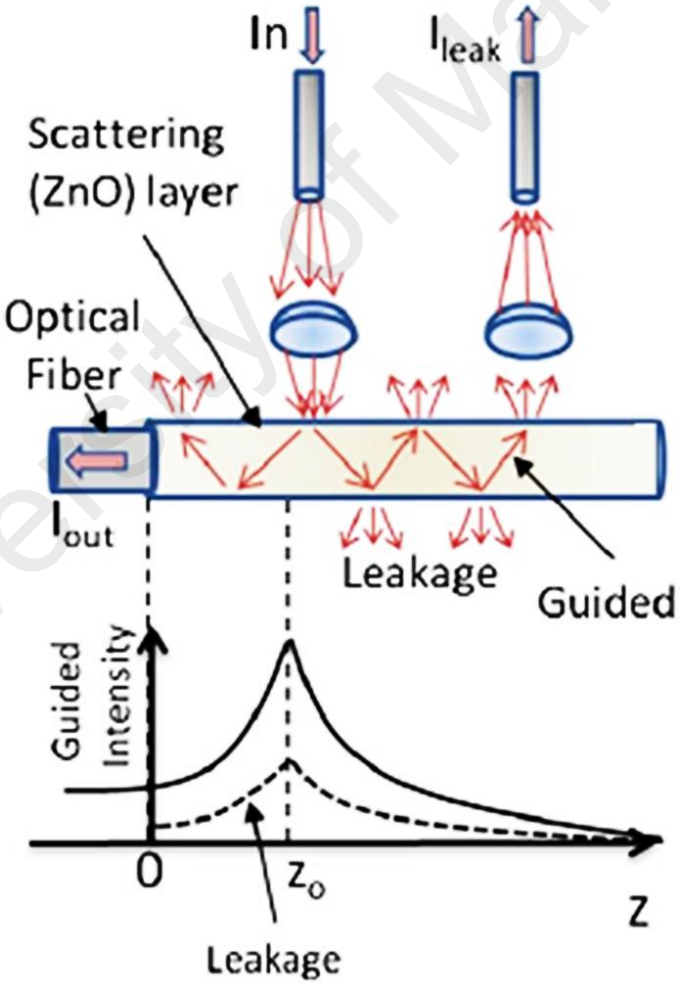

Figure 2.19 Schematic representation of two possible configurations of side coupling to cladding modes with guided and leakage intensity responses of light paths in the side coupling configuration (H Fallah et al., 2013)

However, the excitation inside the fiber is only maximized at $Z = Z_O$ and then the intensity of the guided light reduces exponentially to the ZnO nanorods interface ($Z = 0$). For the location farthest away from the interface, any light reaching the detector is minimised. In the approach, a fundamental work was practically performed to characterize the scattering coefficient, α_s and coupling intensity for different concentrations of zinc acetate used during seeding process in hydrothermal process (3 mM, 4 mM, 5 mM & 6 mM). The optical characterization was performed by measuring the output power to cladding mode in wet etched optical fiber coated with ZnO nanorods using longitudinal scanning approach as graphically illustrated in Figure 2.20. The output power was recorded by a photodetector placed at the end of the optical fiber while the coupling intensity was captured using a charge-coupled device (CCD camera) at incident angle along the optical fiber. The output from camera and photodetector were synchronized using a computer to record images of coupling intensity and output power while moving the stage parallel to the optical fiber. Then, the scattering coefficient can be directly determined from the measurement using Equation (2.1).

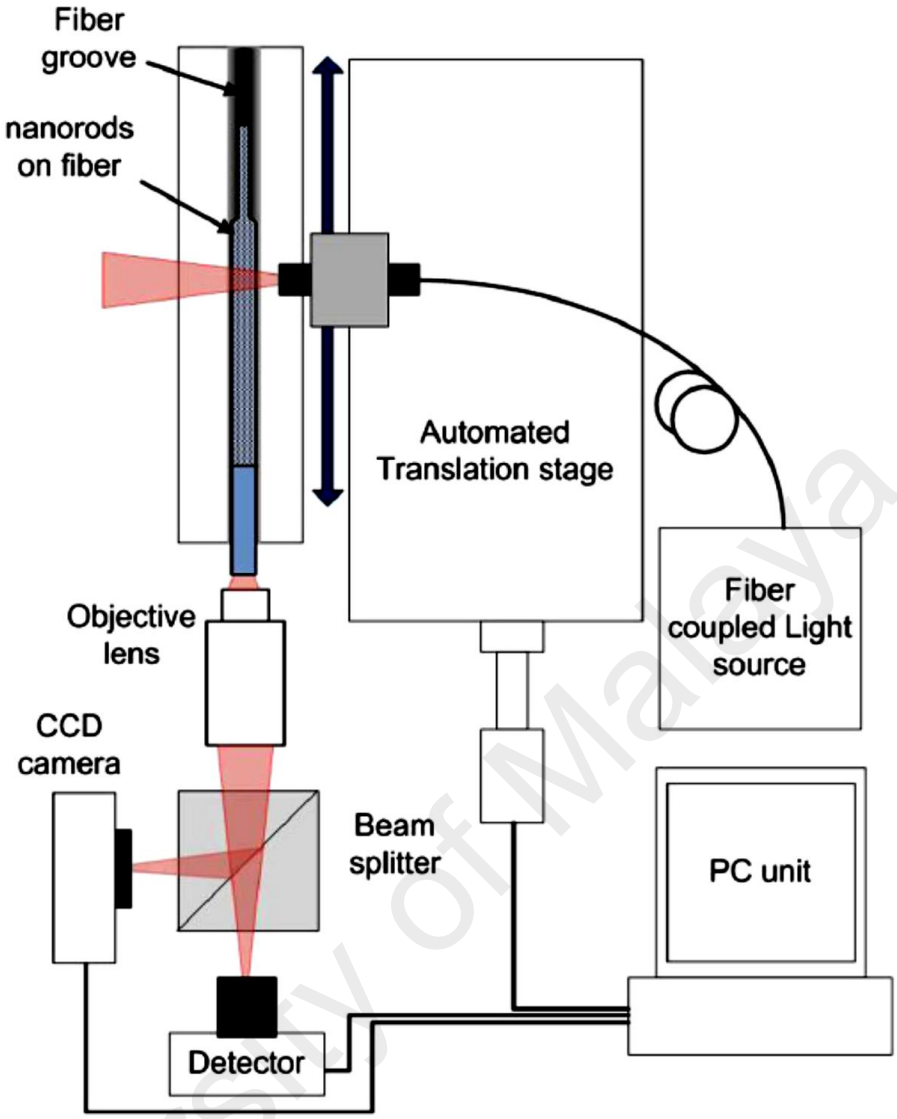

Figure 2.20 Optical characterization setup for the light side coupling (Hoorieh Fallah et al., 2014)

As results, the coupling intensity versus displacement of light source was plotted as shown in Figure 2.21. It was observed that the use of 4 mM of zinc acetate for seeding showed the brightest intensity. The coupling intensity rapidly reduces due to the increase in distance of the excitation location of light source from photodetector.

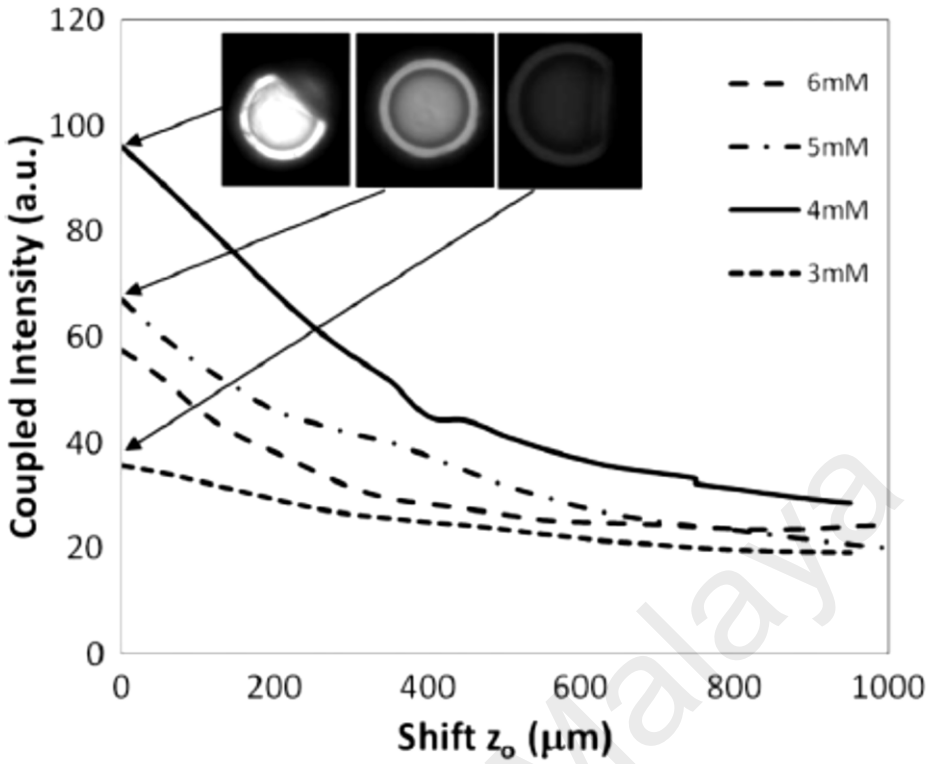

Figure 2.21 The coupling intensity of different concentration of zinc acetate for ZnO nanorods grown on wet etched optical fiber (H Fallah et al., 2013)

Figure 2.22 shows the measured coupling output and scattering coefficient versus the concentration of zinc acetate for ZnO nanorods growth on the wet etched optical fiber to excite cladding mode. Relatively, 4 mM of zinc acetate was found to be the highest scattering coefficient. Higher zinc acetate concentration could lead to the lack of pattern in directionality of ZnO nanorods that might affect the scattering coefficient values as indicated through the large standard deviation.

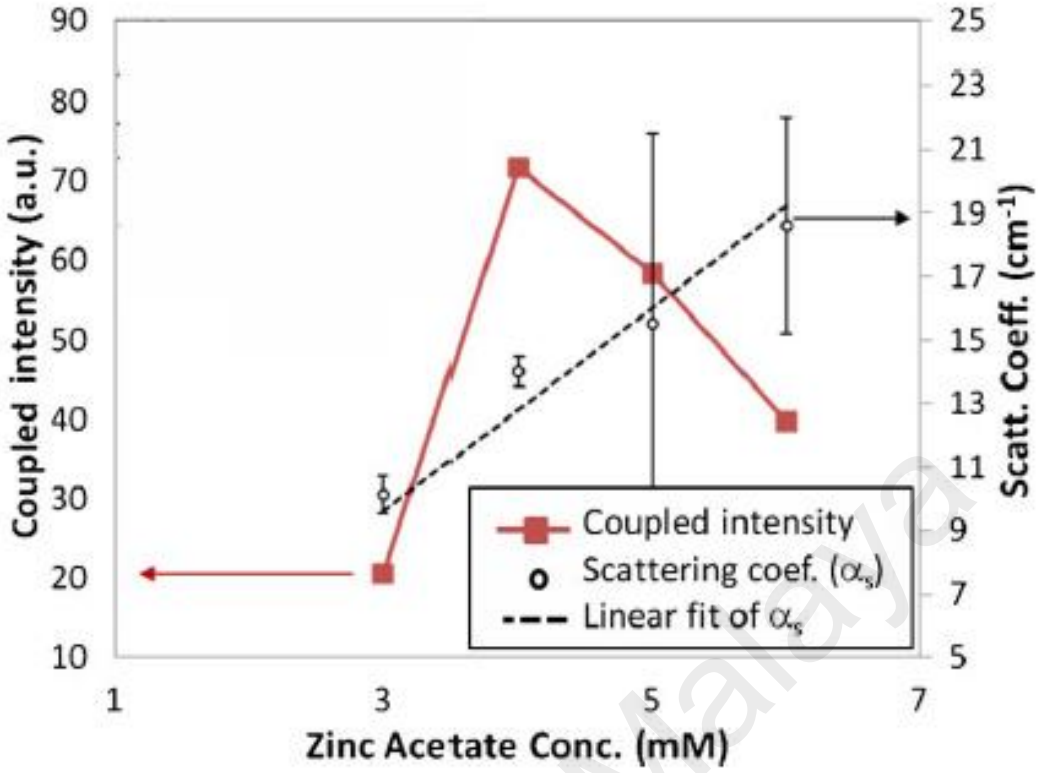

Figure 2.22 The measurement of coupling intensity (y- left axis), the average scattering coefficient (y- right axis) and versus the concentration of zinc acetate (H Fallah et al., 2013)

The investigation on coupling intensity was extended to excite core mode in wet etched of optical fiber using the experiment setup as shown in Figure 2.20. A multimode optical fiber was wet etched for 20 minutes and subsequently coated with ZnO nanorods. Figure 2.23 shows the comparison of coupling intensity between cladding mode and core mode. It was found that the power coupled to the core modes is higher than the cladding modes. In addition, power exponentially decays due to leakage of the core mode through the presence of ZnO nanorods on the wet etched region when the light source was moved away from the focused region.

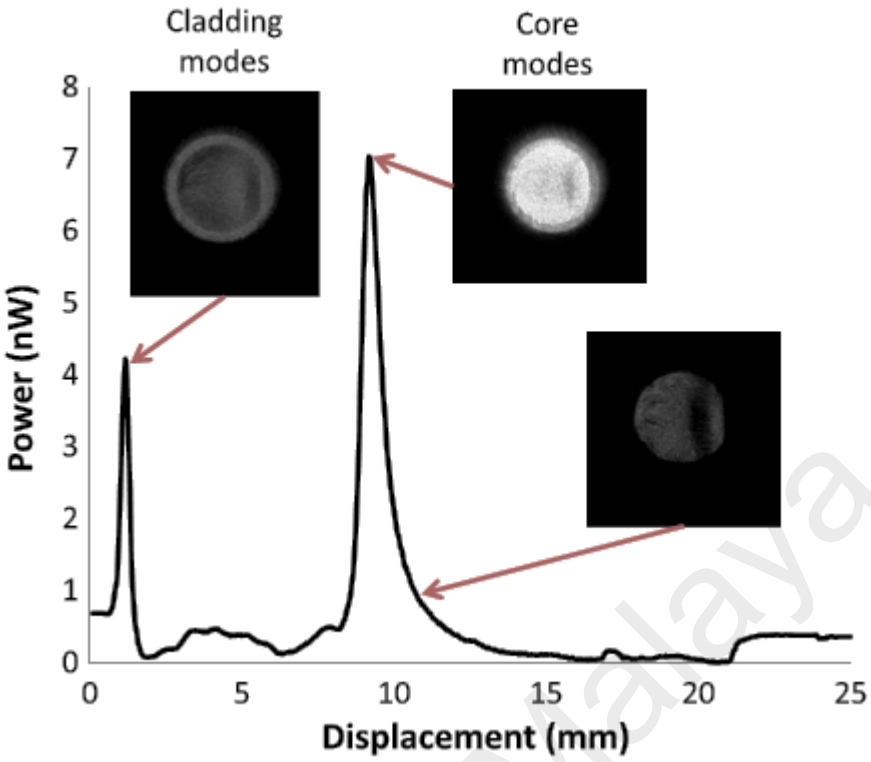

Figure 2.23 The coupling intensity for cladding mode and core mode at different excitation location on the optical fiber (Hoorieh Fallah et al., 2014)

However, the primary limitation of wet etching method was that only a small region of the fiber could be used for signal collection. This situation is not preferable for sensing applications where extended light sources are required. Another fundamental work of light side coupling was also performed to characterize the scattering properties of ZnO nanorods such as cross section and maximum power coupling using nephelometry method. Figure 2.24 shows the homemade nephelometer using a collimated fiber coupled with white light LED source and a photodetector.

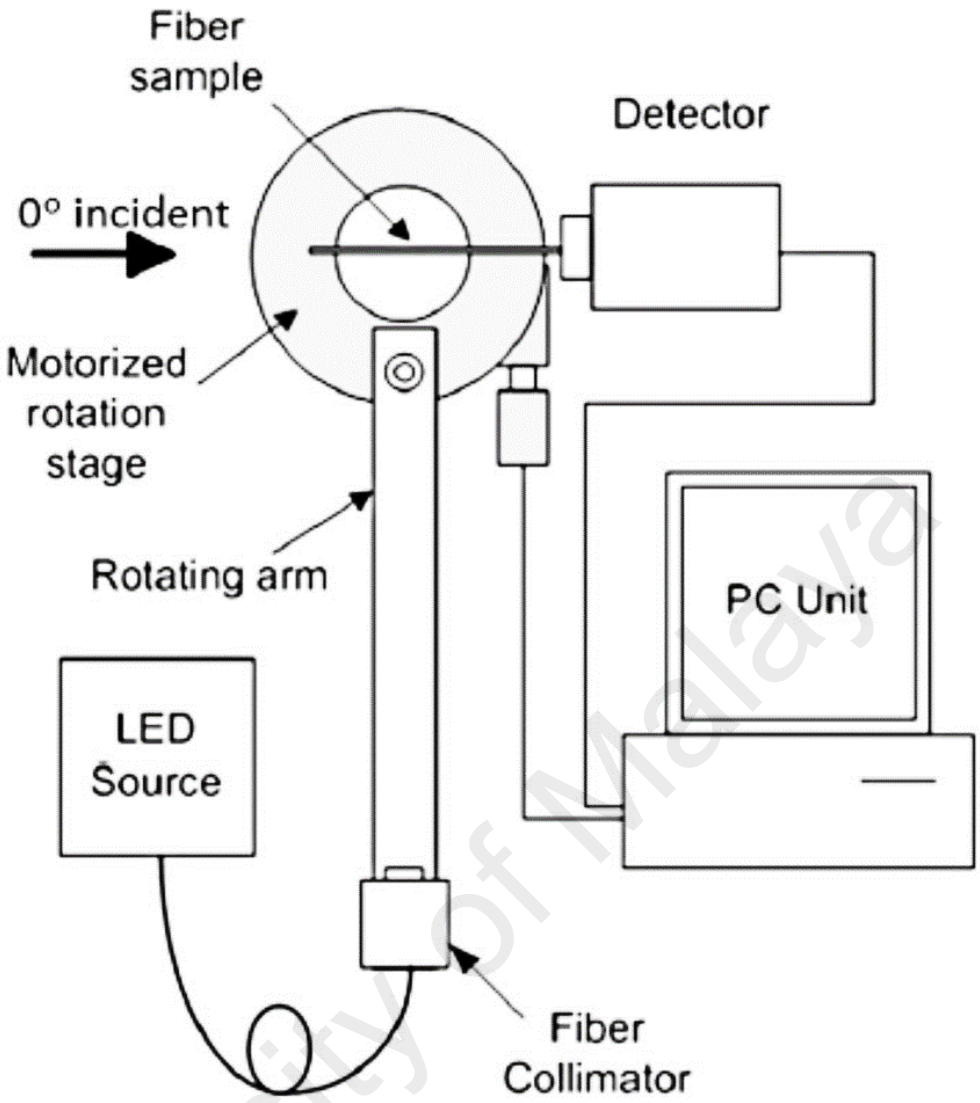

Figure 2.24 Optical nephelometer setup for testing scattering properties of ZnO grown on glass substrate (Hoorieh Fallah et al., 2014)

In the optical characterization, ZnO nanorods were grown on a flat glass substrate using hydrothermal method in order to optimize the growth condition. This is to avoid the effects on angular spectrum of the scattering process since a cylindrical lens was used in the work. Moreover, the growth of ZnO nanorods around the optical fiber might increase the interaction among the ZnO nanorods. The characterization was performed for different concentrations of zinc acetate using in seeding process which are 1 mM, 2 mM, 4 mM and 6 mM. As a result, a polar plot as shown in Figure 2.25 presents the measured normalized angular power spectra and density, ρ_a for different zinc acetate

concentrations. It was observed that the lowest concentration of zinc acetate demonstrates highest coupling power at incident angle larger than critical angle, θ_c. Meanwhile, higher concentrations presented lower coupling power compared to 1 mM. The ZnO nanorods density was given by the number of rods in a selected area divided by the area, A (cm^2). It was seen that the number of ZnO nanorods per unit area is almost constant and increasing the concentration did not have significant effects on length and diameter on ZnO nanorods. Base on the analysis, the seeding solution molarity was fixed to 1 mM for growing ZnO nanorods on optical fiber.

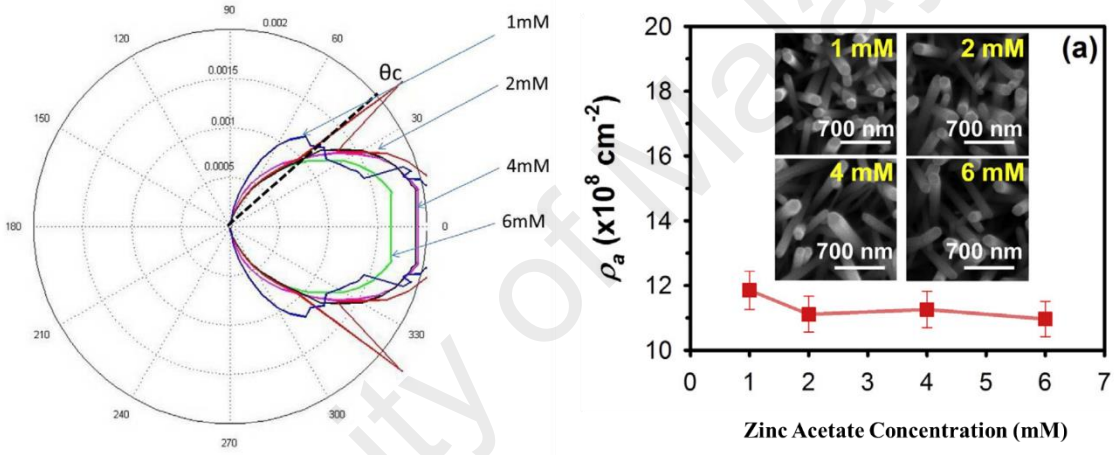

Figure 2.25 The measurement of (a) normalized angular power spectra and (b) density, ρ_a respect to the concentrations of zinc acetate used for preparing the ZnO seed layer on glass substrate (Bora et al., 2014)

2.9 Recent Research on Temperature and Gas Sensing Using Optical Fiber

Interest in monitoring temperature has constantly been on the increase in recent years. The monitoring is very important because it is necessary in many different fields such as medical (Takaki, 1998), food industry (Law, Bermak, & Luong, 2010), sport (Byrne & Lim, 2007), living residences (Wood et al., 2008) etc. For instance, a sensor system is required in operating room to prevent the buildup of humidity that can pose serious risks to patient health. Up to date in 2016, researches still use the very common

optical fiber in temperature sensing which is fiber Bragg gratings (FBG) using silica optical fiber (Warren-Smith, Nguyen, Lang, Ebendorff-Heidepriem, & Monro, 2016; Woyessa, Nielsen, Stefani, Markos, & Bang, 2016). The fabrication process of FBG involves a complicated process and expensive equipment such as high performance laser light source with high pulse energy for open structures. In addition, the Bragg grating region is difficult to determine using laser light source with 1550 nm in wavelength. An integration of visible light source and the spliced single-mode fiber is required so that scattering from the ablation spots could be observed.

In other method, Mach-Zehnder interferometer (MZI) has been commonly used in diverse sensing applications because of their flexible configurations (B. H. Lee et al., 2012). MZI is a device used to determine relative phase shift between two collimated beams from a coherent light source either by changing length of one of the arms or by placing a sample in path of one of the beams. In a recent research, temperature sensor based on POF and electro-optic effect of MZI using a laser source of wavelength 635 nm was proposed (S. Kumar & Swaminathan, 2016). Figure 2.26 shows the proposed setup of liquid temperature sensor.

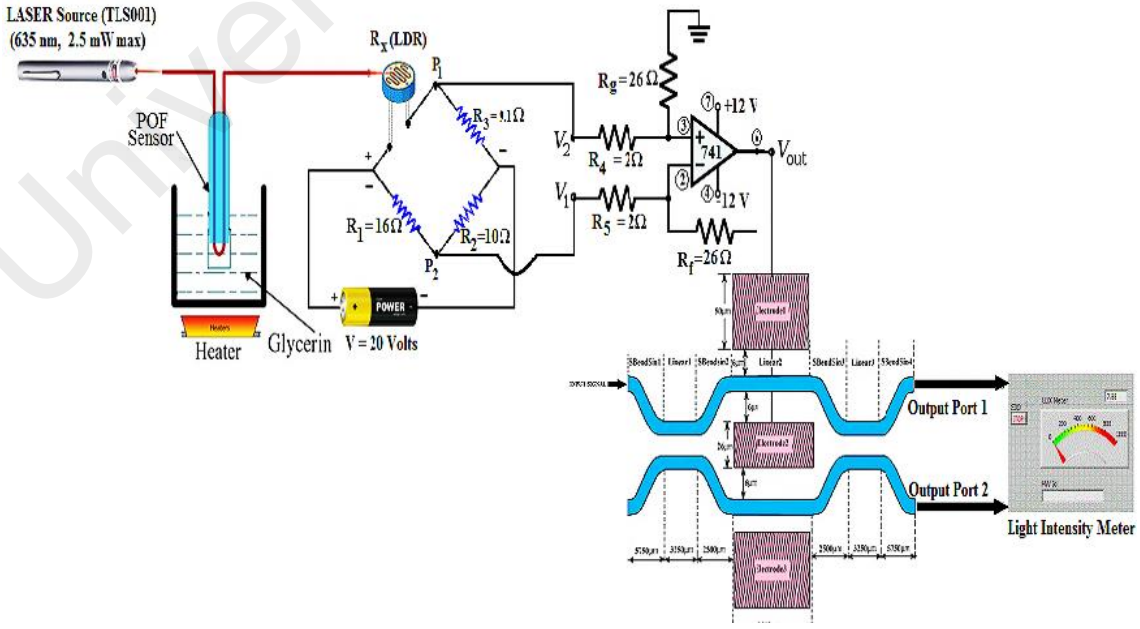

Figure 2.26 The setup of liquid temperature sensor. (S. Kumar & Swaminathan, 2016)

The laser light source is used to generate a beam of light and then this beam is guided into the POF. The setup employed a differential amplifier in order to detect precisely a small variation in liquid temperature.

Gas sensing plays important roles in many applications including safety management of oil and gas industry (Vogler & Sigrist, 2006) and exhaust gas monitoring for combustion engines (Docquier & Candel, 2002). There are numerous gas sensing technologies available to sense various gases. Among them, optical fiber sensors using infrared (IR) absorption spectroscopy (Hoo, Jin, Ho, Wang, & Windeler, 2002); (Chong et al., 2015) stands out due to the high detection specificity. IR spectroscopy is based on the optical absorption of molecular vibration bands, which represent the particular of various gas molecules. Therefore, IR absorption spectroscopy is widely used due to reliable technique for both detection and identification of hazardous and greenhouse gases. In addition, IR sensors have minimal drift, fast response, long lifetime and can be conducted in real time and in situ without disturbing the target system (Hodgkinson & Tatam, 2012). An optical fiber sensor for gas detection has been developed based on IR absorption spectroscopy (Chong et al., 2016). The proposed sensor demonstrated ultra-sensitive to detect the level of carbon dioxide (CO_2) at 1570 nm wavelength.

Surface plasmon resonance (SPR) for gas detection and biosensing was demonstrated by Nylander and Liedberg (Liedberg, Nylander, & Lunström, 1983; Nylander, Liedberg, & Lind, 1982). Since then SPR sensing has been receiving continuously growing attention from scientific community. SPR is a powerful technique for direct sensitive chemical detection (Abdelghani et al., 1997). A latest research using SPR technique was developed for in situ detection of xanthan gum (Michel, Xiao, Skillman, & Alameh, 2016) using 1550 nm laser light source. Figure 2.27 shows the experiment setup using optical equipment such as optical power meter, optical circular, mirror, prism and laser beam which is not cost effective and complicated in measurement.

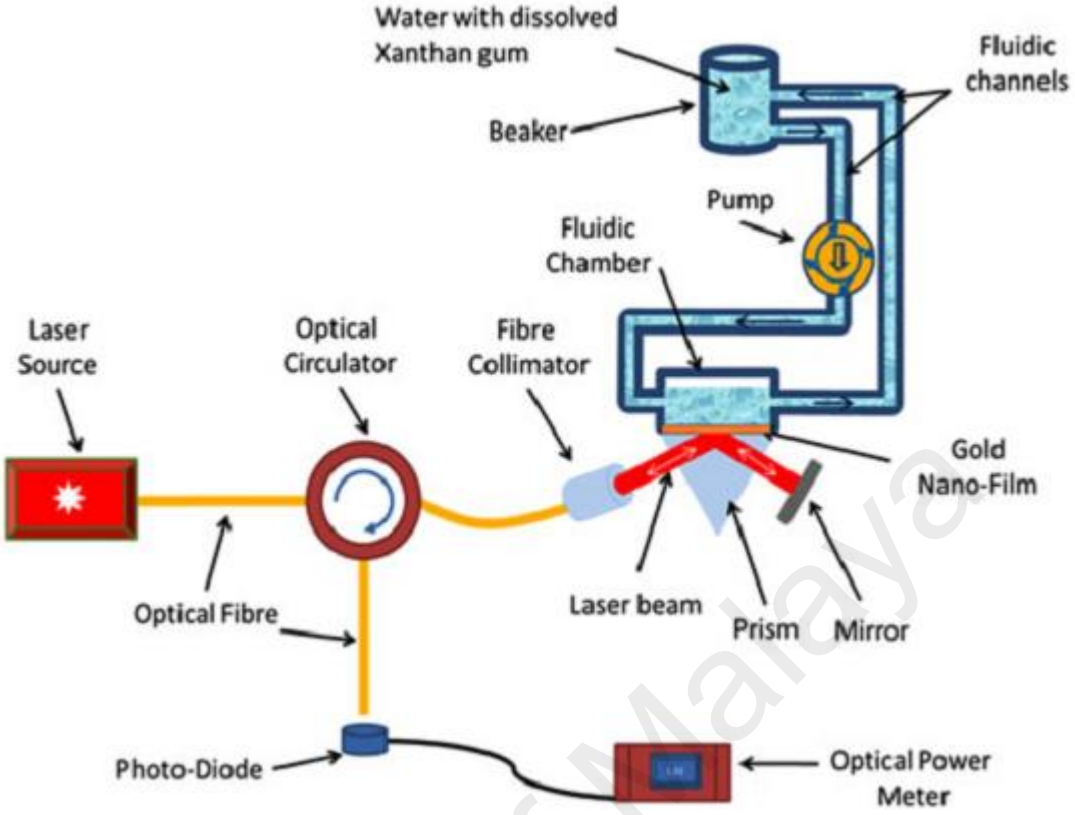

Figure 2.27 Optical fiber sensor based on SPR for chemical sensing. (Michel et al., 2016)

In all the systems explained above, laser light source was widely used in temperature and gas sensing and light was launched from one end of the fiber while signal was collected at the other end. In order to reduce cost and complexity in design and increase the utilization of visible light in sensing applications with high sensitivity, this work applies the behavior of light scattering from ZnO nanorods into POF towards light side coupling.

CHAPTER 3: OPTIMIZATION OF ZINC OXIDE NANOROD COATINGS ON LARGE CORE PLASTIC OPTICAL FIBER THROUGH HYDROTHERMAL GROWTH

3.1 Introduction

Zinc oxide coating is a layer containing zinc (Zn) and oxygen (O) which can be synthetically produced using various chemical methods such as mechanochemical process (Ao, Li, Yang, Zeng, & Ma, 2006; Stanković, Veselinović, Škapin, Marković, & Uskoković, 2011), sol-gel (Benhebal et al., 2013; Mahato et al., 2009), hydrothermal (D. Chen et al., 1999; Ismail et al., 2005) and emulsion (Stanković et al., 2011). As explained in the previous chapter, zinc oxide (ZnO) has attracted tremendous interest due to its noticeable performances in electronics, optics and photonics. ZnO is preferable to use in numerous applications because it is insoluble in water, high chemical stability, high electrochemical coupling coefficient, broad range of radiation absorption and high photo-stability. Due to this, ZnO can serve greatly as a coating layer in optical sensor technology to improve and enhance the sensitivity in sensing various physical parameters such as gas concentrations, humidity level, temperature, pressure, strain, etc. Absorption of molecules on the ZnO coating layer can be sensed through variation of ZnO properties such as photoluminescence, electrical conductivity, vibration frequency, mass etc. This chapter explains the synthesis process of ZnO nanorods growth to coat large core plastic optical fiber (POF) using hydrothermal method.

3.2 Optimization parameters for the hydrothermal method

Figure 3.1 shows the important parameters for growing ZnO nanorods using hydrothermal method. In previous works, the hydrothermal synthesis was used to grow ZnO nanorods on glass substrate and silica multimode optical fiber. From these works, chemicals, solution concentration (molarity) and temperature had been optimized successfully to maximize light side coupling by exploiting scattering properties of the ZnO nanorods (Baruah & Dutta, 2008; Bora et al., 2014; H Fallah et al., 2013; Mahmood et al., 2013). Light induced by scattering at angles larger than the critical angle is guided inside the fiber. Although ZnO nanorods enhance optical guidance in this way, they are also responsible for light leakage due to the very same scattering property. In the previous work also, coupling of light to the core mode was accomplished by exposing the core to wet chemical etching. Light was then allowed to couple from an intermediate region near the beginning of the core exposure domain while leakage was minimised at un-etched fiber domains downstream. The primary limitation of this method was that only a small portion of the fiber could be used for signal collection. This situation is undesirable for applications such as receivers in telecommunications and sensing where extended light sources are required.

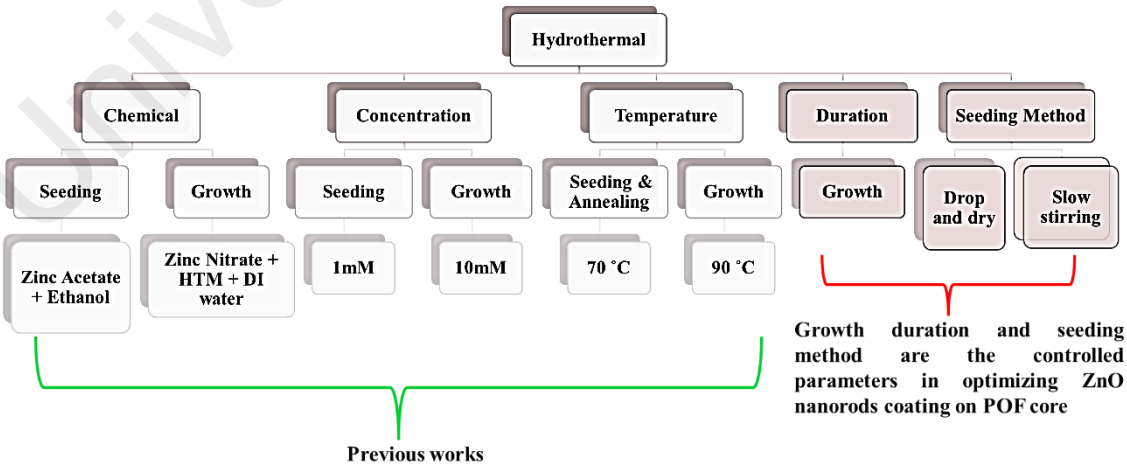

Figure 3.1 Optimization parameters for the ZnO nanorods growth on POF using hydrothermal method

The extended light source leads to less guidance of light inside the fiber resulting in low efficiency and sensitivity. To increase the magnitude of light collection, two approaches that were executed simultaneously were proposed. First, a large-core plastic fiber optic is required to increase the scattering area; and second, a structured scattering layer tightly bound to the surface of the POF is required to harvest light from different segments of the POF. The scattering layer consists of ZnO nanorods as a fiber coating. Thus, the synthesis process of ZnO nanorods through hydrothermal method needed to be optimized again due to the different specifications of POF. The POF consists of polymethyl methacrylate resin that is surrounded by a fluorinated polymer jacket that have a storage and operating temperature lower than 100 ˚C compare to multimode silica optical fiber. Hence, two important parameters are controlled in order to optimize the growth of ZnO nanorods on POF as shown in Figure 3.1. First, growth duration for a promising ZnO nanorods coating and second, seeding method to control uniformity and density of ZnO nanorods grown on POF.

3.3 ZnO Nanorods through Hydrothermal Growth

The growth of ZnO nanorods on POF using hydrothermal synthesis involves three major steps; sample preparation, seeding and growth process as depicted in Figure 3.2. These procedures are discussed in this section.

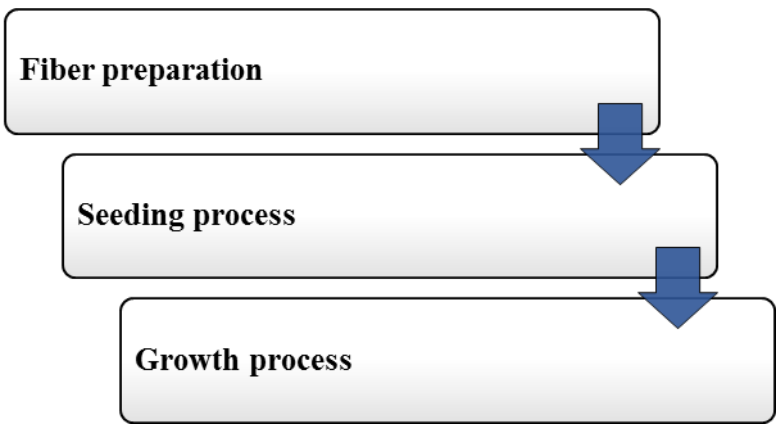

Figure 3.2 General procedures of ZnO nanorods synthesis using hydrothermal

3.3.1 Fiber Preparation

Figure 3.3 shows the process of fiber preparation to create ZnO structured growth on POF. In this work, ZnO nanorods were spirally grown on POF to increase the intensity of guided light for sensing application. Standard multimode SK-80 POF fiber (Mitsubishi Rayon Co., LTD; Japan) was used in this study as shown in Figure 3.3 (a). The outer part of the POF is a fluorinated polymer jacket with inner-outer diameter in range of 1880-2120 µm, respectively. The jacket covers the POF that consists of polymethyl methacrylate resin with diameter ranging from 1840 to 2080 µm. At first, the jacket of the POF was mechanically stripped to expose the POF over a length of 10 cm as depicted in Figure 3.3(b). Following cleansing with a dry tissue, 3M water proof plastic tape (Figure 3.3(c)) was applied to create manually spiral template along the exposed POF as shown in Figure 3.3 (d). The width of spiral pattern on POF can be varied and Figure 3.3(e) shows the width was 0.5 cm (uncovered area) to be coated with ZnO nanorods.

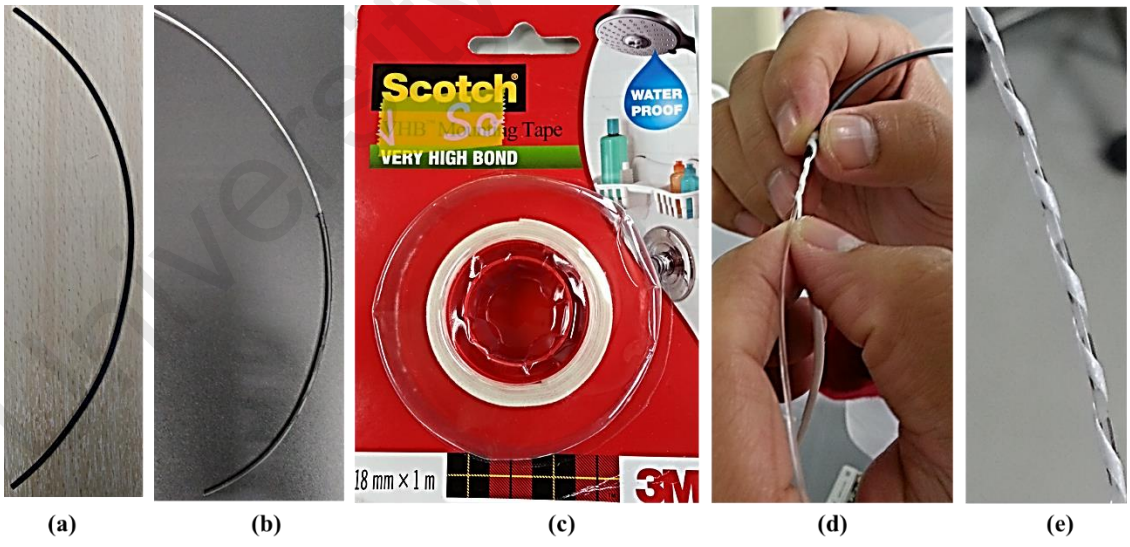

Figure 3.3 The process of fiber preparation (a) POF with black jacket (b) POF is exposed with length of 10 cm for ZnO coating (c) 3M water proof tape is used to create spiral template (d) manually creating spiral pattern on POF and (e) POF with spiral template before the synthesis process.

The tape was removed after the ZnO nanorods synthesis process to expose the bare templated POF surface before experimental characterisation and sensing. For unpatterned coating, the tape was not required to apply on the POF but ZnO nanorods were grown entirely along the POF.

3.3.2 Seeding Process

Seeding process plays a very important role in ZnO nanorod coatings on POF. The diameter, length, uniformity and density of the ZnO nanorods are primarily dependent on the seeding process. Figure 3.4 shows the procedures of seeding process which involve 4 main steps; seeding solution preparation, POF surface treatment, forming nucleation site on POF and annealing.

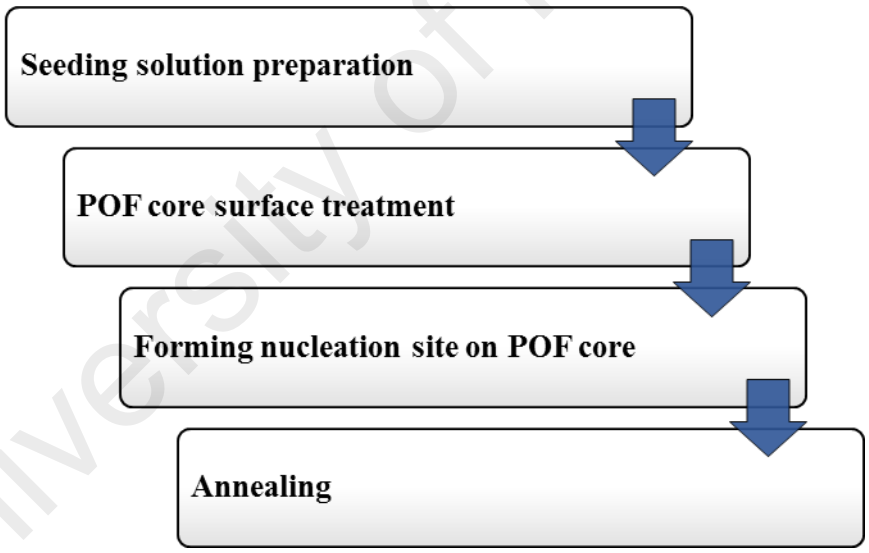

Figure 3.4 Procedures of seeding process on POF

Firstly, two different solutions were prepared in order to synthesise ZnO seed particles which are ZnO nanoparticles solution and pH controlled solution. For ZnO nanoparticles solution, ca. 0.0044 g zinc acetate dihydrate [$Zn(O_2CCH_3)_2(H_2O)_2$] (Merck KGaA, Germany) was dissolved in 20 ml of ethanol (Merck KGaA, Germany) under slow

stirring at temperature of 50 ˚C for 30 minutes to form a 1 mM solution. Then, the solution was cooled in the ambient for some time before adding another 20 ml ethanol. Figure 3.5 shows the process of ZnO solution preparation with the final amount of 40 ml.

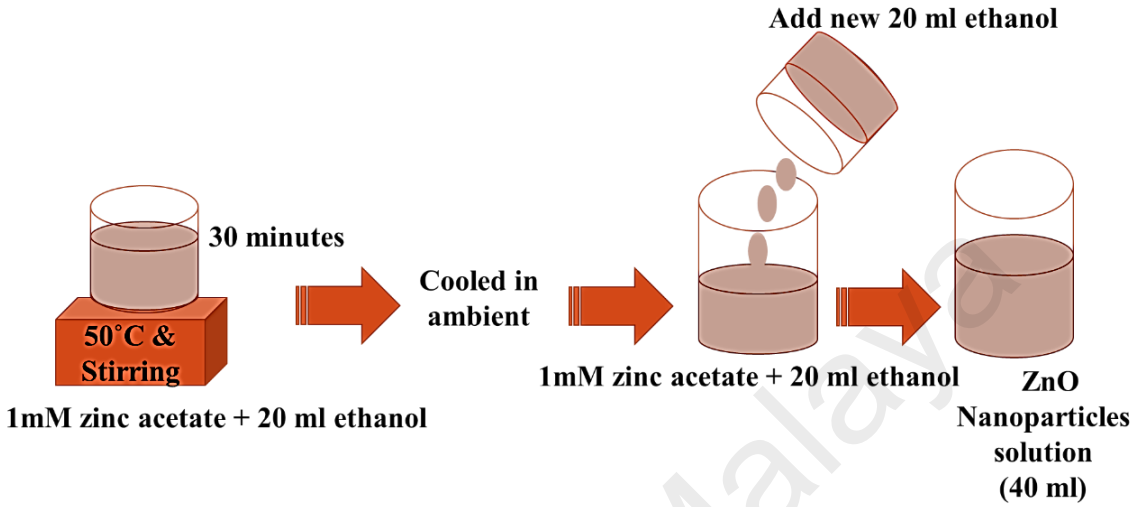

Figure 3.5 Process of 1mM ZnO nanoparticle solution preparation

The pH of ZnO nanoparticles solution is one of the important factors that influencing the ZnO properties thorough hydrothermal process. The pH can change the number of ZnO nuclei and growth units (H. Zhang et al., 2004). Sagar et al. (2007) claimed that the increase in pH (from acidic to alkaline) of the ZnO nanoparticles solution improves the growth of a ZnO film. To control the aqueous pH, a pH control solution was prepared by dissolving sodium hydroxide (NaOH) in 20 ml ethanol to form 1mM solution with temperature of 50 ˚C under slow stirring as shown in Figure 3.6.

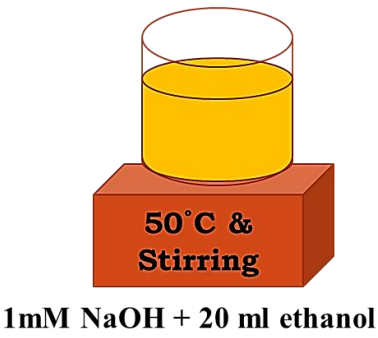

Figure 3.6 Preparation of the pH controlled solution using NaOH

After 10 minutes, the 20 ml pH control solution was added into ZnO nanoparticles solution using 1 ml pipet as illustrated in Figure 3.7. This technique provides more hydroxyl ions (OH^-) in the seeding solution (Baruah & Dutta, 2008). Then, the ZnO nanoparticles solution was slowly stirred for 1 minute for every single drop of 1 ml pH control solution. This process was repeated for 20 times. Then, the seeding solution was kept in a water bath at temperature 60 ˚C for 3 hours. As result, a noticeable change in the colour of the solution from clear to milky could be observed and pH level changed from ~ 4 to ~ 9.

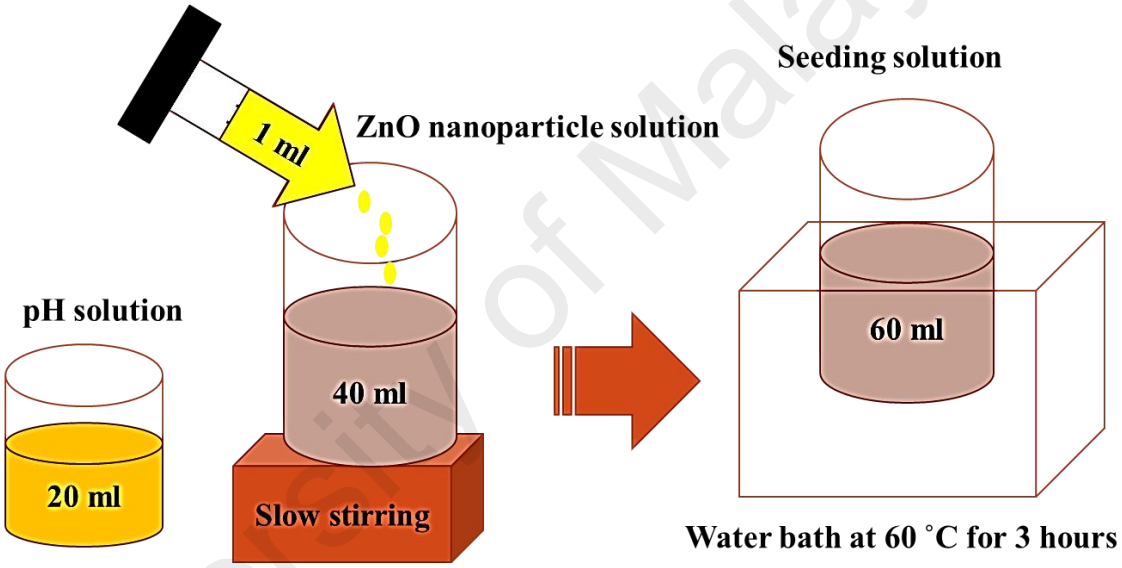

Figure 3.7 Alkaline process of ZnO nanoparticles solution by NaOH

For optimum uniformity of ZnO growth on POF, surface treatment was performed using polysorbate 80 (tween 80) which is non-ionic surfactant that contains hydrophilic group. In the process, 1 ml tween 80 was completely dissolved in 10 ml deionized (DI) water under moderate stirring with temperature of 45 ˚C as depicted in Figure 3.8(a). Then, the POF were vertically dipped into the solution for 10 minutes as shown in Figure 3.8(b). The POF samples were dried in air for 2 hours.

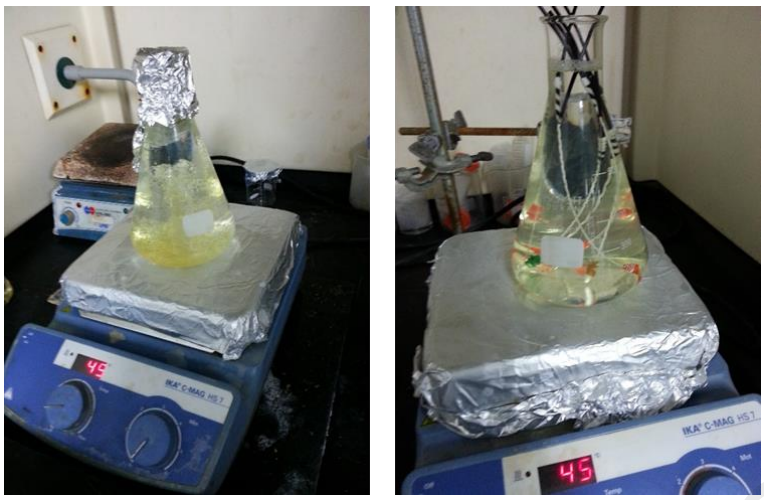

(a) **(b)**

Figure 3.8 (a) Tween 80 preparation and (b) POF surface treatment

In the process of forming nucleation site on the POF, three seeding methods were carried out in order to achieve a proper profile of ZnO nanorods growth on POF. The method used are as follows:

(i) **Dip and Dry (Figure 3.9):** The samples of POF were dipped in the seeding solution for 1 minute and dried on a hot plate at a temperature of 70 ˚C for 1 minute. This process was repeated for 10 times. Following the conclusion of the dipping process, the POFs were annealed at 70 °C for 3 hrs.

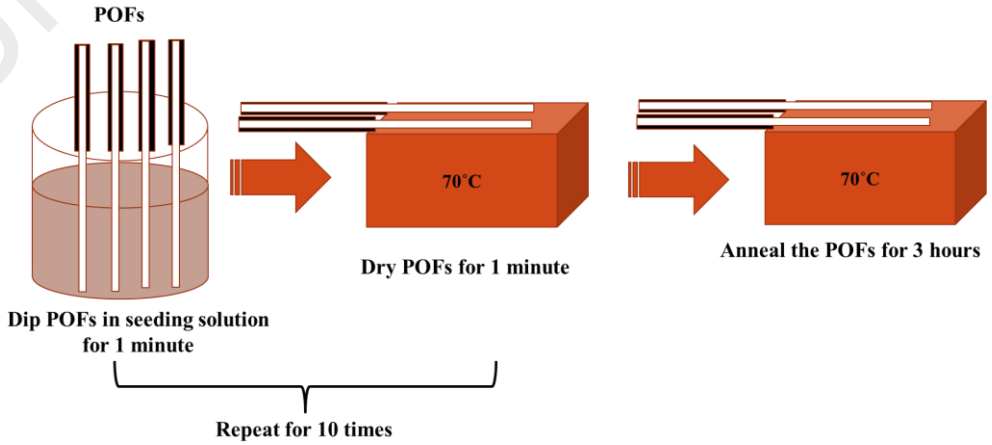

Figure 3.9 Dip and Dry method in seeding process

(ii) **Drop and Dry (Figure 3.10):** The samples of POFs were placed on a hot plate at a temperature of 70 ˚C. The seeding solution was dropped on the POFs with amount of 100 µl using micro-pipet and wait for 1 minute to dry the POFs. The process was repeated for 10 times. Then, the POFs were annealed at the same temperature for 3 hours.

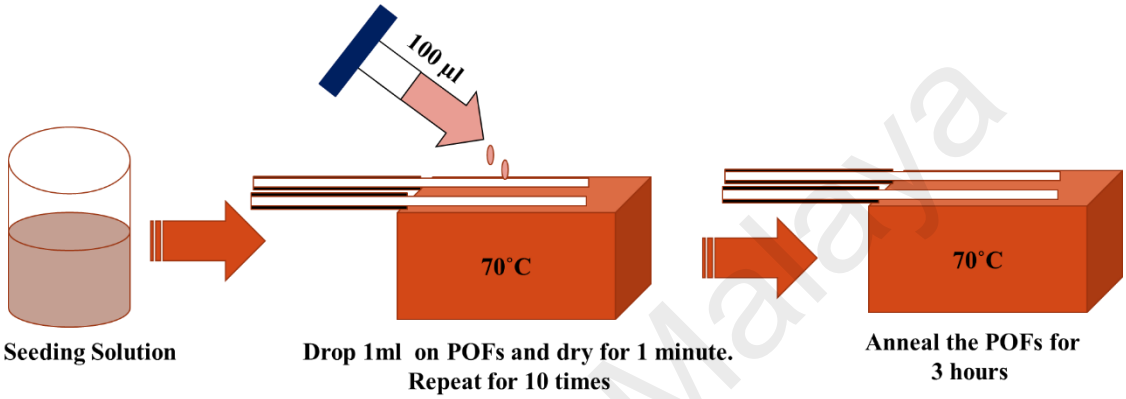

Figure 3.10 Drop and Dry method in seeding process

(iii) **Slow stirring (Figure 3.11):** In the method, the exposed POFs were immersed in the seeding solution under slow stirring for 30 minutes. This method can avoid the ZnO nanostructure to attach with redundancy on the POFs. The seeding process was also concluded by annealing the POFs for 3 hours at 70 ˚C.

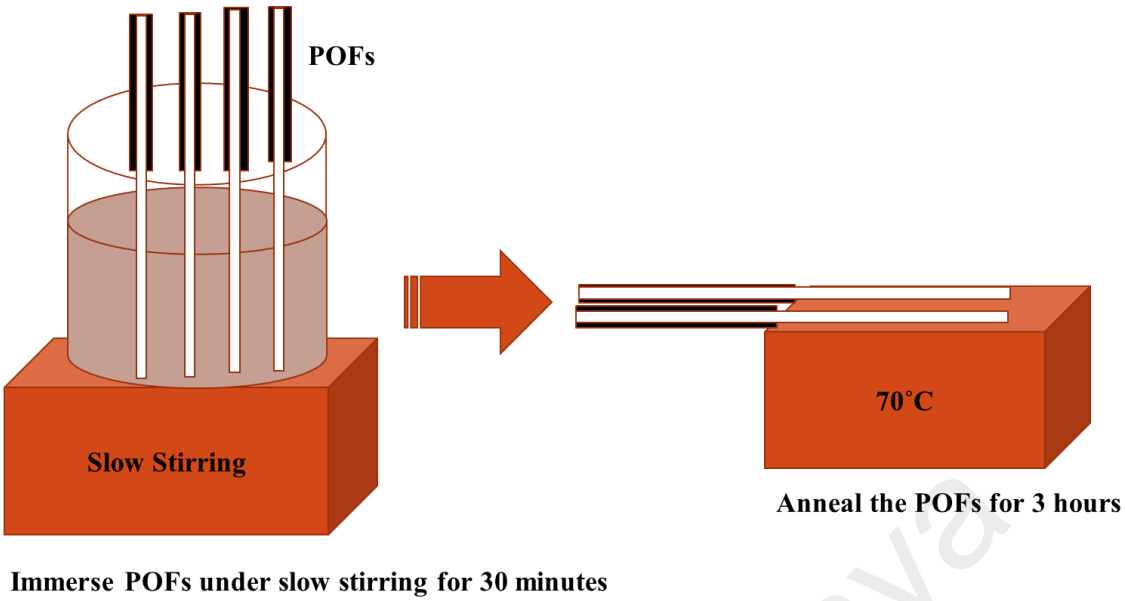

Figure 3.11 Slow stirring method in seeding process

3.3.3 ZnO Nanorod Growth Process

ZnO nanorods were grown following the seeding process. 2.97 g zinc nitrate hexahydrate [$Zn(NO_3)_2 \cdot 6H_2O$] (Ajax Finechem Pty Ltd) and 1.40 g of hexamethyleneteramine or HMT [$(CH_2)6N_4$] (Sigma-Aldrich) were dissolved in 1000 ml of deionised (DI) water to form 10 mM solutions of each compound. The seeded POFs were then vertically placed in 200 ml of the synthesis solution and heated in an oven set at 90 °C as shown in Figure 3.12. Following 5 hours of heating, the solution was discarded and replaced with a new solution in order to maintain constant growth conditions (Baruah & Dutta, 2009b). Growth time was varied from 8 to 20 h. Following synthesis, POFs were removed and rinsed several times with DI water.

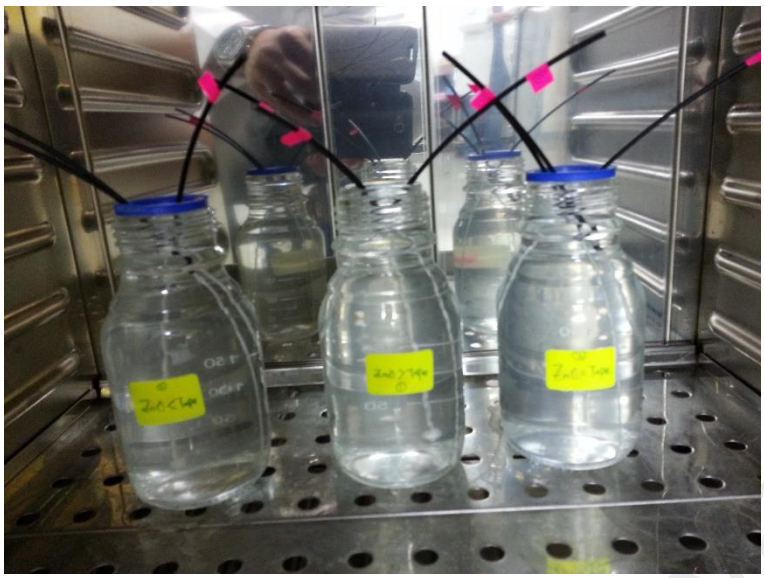

Figure 3.12 The process of ZnO nanorod growth on POFs

3.4 Optimization of ZnO Nanorod Growth on POF

The synthesis of ZnO nanorod growth on POF as explained in section 3.3 was optically optimized to investigate light scattering into the POF towards light side coupling. In seeding process, the dip and dry method was applied in order to deposit ZnO nanoparticles on the POF. The profile of ZnO nanorods growth on the POF was as well characterized using scanning electron microscopy (SEM) and Energy dispersive X-ray (EDX). The entire process of the optimization is summarized accordingly as depicted in Figure 3.13.

The hydrothermal growth was firstly performed to grow ZnO nanorods on POF for 20 hours at a temperatures as low as 90 ˚C (J. H. Kim et al., 2007; T.-U. Kim, Kim, Pawar, Moon, & Kim, 2010; Tam et al., 2006) with and without the surface treatment process. The obtained ZnO nanorords coated POF were then characterized by SEM (model: Hitachi, 3400N) and EDX was performed during SEM.

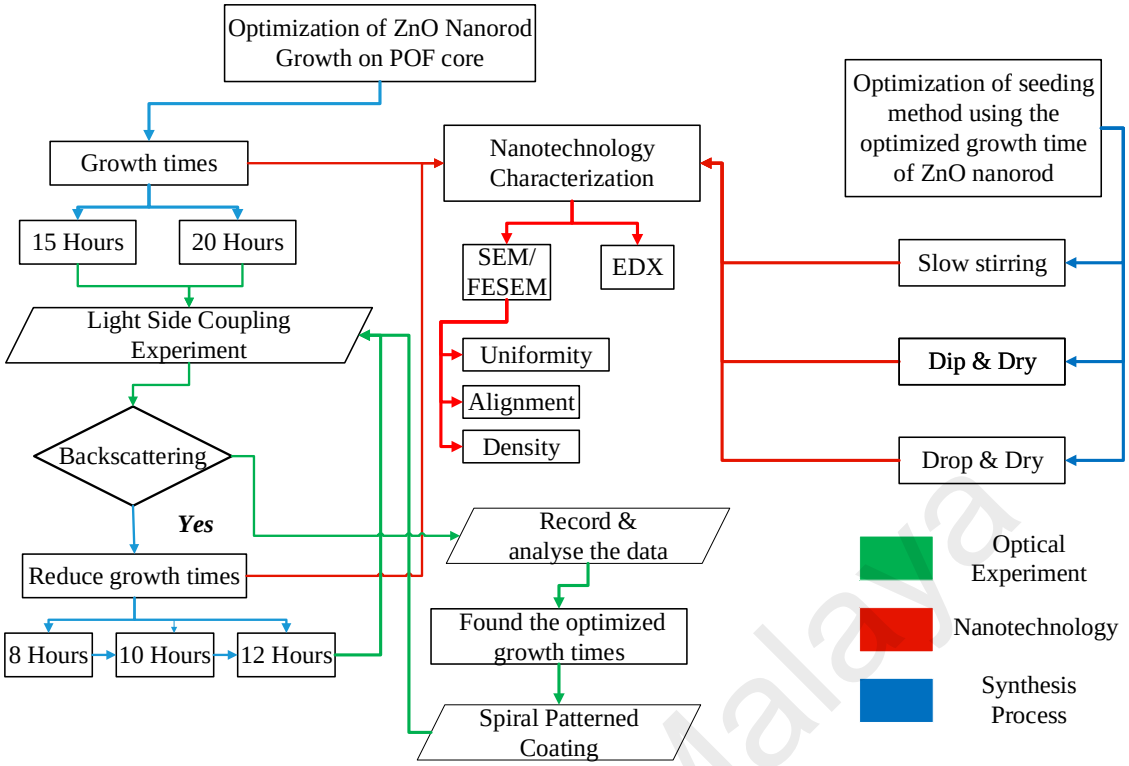

Figure 3.13 Flow of the optimization process of ZnO nanorod growth on POF through hydrothermal

Figure 3.14 shows the SEM images of ZnO nanorods grown on the POF for 20 hours with surface treatment (Tween 80) and without surface treatment, respectively. These POF samples were observed at low magnification in order to compare the distribution of ZnO coating layer attached on the POF. It was obtained that the POF treated with Tween 80 has a good coating of ZnO layer as shown in Figure 3.14 (a) compare to the untreated POF as depicted in Figure 3.14 (b). The result clearly shows that the coating of ZnO layer was not firmly attached on the untreated POF. It can affect the intensity of guided light inside the POF due to less light scattering.

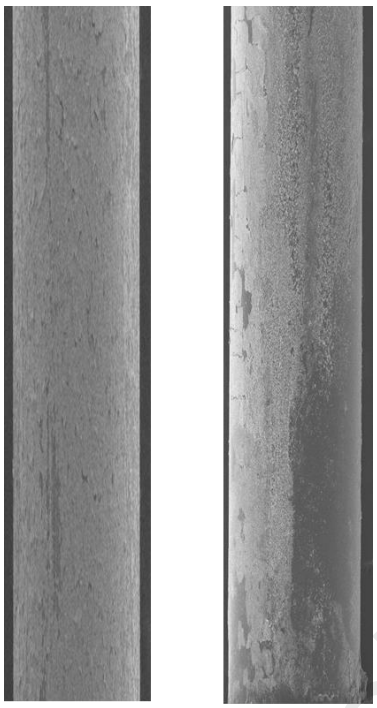

Figure 3.14 Low magnification SEM images of the POF coated with ZnO nanorods with (a) surface treatment (Tween 80) and (b) without surface treatment

For onward ZnO synthesis process, the surface treatment becomes a compulsory procedure before seeding the POF with ZnO nanoparticles. Then, the unpatterned POF samples coated with ZnO nanorods were prepared for two different growth time; 15 hours and 20 hours. The POF samples were optically characterized towards light side coupling. The optical characterisation apparatus is schematically depicted in Figure 3.15 below.

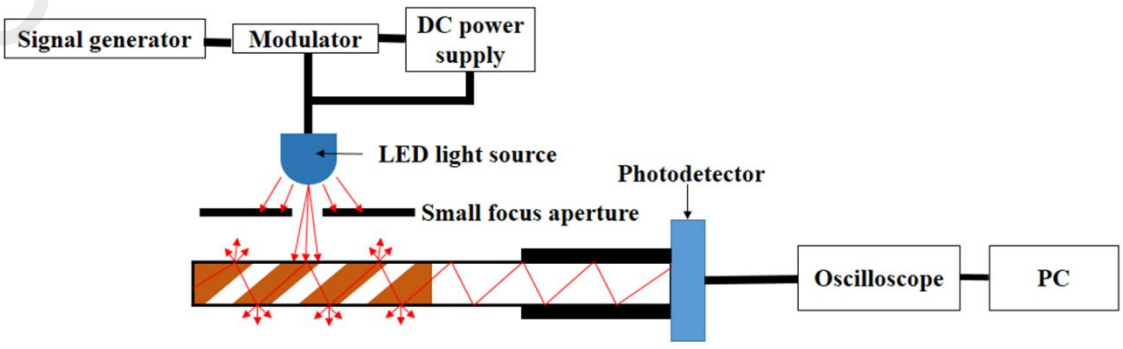

Figure 3.15 V_{pp} characterisation setup to measure the side coupling of ZnO nanorods for unpatterned and spiral patterned POFs

The magnitude of the side coupling was measured in terms of 'peak-to-peak' voltage (V_{pp}) following excitation by a modulated light-emitting diode (LED) red light source – e.g. the extended light source as depicted in Figure 3.16. Light from the extended source was restricted by an aperture onto specific sites on the POF in order to optimise the growth conditions for maximum side coupling. The egress end of the optical fiber is linked to a digital oscilloscope and subsequently to a computer for data recording and analysis.

Figure 3.16 The modulated LED red light source used in the optical characterization

POFs were illuminated by a 3 cm diameter broad band LED extended light source placed 10 cm from the fiber surface. A rectangular aperture 1 × 3 cm was placed perpendicularly to and directly on top of the fiber during signal acquisition. Three regions were inspected for the unpatterned type of fiber: (i) the interfacial area between the ZnO coating and the uncoated fiber near the detector end; (ii) the middle ZnO region; and (iii) the tip that consisted of the terminal ZnO-air interface as illustrated in Figure 3.17. The fiber tip was covered in all cases except for readings taken for the tip of the POF samples and the tip reading is not considered for any purpose in this work. In addition, the tip reading is changeable for each sample due to the edge of the tips.

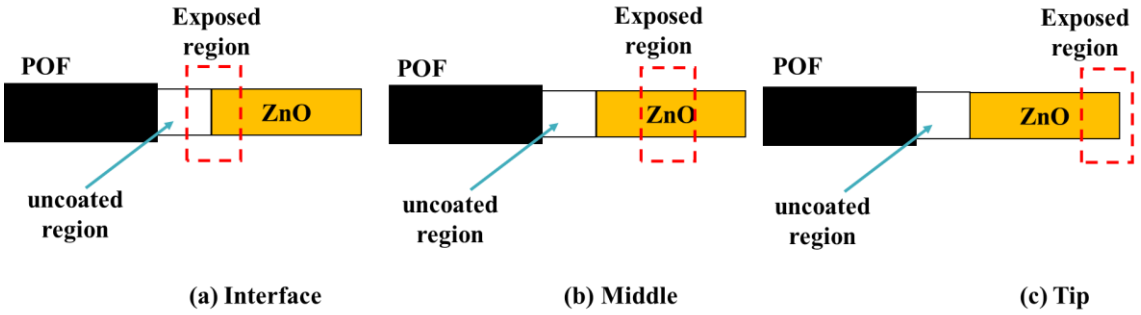

Figure 3.17 The exposed regions on the unpatterned type of POF (a) interface, (b) middle and (c) tip

The plots in Figure 3.18 shows the average V_{pp} on bare and unpatterned POFs for 15 hours and 20 hours. However, the average V_{pp} at the interface region (for both these growth times) was greatly reduced due to backscattering that limits light side coupling to the core modes. This backscattering problem also contributed to increase the average V_{pp} at the ZnO region for 15 and 20 hours due to the presence of ZnO nanorods not inducing light leakage. The bare POFs did not show any backscattering effects and very low forward light scattering. The backscattering problem occurred due to longer growth times, resulting in higher ZnO nanorods density on POFs as shown in Figure 3.19 for 15 hours and 20 hours, respectively. Hence, the coating provided a greater barrier to light side coupling due to backscattering. The SEM images of ZnO nanorods are captured at a magnification of 25.00 kX clearly showed that the ZnO nanorods were not vertically grown on POFs. This profile as well contributes to produce high backscattering and low intensity of guided light.

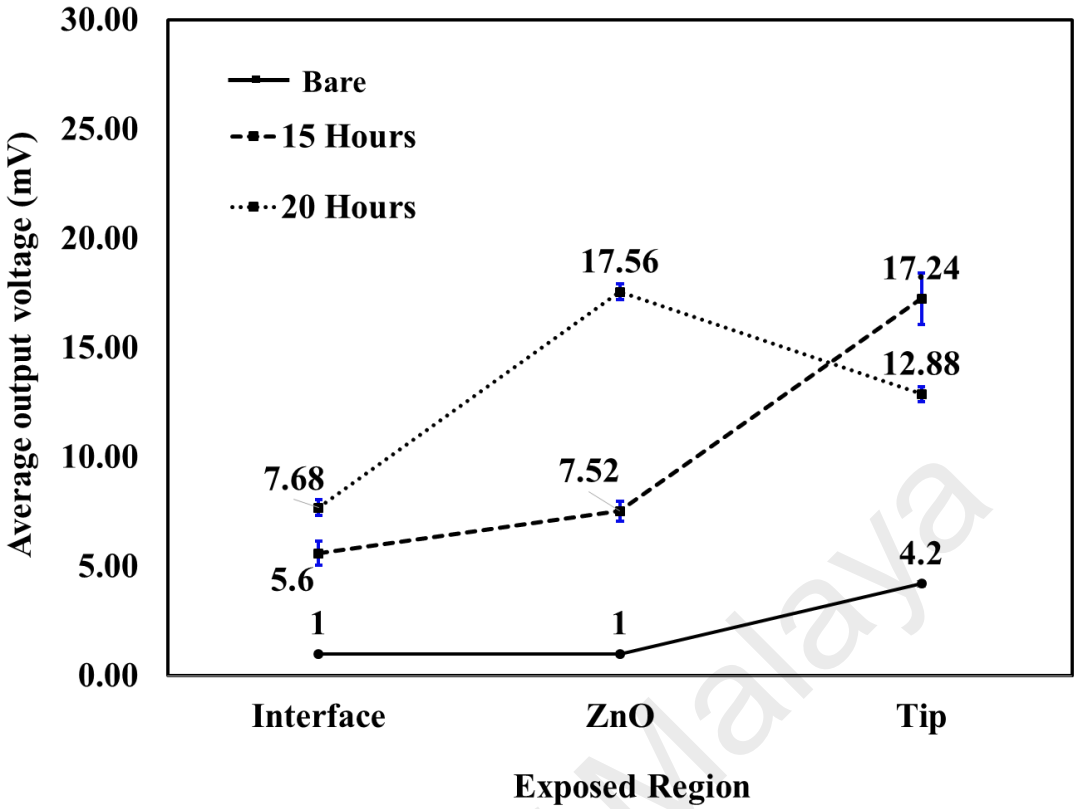

Figure 3.18 Average V_{pp} for 15 and 20 hours growth time with backscattering effects

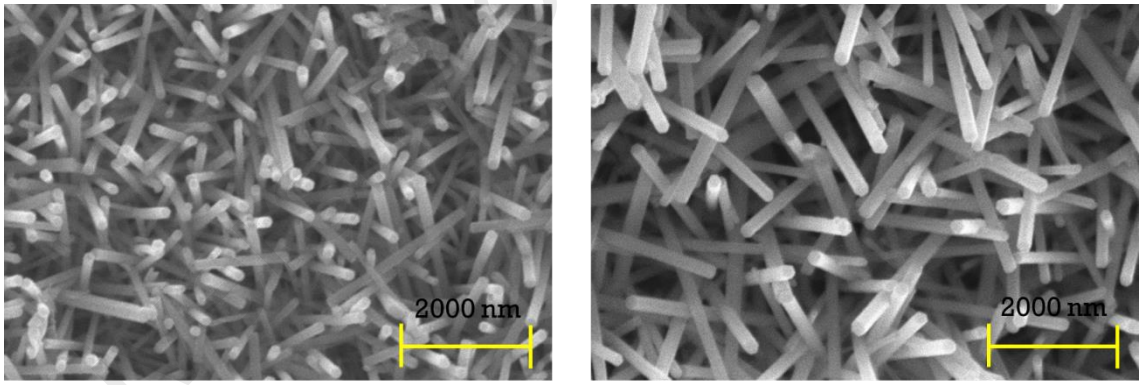

Figure 3.19 ZnO nanorods grown on POF (a) 15 hours (b) 20 hours

The problem was solved by reducing the ZnO nanorods growth duration to 8, 10, or 12 hours by applying the same synthesis process of ZnO nanorods as explained in section 3.3. Figure 3.20 shows the improvement in the average V_{pp} at interface regions for the above mentioned growth durations: 8, 10, and 12 hours. As the extended light source was shined at middle regions, the average V_{pp} significantly reduced due to ZnO

nanorods induced light leakage through the core modes. At interface region, the average V_{pp} greatly increased due to more light coupled inside the core. However, it was determined that the growth duration of 12 hours was optimal in limiting backscattering. Tip readings (uncovered) are high due to ingress of light through the fiber optic in addition to potential side coupling.

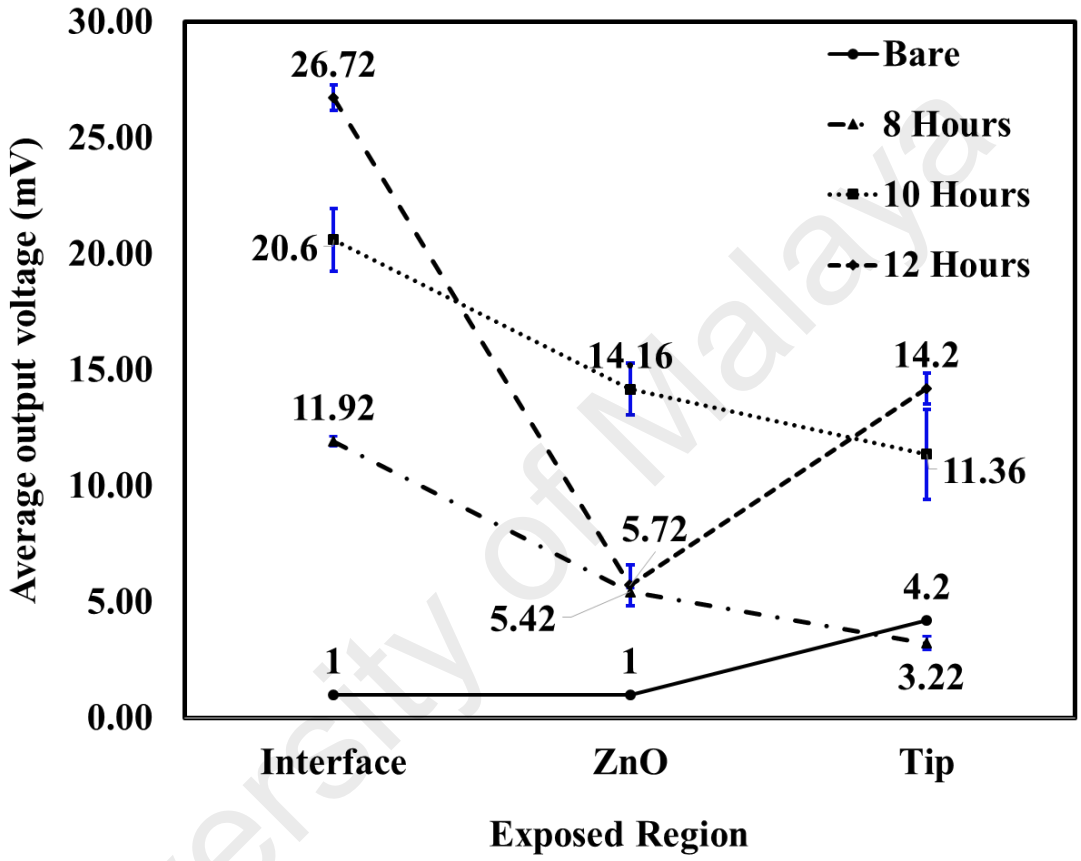

Figure 3.20 Backscattering effect is eliminated at interface regions after reducing the growth time to 8, 10, and 12 hours

The optimized condition was concluded based on the highest average V_{pp} at the interface region. The results of optimisation are summarised in Figure 3.21 showing only V_{pp} against interface data. At 12 h growth time, V_{pp} is maximized, thereby demonstrating high light side coupling with reduced leakage due to backscattering. This optimized process of growing ZnO nanorods on POF was then applied to fabricate the spiral patterned growth on POF as shown in Figure 3.3.

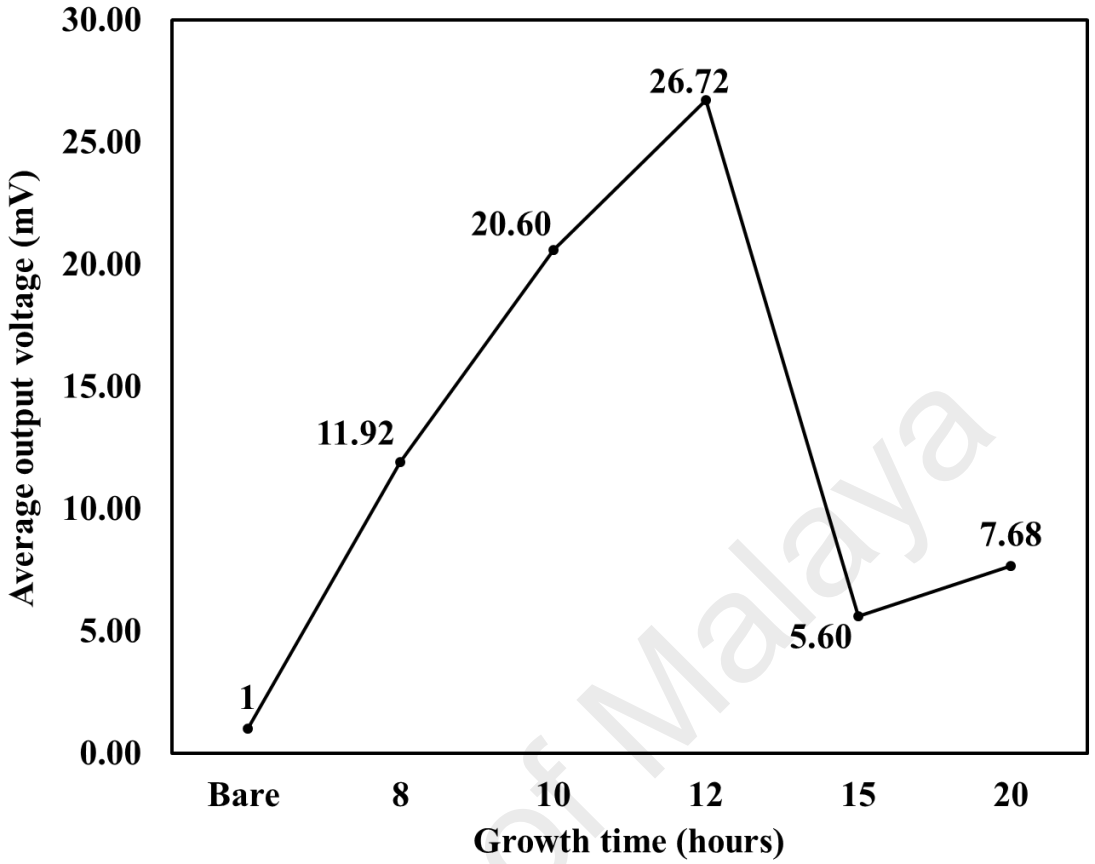

Figure 3.21 Average V_{pp} at interfacial area for all growth times

Meanwhile, the growth of ZnO nanorods on POFs for the growth durations; 8, 10 and 12 hours were also characterized and analysed through SEM images as shown in Figure 3.22. For ZnO nanorods grown on POF for 8 hours, it was observed that the thickness of ZnO coating layer was very thin and detached. Some parts of the coating layer were not properly grown with ZnO nanorods. The growth of ZnO nanorods was seen like a wave because the length was not proper uniform and short due to a short growth duration. The growth of ZnO nanorods for 10 hours also showing an improper coating layer but the thickness has a slight improvement due to the elongation of ZnO nanorods. However, the orientation of ZnO nanorods is not homogenous as desired. A better improvement in ZnO coating layer can be clearly seen for 12 hours, only a few small parts were not coated and a strong attachment with the POF was achieved.

Therefore, the ZnO nanorods were not distributed appropriately on the POF and few patches of ZnO flowers were presented among the nanorods.

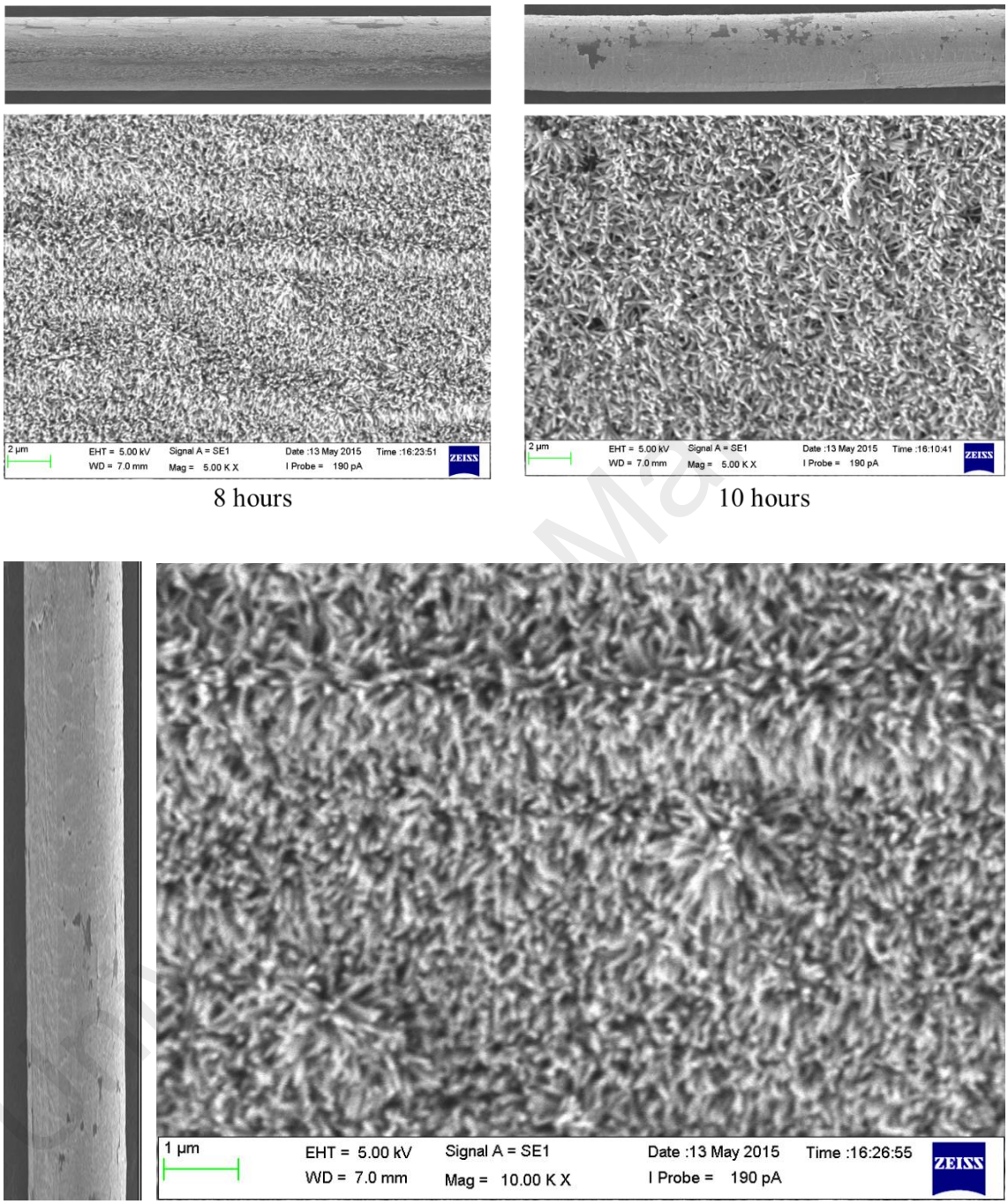

Figure 3.22 The SEM images for growth durations: 8 hours (top left), 10 hours (top right) and 12 hours (bottom)

3.4.1 Spiral Patterned Growth of Zno Nanorods on POF Using the Optimized Growth Duration.

For spiral patterned POF, the POF samples were prepared following the steps as shown in Figure 3.3. The synthesis process was performed as explained in section 3.3 with the optimized growth duration. For optical characterization, five ZnO regions were analysed: (Interface 1) the interfacial area between the ZnO coating and the uncoated fiber near the detector end; (ZnO 1) the adjacent pure ZnO region; (Interface 2) a second interfacial domain between the ZnO and the uncoated fiber; (ZnO 2) a second pure ZnO region; and (Tip/ Interface 3) the tip domain of ZnO and air as before (uncovered during reading taken for the tip) as illustrated in Figure 3.23. In all cases, bare POFs devoid of ZnO coating served as controls in the experiments. Five readings were acquired for each measurement.

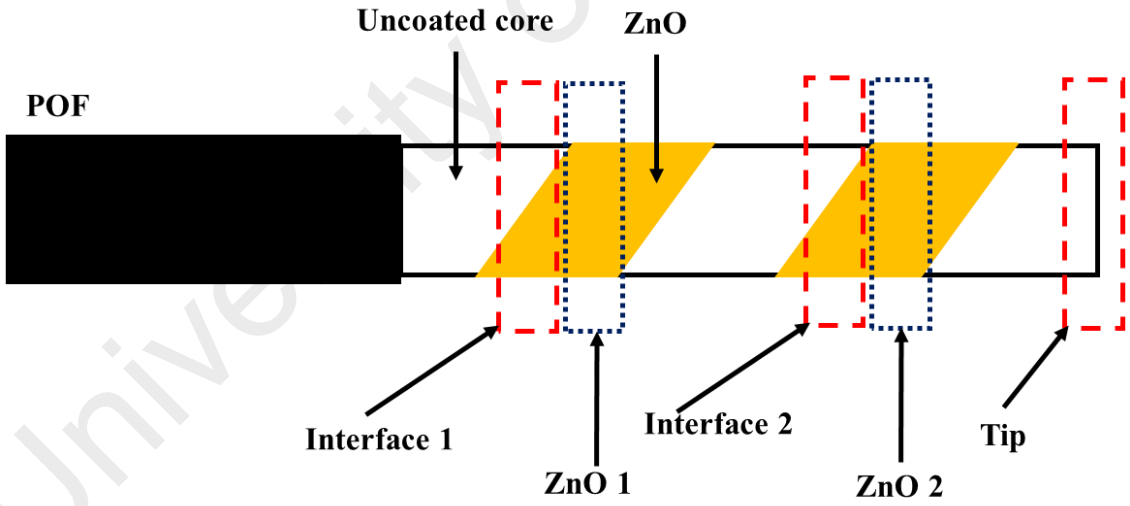

Figure 3.23 The specified regions on the spiral patterned POF for optical characterization.

The same characterization setup as performed for the unpatterned POF was used to investigate the side coupling in term of 'peak to peak' voltage (V_{pp}) as shown in Figure 3.15. The graph of average V_{pp} for the five regions on the spiral patterned growth is depicted in Figure 3.24. V_{pp} was highest at Interface 1, the ZnO bare interface closest to

the detector. V_{pp} was significantly lower at ZnO 2, the pure ZnO region. A slight rise in V_{pp} was observed at Interface 2, another interfacial region. ZnO 2, a pure ZnO region located further from the detector showed similar values to ZnO 1. Interface 3 showed the tip effect as before. Therefore, the spiral patterned on the POF has potential application as multi-channel excitation and enhance the total coupling inside POF. It is worth mentioning that V_{pp} was a factor of 2x lower than for the same region (interfacial region closet to photodetector) on the unpatterned fiber. This is due to area reduction of the spiral structure as shown by the inset in Figure 3.24. This is not the case when an extended light source was used.

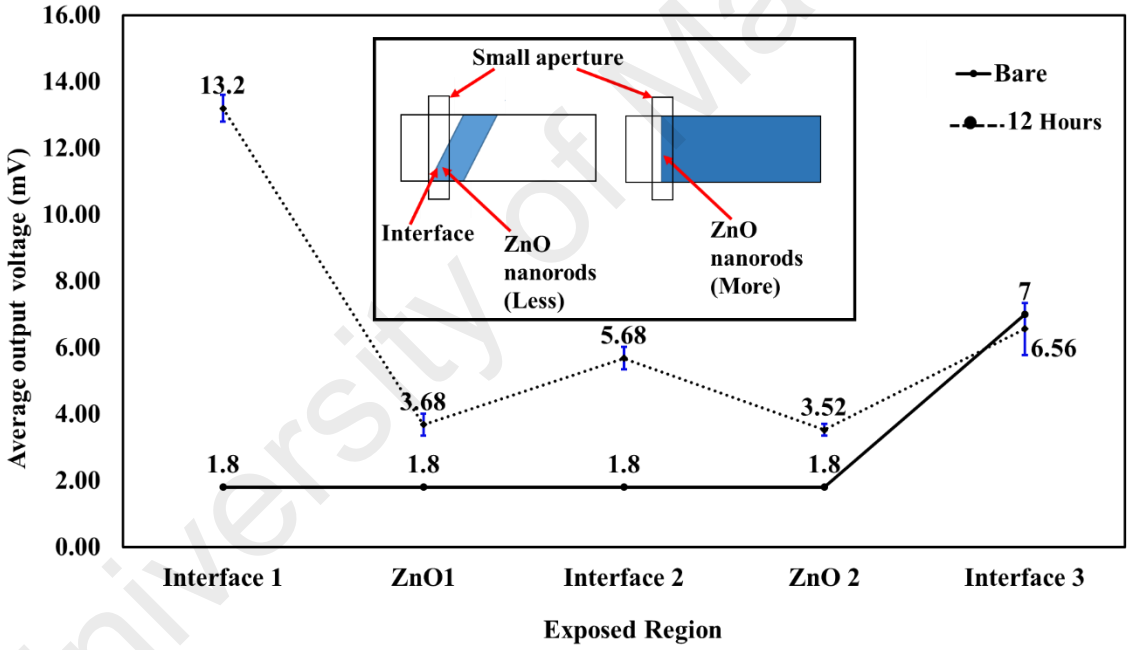

Figure 3.24 Average Vpp for the spiral patterned growth for 12 h which has more than one interface and ZnO regions. The inset shows the regions covered by the aperture when characterisation the structured and unstructured ZnO growth on POF

Figure 3.25 shows the SEM image of ZnO spiral patterned growth on POF for 12 hours. The SEM image in Figure 3.25 (a) with magnification set at 13.00 kX was used to observe the ZnO spiral pattern on the POF. The ZnO coating layer strongly attached on the POF with proper orientation. Figure 3.25 (b) depicts SEM images with magnification

of 25.00 kX which clearly shows vertical alignment, high density (63 nanorods/1.23 × 10^{-12} m^2 = 510 × 10^{11} nanorods/m2) and uniform distribution of ZnO nanorods on the POF.

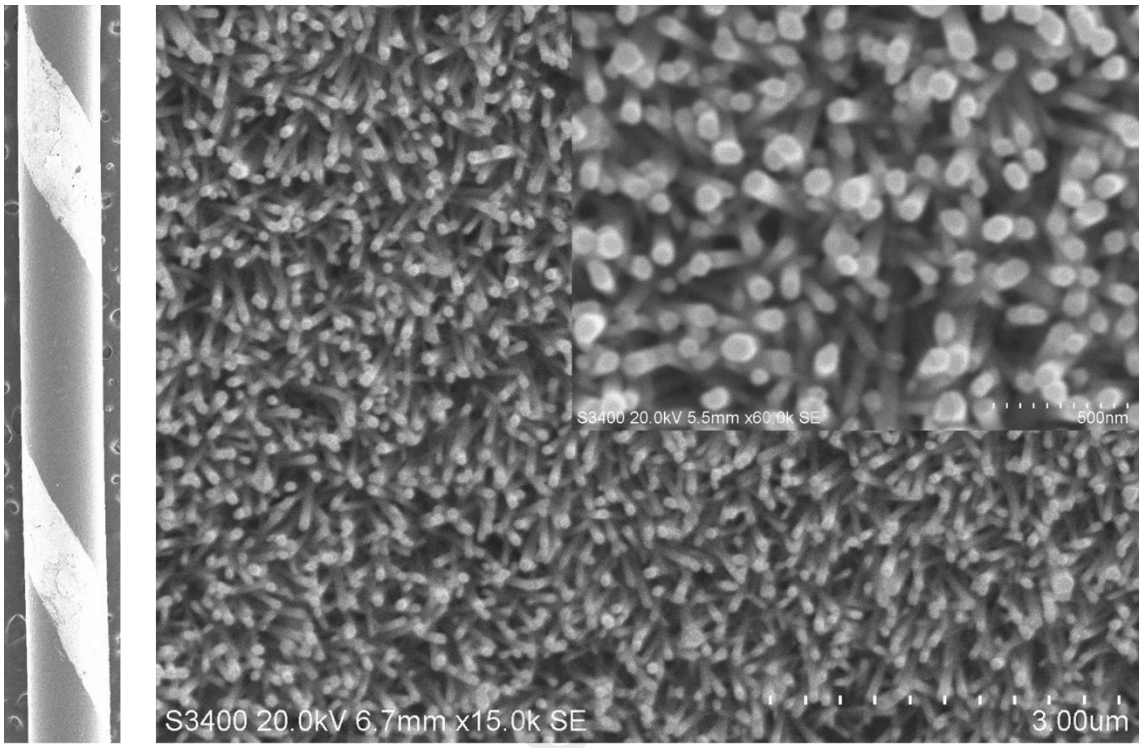

(a) (b)

Figure 3.25 (a) 13 kX SEM image of ZnO spiral patterned growth after synthesis (b) 25.0 kX SEM image of the nanorods and Inset: The ZnO nanorods at 60.0 kx magnification for 12 hours

The EDX spectra was performed during SEM to verify the nature of the species attached on the POF and to allow a rough estimation of their relative amounts. The EDX elemental analysis revealed that the topcoat layer consisted only of zinc and oxygen as shown in Figure 3.26. The presence of Zinc indicates a high peak at about 1.0 keV and oxygen peak appears at 0.35 keV.

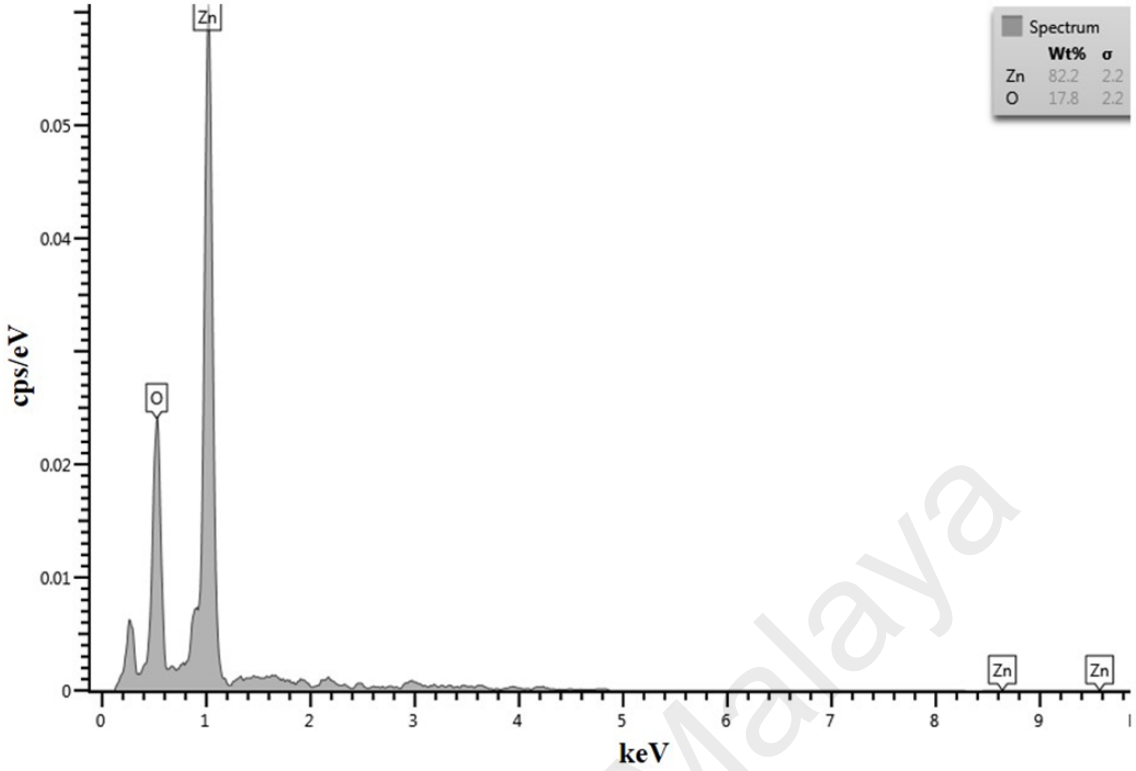

Figure 3.26 EDX spectrum of ZnO nanorods showing zinc and oxygen peaks

3.5 Optimization of Seeding Methods to Improve the Growth of Zno Nanorods on POF.

The SEM images in section 3.4 showing the morphology of ZnO nanorods grown on POF was not proper as desired due to cylindrical surface of POF compare to flat surfaces that promises a high guarantee for easily controlling the morphological parameters such as alignment, density and uniformity. Deposition of ZnO nanoparticles during seeding process plays an important role in the hydrothermal growth of ZnO (Baruah & Dutta, 2009a). In an attempt to improve the morphology of ZnO, another two seeding methods were carried out as explained clearly in section 3.3.2; drop-dry and continuous slow stirring method. The nanorods were then grown following the conventional growth process. The SEM images of ZnO spiral patterned growth on POF using drop and dry method as depicted in Figure 3.27.

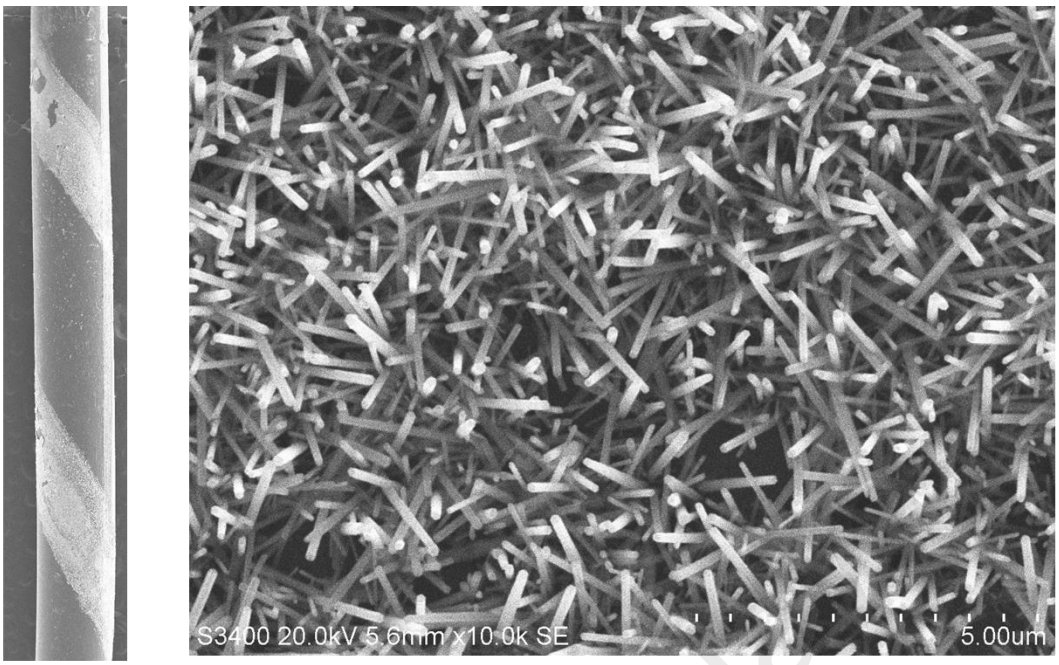

(a) (b)

Figure 3.27 The growth of ZnO nanorods using the drop and dry method (a) 5 kX SEM image of spiral patterned growth on POF and (b) the morphology of ZnO nanorods at a high magnification

It was observed that the ZnO nanorods were successfully coated on the POF but with low density. At the high magnification, it can be seen that the ZnO nanoparticles agglomerate during the seeding process to form bigger clumps. This can be attributed to occur due to the surface tension of the solvent (ethanol) which brings the particles together during the drying process (Dutta & Hofmann, 2004). The gradual evaporation of the solvent from the surface of the POF leads to cracks in the layer of the ZnO nanoparticles grown on the POF. As the particles are brought together due to surface tension of the solvent during evaporation, it is unlikely that the crystallites would be preferentially oriented on the POF (M. Wang & Zhang, 2009). As a result of multifarious orientations of the seed crystallites, the nanorods grow in various directions resulting an agglomerated nanorods like growth as illustrated in Figure 3.28.

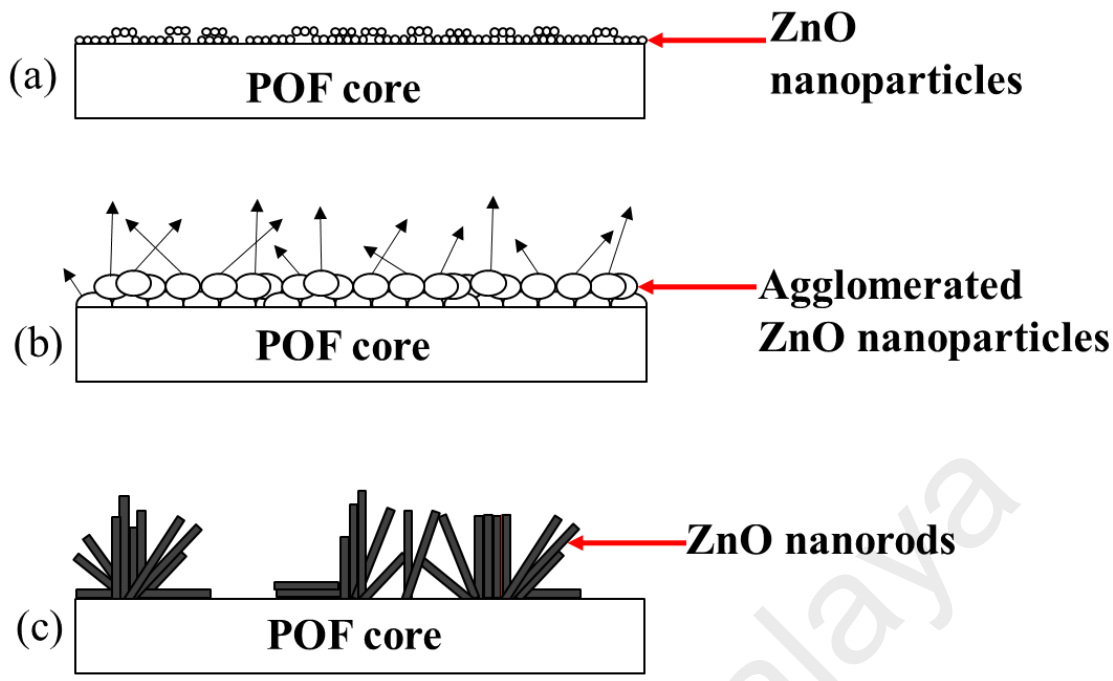

Figure 3.28 Schematic diagram showing the possible agglomeration of ZnO nanoparticles upon evaporation of the solvent (a) thin layer of ZnO nanoparticles (b) agglomerated clumps of ZnO nanoparticles with various orientations and (c) ZnO nanorods grow from the seed crystallites in the different directions

To obtain highly oriented growth on POF, continuous slow stirring method through direct hydrolysis proved to be a more promising technique than using pre-synthesized ZnO nanoparticles seeds self-organised on the POF as discussed above. Figure 3.29 shows the POFs were being dipped in the seeding solution for 30 minutes under continuous slow stirring which is able to avoid the agglomeration of ZnO nanoparticles. Orientation of the ZnO nanoparticles formed in the thin film grown on the POF.

Figure 3.29 The continuous slow stirring process

Figure 3.30 shows the SEM image of the ZnO growth on the POF with the continuous slow stirring method in seeding process. It was interesting to observe that not only did this seeding process give uniform growth in the inner layers of the mesh, but it also eliminated the formation of the loosely bound agglomerates. No microstructures could be observed sitting on the nanorods.

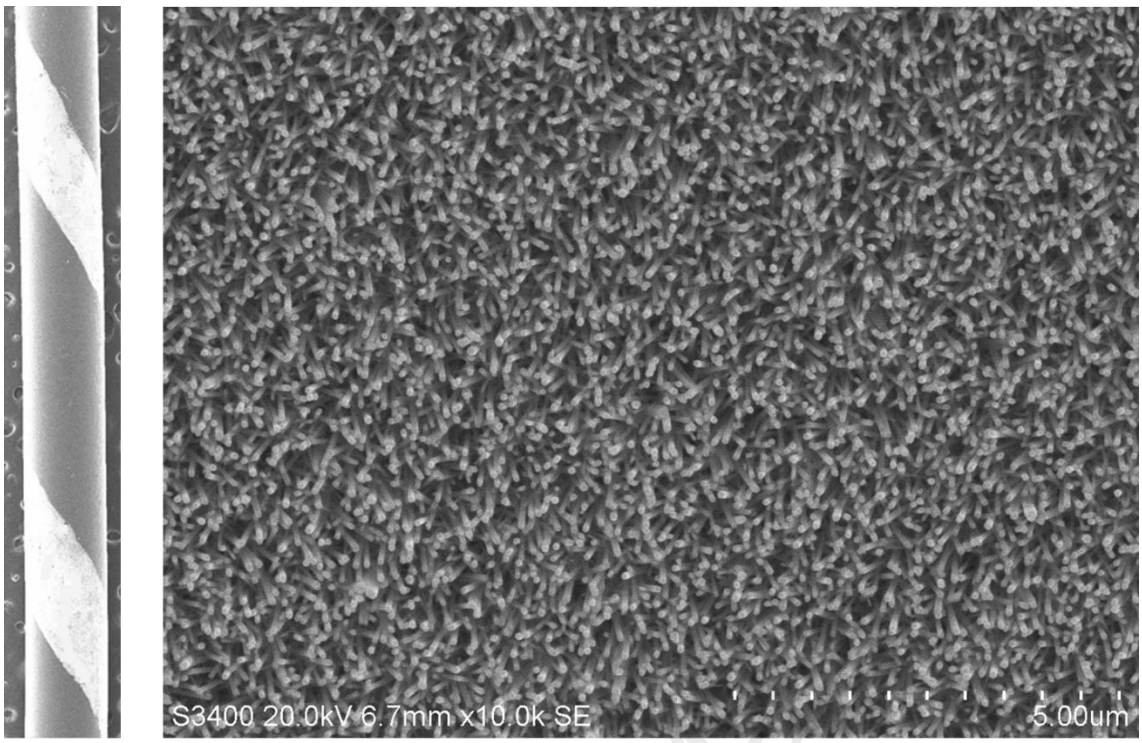

(a) (b)

Figure 3.30 The growth of ZnO nanorods using the continuous slow stirring method (a) 5 kX SEM image of spiral patterned growth on POF and (b) the morphology of ZnO nanorods at 10.0 kX

3.6 Summary

ZnO nanorods were grown by the hydrothermal method directly onto POF. The morphology of the ZnO nanorods could be varied through changes in growth duration and seeding methods. The synthesis process to grow ZnO nanorods on POF was optimised by maximising the side coupling to POF from an extended light source. Backscattering occurred due to high density of ZnO nanorods growth for 15 and 20 hours, resulting less coupling light inside the POF. This problem was solved by varying the growth duration to 8, 10 and 12 hours. ZnO nanorods growth time of 12 hours and temperature of 90 °C provided the best coupling voltage. This work also reports a novel spiral patterned growth of ZnO nanorods on POF. Structuring the growth to specific regions allows scattering from different segments along the POF to contribute to the total

coupled power. Seeding methods were as well optimized in this work because it is very important to control the growth and orientation of ZnO nanorods on the POF. Vertically aligned ZnO nanorods were obtained on the POF using a continuous slow stirring during the seeding process.

CHAPTER 4: CHARACTERIZATION OF LIGHT SIDE COUPLING TOWARDS MULTIPLE OPTICAL CHANNEL AND OPTIMIZATION OF SPIRAL PATTERNED WIDTH OF ZINC OXIDE NANOROD COATING FOR OPTIMAL SIDE COUPLING

4.1 Introduction

The numerous breakthroughs in photonics that have taken place over the last 50 years gave rise to many applications using light scattering which often involves a considerable amount of interdisciplinary knowledge. Chemists and physicists have utilized light scattering such as small angle x-ray scattering (SAXS) to study the size and shape of macromolecules in solution as well as a whole range of materials including colloidal suspensions and solid polymers (Agbabiaka, Wiltfong, & Park, 2013; Lipfert, Columbus, Chu, Lesley, & Doniach, 2007). A classical text with title “Light Scattering by Small Particles” (Hulst & Van De Hulst, 1957) and the comprehensive book on "The Scattering of Light and Other Electromagnetic Radiation" (Kerker, 1969) were widely referred for a deeper understanding of the dynamical properties of systems often requires theoretical and experimental examinations of the scattering phenomena.

Nowadays, ZnO has received tremendous interest as a scattering element especially on various flat surfaces for many optical applications such as solar cells (Berginski et al., 2007; Krč, Zeman, Kluth, Smole, & Topič, 2003), bio-imaging (Wu et al., 2007) and etc. However, there are not many research attempts so far to develop a patterned ZnO growth. The application of a spiral patterned ZnO nanorods with mm dimensions on cylindrical surfaces with small diameter (e.g. ca. 2 mm) of a typical optical fiber has still not been explored for optical applications. Practically, unpatterned growth is preferred due to reduced complexity during fabrication and shorter treatment time. As

examples, some applications have been demonstrated with unpatterned growth of ZnO coating on POF (Bora et al., 2014; H Fallah et al., 2013). However, it was found that although unpatterned ZnO nanorod layers enhanced optical side coupling with the fiber, significant levels of backscattering prevented the ingress of light into the fiber. Furthermore, ZnO scattering centers provided a pathway for light leakage (Hoorieh Fallah et al., 2014). Consequently, these two optical loss mechanisms resulted in low intensity of side coupling of light, a condition that is undesirable in optical applications such as in telecommunications, sensing and measurements. As explained in previous chapter, in order to increase the intensity of side-coupled light, application of spiral patterned coatings of ZnO nanorods on POF was proposed to mitigate the level of backscattering and leakage.

This chapter will focus on two main objectives of this research work. First, the spiral patterned coatings of ZnO nanorods on POF through continuity of the optimized hydrothermal synthesis will be optically characterized towards light side coupling of multiple optical channel. In this characterization, spectral analysis is performed for the unpatterned and spiral patterned samples to identify the wavelength coupling maxima. A broad spectrum white light source and two infrared laser sources were used (850 and 980 nm). The optical transmittance of patterned and unpatterned POFs is compared by computing the coupling efficiency. Second, an optimization of the spiral spacing of ZnO nanorod coated regions on the POF was carried out to produce maximal signal intensity. Theoretically, high intensity light side coupling is expected between the scattering ZnO layer and the fiber optic if the width of the ZnO spirally-patterned coating is optimized for the purpose of experimental design.

4.2 Mechanism of Light Scattering by ZnO Nanorod

It is worth mentioning here that across this thesis and in a previous publication (H Fallah et al., 2013) , the term scattering is used to describe the main phenomenon corresponding to side coupling as shown in Figure 4.1. It was reported that another important factor has been observed to actually contribute into coupling light to the guided modes inside POF particularly at large angles, θ_i, (near right angles). At angles close to 90°, light is guided inside the rods because ZnO nanorods have higher refractive index, n_3 compared to the polymer, n_2 forming the POF, light at the outlet of the nanorods diverges with wide field of view inside the fiber. Side coupling is obtained for the portion of this diverging light which is at angles larger than the critical angle, θ_c between polymer core and air, n_1. Though, for simplicity and for the remaining of this thesis the term scattering is used to describe the macroscopic effect of light side coupling.

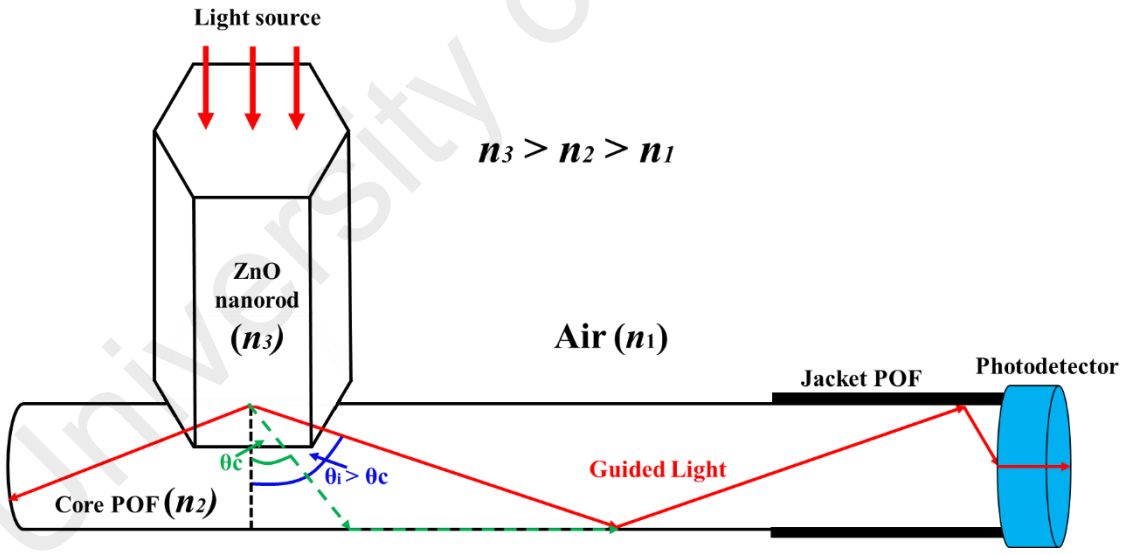

Figure 4.1 Mechanism of light scatters into POF by ZnO nanorods at angle larger than critical angle, θ_c

4.3 Mechanism of Light Scattering For Unpatterned and Spiral Patterned ZnO Nanorod Layers and For the Multi-Channel Optical Fiber

In conventional optical fiber systems, light is typically introduced from one end, guided through the fiber and collected at the other end. This common method has been widely used for sensing applications using plastic optic fiber (POF) coated with ZnO nanostructures (Batumalay et al., 2014; Harith et al., 2015; Lokman et al., 2015). In previous chapter, two approaches were proposed to increase the magnitude of light collection and light side coupling was applied in order to optimize the growth of ZnO nanorods on POF. This section explains the mechanism of light scattering for unpatterned and spiral patterned ZnO nanorod coatings and for the multi-channel optical fiber case as illustrated in Figure 4.2.

Light scattering is induced by the presence of ZnO nanorods on the surface excitation locations along the POF. A portion of the scattered light is guided when scattering angles are greater than the critical angle between the surrounding and the core (Bora et al., 2014). The coupled light propagates through the POF to the terminal detector (I_{out}). The presence of the nanorods as well causes light leakage through the side of the fiber (I_{leak}) (Figure 4.2(a)). For example, if two point light sources, $P(z_1)$ and $P(z_2)$ along a POF are illuminated simultaneously, then the excitation inside the fiber is maximised at these points. However, due to the nanorods inducing light leakage, the intensity of the guided light decreases exponentially to the ZnO nanorods interface. For the location farthest away from the interface (e.g. z_2), any light reaching the detector is minimised. Hence, the power coupled from point z_2 provides only minimal contribution to the total guidance. Clearly, the way to increase the contribution originating from point z_2 is to reduce the amount of leakage.

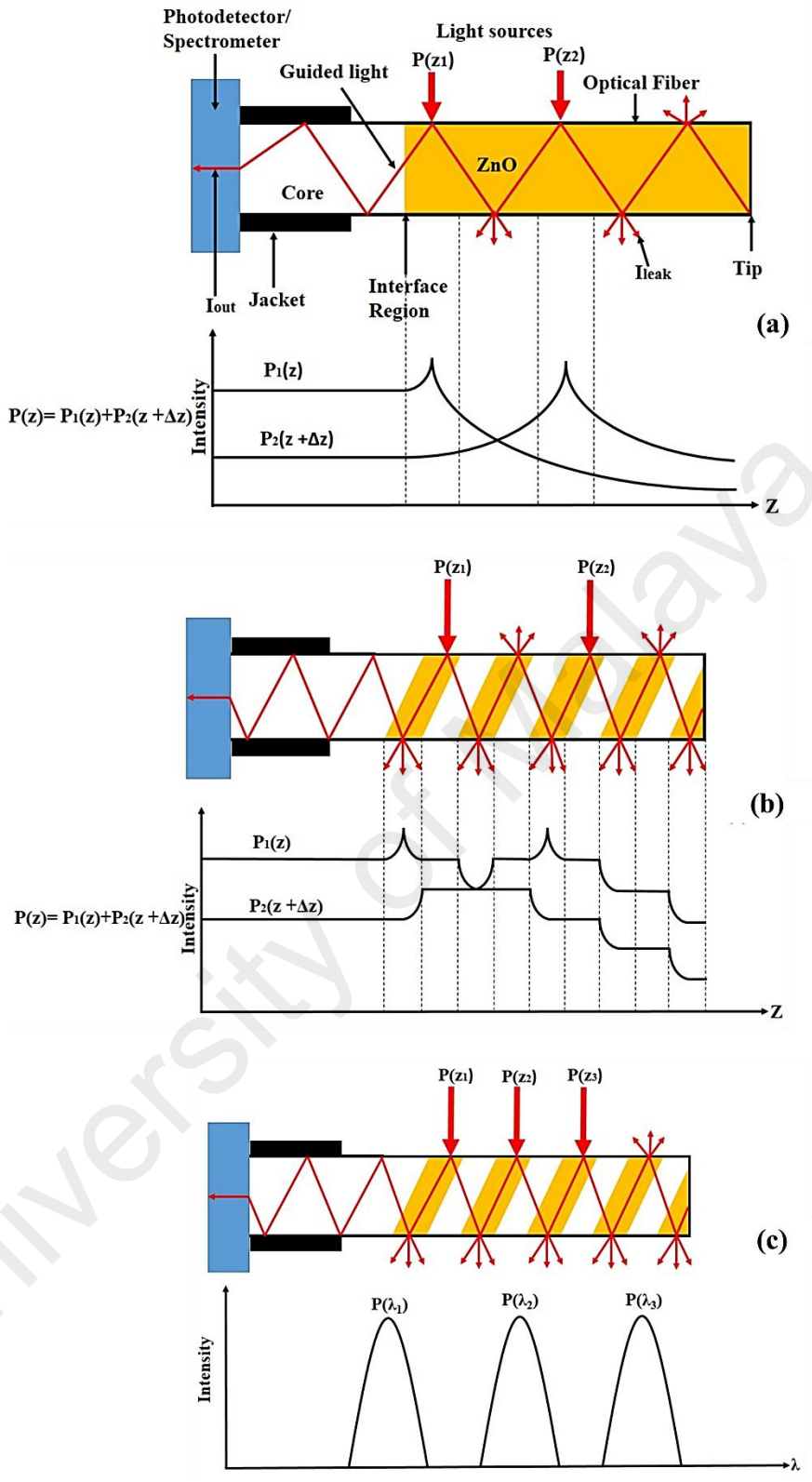

Figure 4.2 Schematic diagram of light scattering for (a) Unpatterned growth of ZnO nanorods with the coupling light (b) Spiral patterned growth of ZnO nanorods with more interface and ZnO regions with the coupling light (c) Spiral patterned growth of ZnO nanorods for a multi-channel excitation

Light leakage can be minimised by reducing the ZnO coverage through the fabrication of a spiral patterned layer of ZnO nanorods as shown in Figure 4.2(b). The reduction of the effective area of the scattering layer is expected to increase the contribution from point z_2. Considering an arbitrary point at the middle of the spiral patterned ZnO layer (Figure 4.2(b)), the light coupled inside the fiber leaks exponentially inside the coated region. The intensity remains steady in the uncoated region till the next ZnO patterned region where the exponential decay occurs again. The intensity from point z_2 is increased due to a balance between the optimised side coupling from the ZnO patches and the reduction of the leakage due to the reduction of the effective ZnO nanorods region. On the basis of this hypothesis, one can predict possible enhancement of the total coupling when an extended light source is used.

In another demonstration, the presence of patches of ZnO nanorods was used for multi-channel excitation. Though, it is possible to achieve multi-wavelength excitation with unpatterned growth, channels further from the ZnO edge suffers a sever loss. Higher power is then required for channel equalisation. This effect is minimised here using the spiral patterned POF as shown in Figure 4.2(c). Different wavelengths of light source, $P(z_1)$, $P(z_2)$, and $P(z_3)$ are individually excited at different spiral patches of ZnO nanorods. Due to the reduction of the effective scattering area, the peaks of the coupled light are expected to be higher than multi-channel performed on unpatterned ZnO nanorods growth. This gives rise to a possible application in wavelength division multiplexing. The coupling efficiency of each channel depends on the spacing between the scattering domains.

4.4 Experimental Characterization of Multi-Channel Optical Fiber towards Light Side Coupling

Spectral analysis was performed for the unpatterned and patterned samples to identify the wavelength coupling maxima using the setup shown in Figure 4.3. A broad spectrum white light source and two infrared laser sources were used (850 and 980 nm). The one end of the POF fiber is linked to a spectrometer and subsequently to a computer for data recording and analysis. The other one end of the POF fiber was covered with a small aperture to avoid light entering from the end during spectral acquisition. The optical transmittance of patterned and unpatterned POFs were compared. Transmittance was calculated by the following expression.

$$Transmittance = \frac{Coupled\ Power}{Source\ Power} \tag{4.1}$$

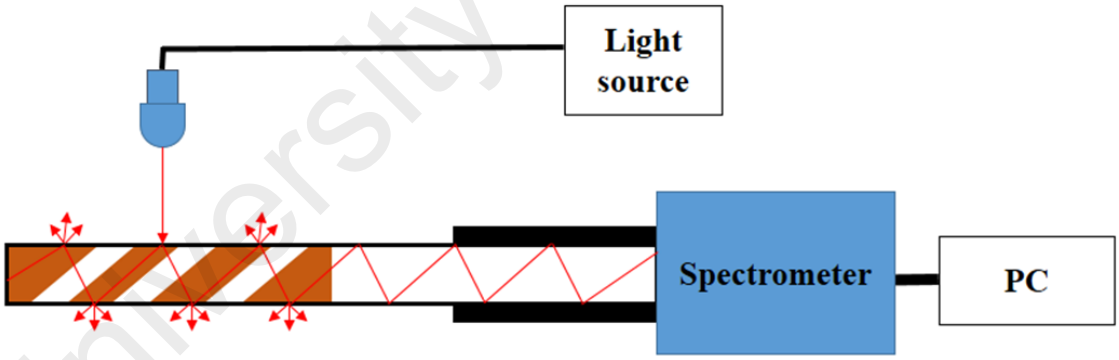

Figure 4.3 Spectral analysis setup to determine wavelength coupling maxima

Figure 4.4 represents the transmittance of visible white light for spiral patterned and unpatterned POFs when an extended source was used. The result indicates that the spiral patterned growth is able to increase coupling of the light source better than the unpatterned growth due to the existence of more interfacial ZnO regions and reduction of

active region on the POF. The plot in Figure 4.4 also shows that the spiral patterned growth provides a higher light transmittance with an improvement factor of 2.2.

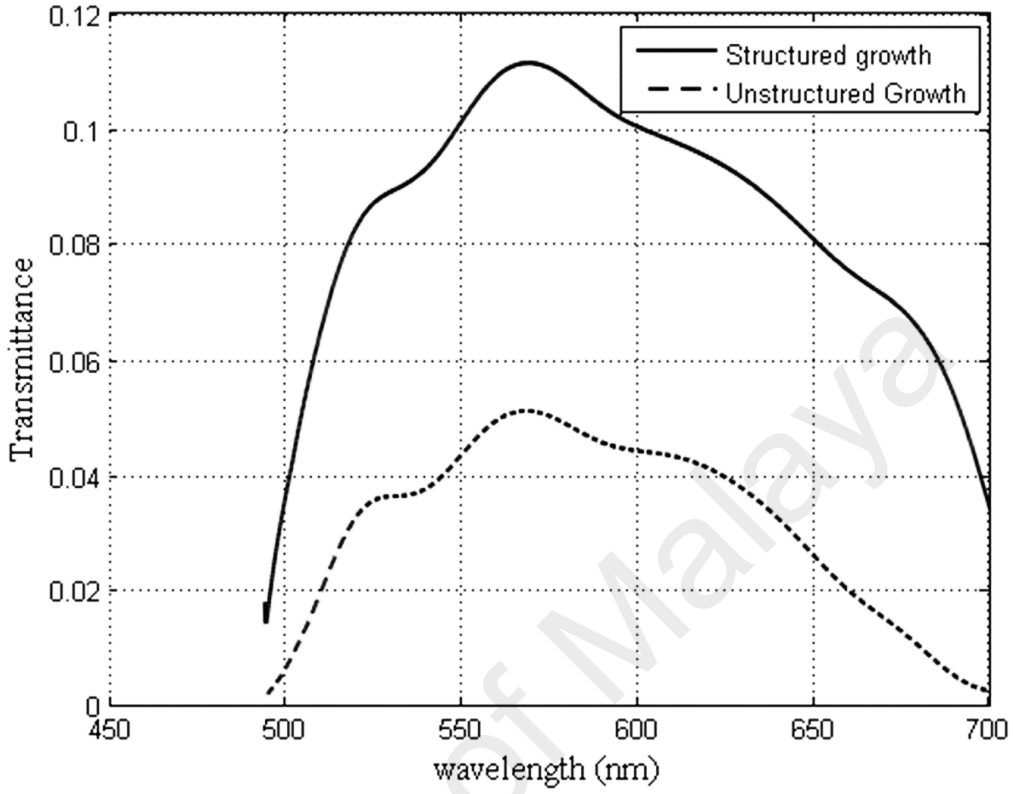

Figure 4.4 Transmittance of the visible white light spectrum

Figure 4.5 shows that the transmittance of light for the spiral patterned growth is higher than the unpatterned growth when both infrared laser sources were tested. However, the infrared laser source did not significantly couple at the particular wavelength inside the POF due to the small waist of laser beam that only focuses on a specific region. Consequently, less amount of light scatters into POF by ZnO nanorods is coupled and guided inside the POF. Therefore, the coupling efficiency was too low for useful applications.

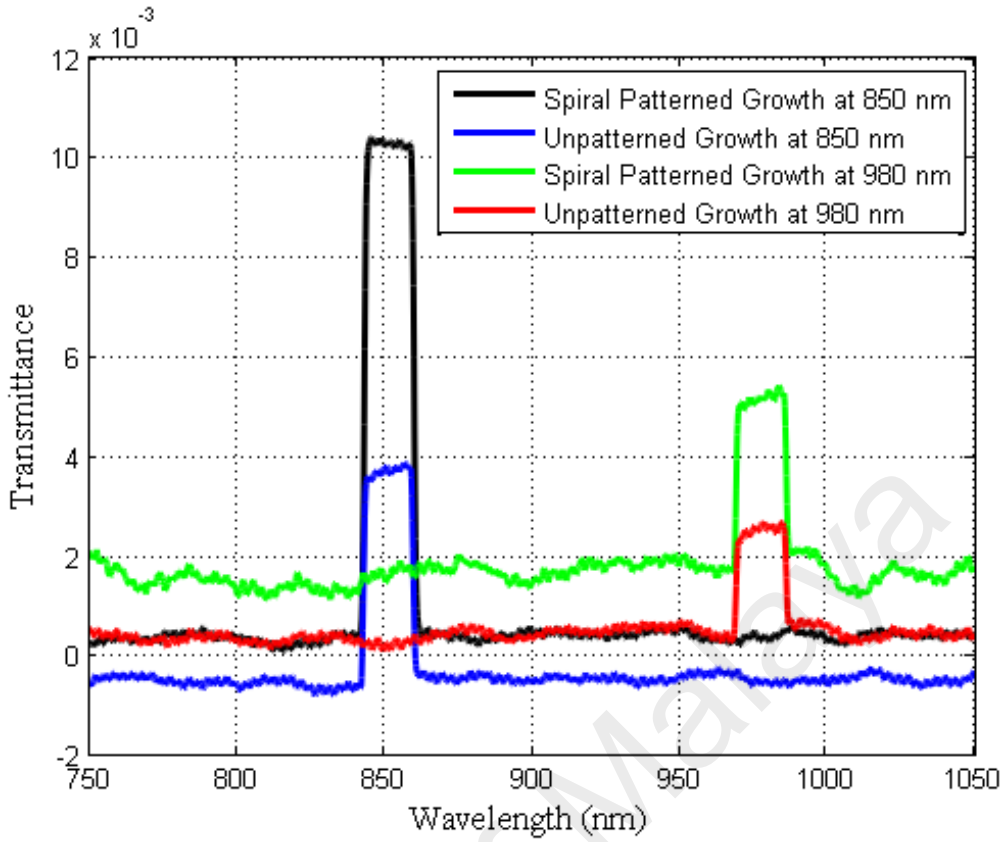

Figure 4.5 Spectrum for near infrared (850 and 980 nm) for spiral patterned and unpatterned growth

4.5 Modeling of Coupling Efficiency for Spiral Patterned and Unpatterned Coating by Varying the Width of the Coated Region towards Light Side Coupling

In this section, a first order model is derived to simulate the impact of millimeter (mm) scale spiral patterns on power leakage due to scattering by ZnO nanorods. In the side coupling mechanism proposed here, ZnO nanorods allow light to couple inside the guiding region (core of POF). ZnO nanorods as well guide the light outside the fiber core with each bounce at the interface. These two counter-effects restrict the coupling to an effective area around a region at the beginning of the ZnO coating. This limits the use of this system in multiple channels as well as for application with extended sources. One way to improve the system response is through spreading the effective coupling area of

ZnO nanorods across the fiber. This is achieved by introducing patches of nanorods coating. Optimizing the gaps and width of ZnO coating enhance the system response depending on the light source used. More detailed analysis of the scheme was explained in section 4.3. Two kinds of ZnO nanorod coating schemes on POF were analyzed: 1. Spirally patterned ZnO nanorod coatings in which a light-blocking layer was applied, and 2. Unpatterned coatings in which ZnO nanorods coated the entire surface of the POF uniformly. The two configurations are shown in Figure 4.6.

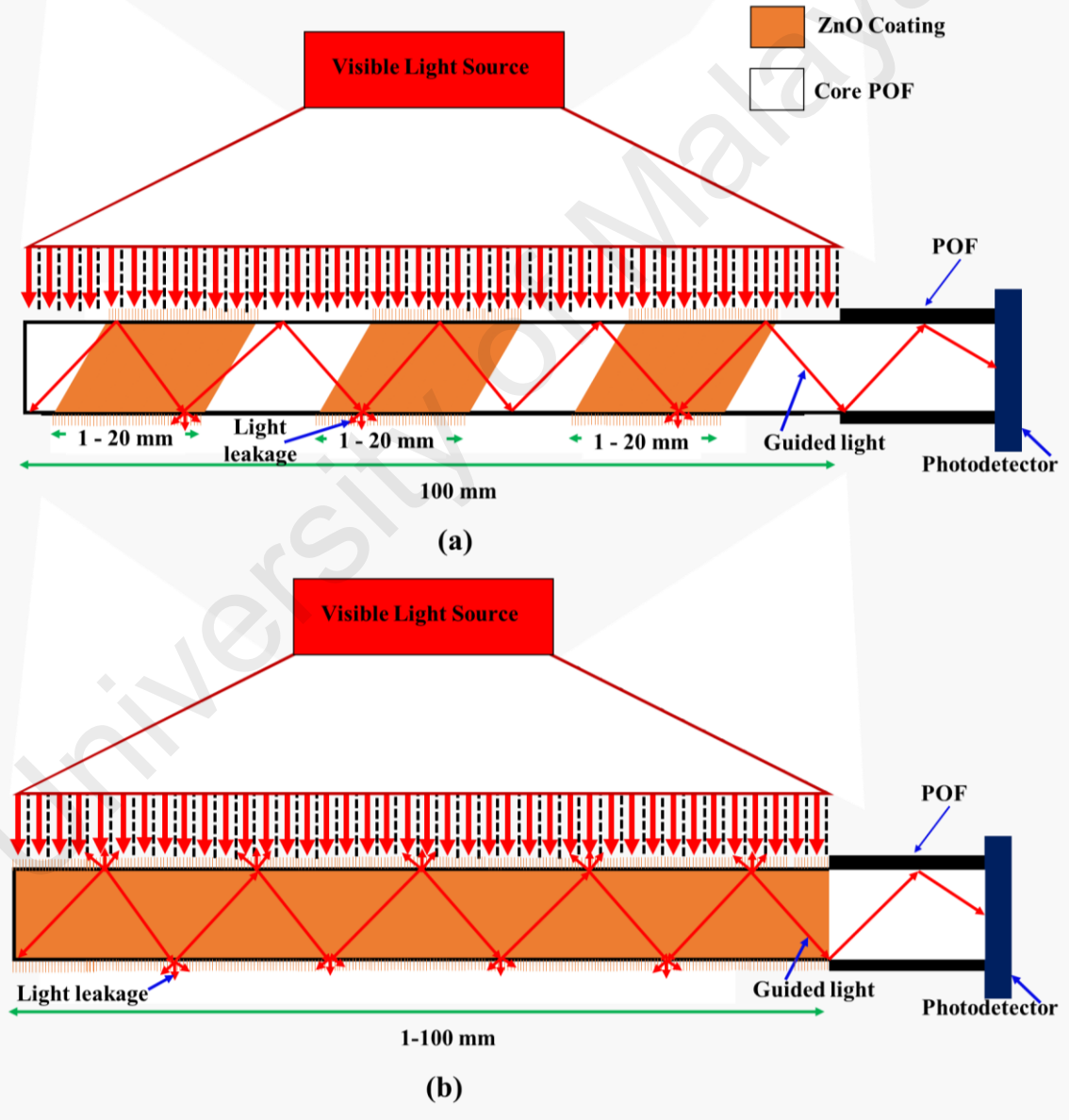

Figure 4.6 (a) Spirally patterned coating of ZnO nanorods on POF and (b) unpatterned coating of ZnO nanorods on POF with a visible light source

In the schemes illustrated in Figure 4.6, the visible-light source illuminates the upper hemisphere of the coated POF when oriented normal to its surface. The ZnO nanorods scatter light at different directions accordingly and the total light scattered inside the optical fiber is expresses in the following equation

$$P_o = P_{source} \cdot \rho_a \cdot C_{sc} \tag{4.2}$$

In Equation (4.2), P_{source}, is the power of the source excitation. The constants C_{sc} and ρ_a are the scattering cross section of one rod (m) and rods density (number of nanorods per unit area, $N_{rod}/\ \mu m^2$) respectively. However, not all light scattering is guided (coupled). Only light scattered with angles larger than the critical angle contributes the coupling. The Equation (4.2) can be written as

$$P_o = P_{source} \cdot \rho_a \cdot C_{sc} \cdot \psi \tag{4.3}$$

The constant ψ is the portion of the scattered light that couples into the guided modes of the fiber. In order to derive an expression of ψ, a probability of distribution function of the light scattering from one ZnO rod versus radial, θ and azimuthal, ϕ angles was calculated and this is typically referred to as the phase function $p(\theta, \phi)$ and it is illustrated in Figure 4.7.

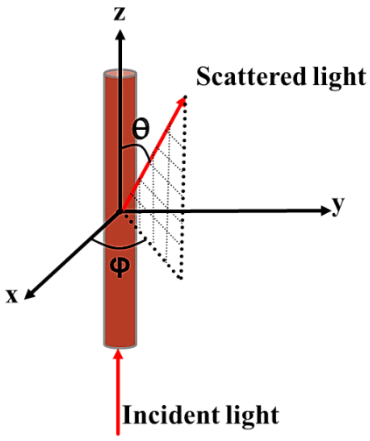

Figure 4.7 Definition of polar coordinate

As $p(\theta, \phi)$ is a probability distribution function, the integration over all angles should be unity.

$$\psi = \int_0^{2\pi} \int_0^{\pi} p(\theta, \phi) \sin\theta \, d\theta d\phi = 1 \quad (4.4)$$

In Equations (4.4), the function p (θ, ϕ) is the phase function which is assumed to be independent on the azimuthal angle, ϕ and hence the integration over ϕ is 2π. Hence in Equation (4.4), the integration is over the radial angle, θ only. The expression in Equation (4.4) is reduced to

$$\psi = 2\pi \int_0^{\pi} p(\theta, \phi) \sin\theta \, d\theta = 1 \quad (4.5)$$

Only light scattered at angles large than critical angles contributes to the guidance inside fiber. The fraction of scattered light that is guided can be written as:

$$\psi = 2\pi \int_{\theta c}^{\pi} p(\theta - \theta_{inc}) \sin\theta \, d\theta \quad (4.6)$$

The function p (θ - θ_{inc}) is assumed to vary linearly with the incident angle, θ_{inc}. This assumption can be justified here as small range of angles around normal incidence is considered. At larger angles this model deviates from the actual system. The critical angle, θ_c, is the one between the core POF and air. From Equation (4.3) and (4.6), the maximum coupled power, P_o to core or cladding mode is defined as

$$P_o = P_{source} \, 2\pi C_{sc} \rho_a \psi \quad (4.7)$$

To study the coupling and source distribution effect, the POF surface was divided into segments of width, Δz shown in Figure 4.8(a). The source excitation is assumed constant over the width. At any segment h on the surface of the POF, exposed to a visible light source, there is an arbitrary intensity profile $P_s(z)$ causes a portion of $\psi\eta P_s(z)$ to couple to the guided modes. In addition to the excitation, a portion of the previously coupled light (coming from segment P_{h-1}) adds to the amount of light coming out of segment h as shown in Figure 4.8(b). Notice that, in the figure the coupling coefficient from segment h is indicated as η_z. The power coupled out of segment h can be then written as

$$P_h = \psi\eta_{z,h}P_s + P_{h-1} - \left(\eta_{z,h}P_{h-1}\right) \tag{4.8}$$

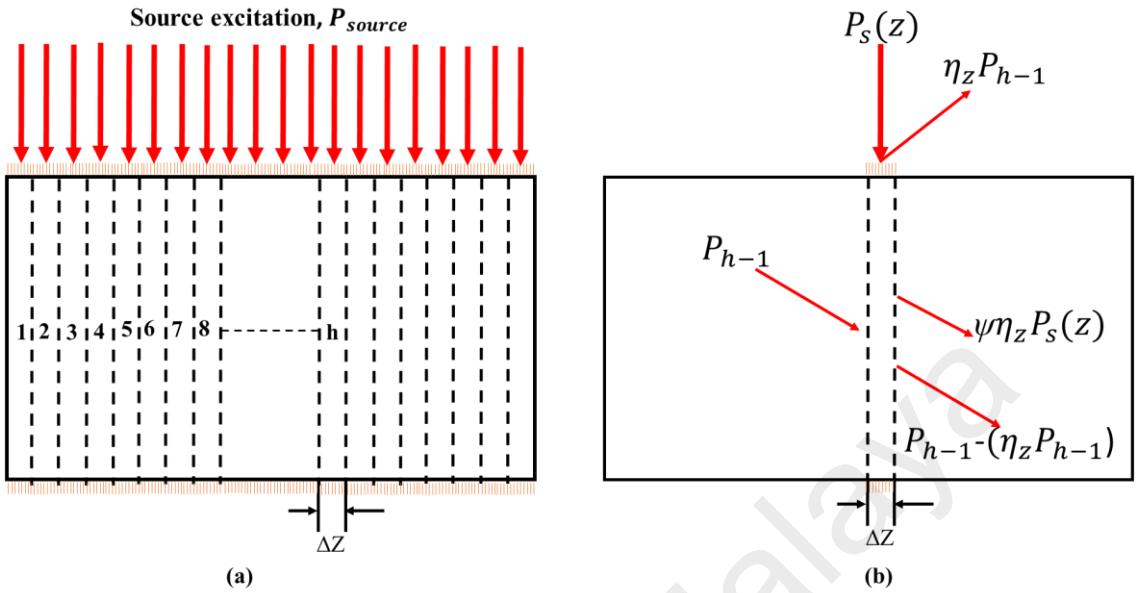

Figure 4.8 (a) Dividing the POF coated with ZnO nanorods into discrete sections of width *Δz* for both coating schemes (b) Optical Intensity components around a segment h of the ZnO coated POF

In simulations, the length of POF was selected to 100 segments of 1 mm each for a total of 100 mm and P_{source} is the power of the source excitation that was fixed to 5 for amplitude. Then, normalization of the outputs were applied, each value of the outputs divided by P_{source} to have a maximum value equal to 1. Three coating regions of ZnO nanorods were developed in order to create spiral patterned coating on the POF and the widths of the ZnO nanorods coating were varied from 1 to 20 segments as shown in Figure 4.6(a). Meanwhile, the unpatterned POF was evaluated by varying the ZnO nanorods coating from 1 to 100 segments which is fully coated as depicted in Figure 4.6(b). These two scheme coatings were analysed using Equation (4.8) by applying finite difference method. In this case, the widths of ZnO nanorods coating were fixed to 3 segments (3 mm) starting from segment 10 to 12 (1st ZnO region), 13 to 38 (uncoated region), 34 to 36 (2nd ZnO region), 37 to 62 (uncoated region) and 63-65 (3rd ZnO region). For ZnO

unpatterned coating, there is only one ZnO region that is also fixed to 3 segments (10 – 12). The region omit is a coated with ZnO nanorods has the coupling coefficient, η_z higher than zero and η_z for uncoated region is equal to zero. Thus, the power for the segment before segment 10 (P_9) was equal to zero due to the η_z was zero. As the portion of light from segment 9, P_9 was substituted into Equation (4.8) to couple to the amount of light of P_{10}. The total light at segment 10 is

$$P_{10} = \psi\eta_{z10}P_s + P_9 - (\eta_{z10}P_9) = \psi\eta_{z10}P_s$$

The amplitude of $P_{10} = \psi\eta_{z10}P_s$ is coupled to the amount of light in segment 11. Thus, P_{11} can be written as follow:

$$P_{11} = \psi\eta_{z11}P_s + P_{10} - (\eta_{z2}P_{10})$$

Then, the coupling light in segment 11 is coupled to the light presents inside segment 12, the amplitude of P_{12} is given as

$$P_{12} = \psi\eta_{z12}P_s + P_{11} - (\eta_{z12}P_{11})$$

In this case, the coupled light from segment 10 to segment 12 is equal to $P_{12} = \sim 0.7$ because the width of ZnO nanorods coating was fixed to 3 segments. For the unpatterned POF, the coupling light is consistently equal to P_{12} in uncoated region until reaching the photodector. The consistency of the coupled light occurs due to coupling coefficients from segment 13 to 100, η_{z13} to η_{z100} are equal to zero in uncoated region. Thus, the coupling light reached the photodetector can be written as

$$P_{13} = \psi\eta_{z13\ to\ 100}P_s + P_{12} - (\eta_{z13\ to\ 100}P_{12}) = P_{12}$$

In spiral patterned POF, this consistency of P_{12} remains steady in the uncoated region (segment 13 to 38) till the second ZnO nanorods region (segment 34 to 36) that has another three segments. The amount of P_{12} is coupled again in the first segment of second ZnO nanorods region. The coupled light keeps increasing until the next uncoated region. The effect of spiral patterned coating on POF leads to a significant improvement of light intensity as depicted in Figure 4.9 achieving a level of coupling light of 0.98. In the case, side coupling was obtained to be a factor of 1.4 times better for spiral patterned coating as opposed to unpatterned continuous coatings.

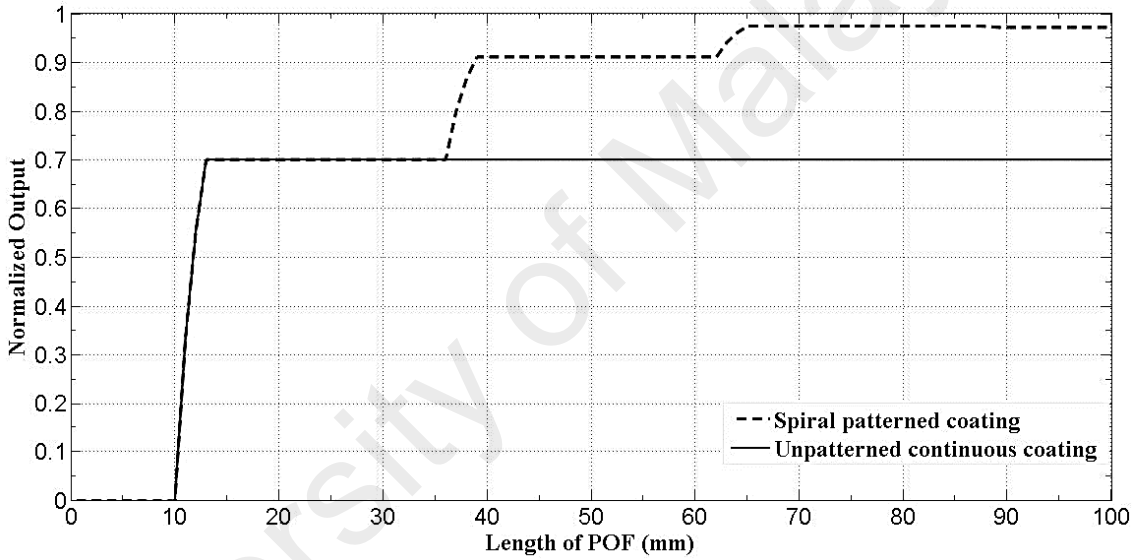

Figure 4.9 The scheme of light propagation for unpatterned continuous and spiral patterned coating where ZnO coating region was fixed to 3 segments (3 mm)

It is worth mentioning that the coupled power is normalized to the optical power incident at each segment. Also in off-axis coupling azimuthal modes (or skew rays) are dominantly coupled (Dwivedi, Sharma, & Gupta, 2007). These however might not be the only modes to be excited in side coupling as radial modes can be excited as well. This is due to the main fact that mode excitation happens due to matching the the momentum of the scattered light to the propagation constant of guided mode. In general, the assumption of specific power distribution among any set of modes (in any form) with the proposed first

order model especially when large core fiber is used would not have a significant effect on the driven results or the measurement as we estimate the leak due to surface scattering.

4.6 Theoretical Optimization of Spiral Patterned Width for Optimal Side Coupling

Improved optical side coupling efficiency was demonstrated for spiral patterned zinc oxide (ZnO) nanorods coated large core plastic optic fibers (POFs) as opposed to unpatterned continuous coatings (Rahim et al., 2016). Nanorods enhanced coupling inside the fiber by scattering light but were also capable of causing leakage. Structuring the growth to specific regions allowed scattering from different segments along the fiber to contribute to the total coupled power. In order to optimize the width of ZnO nanorods coating on POF, an analysis was theoretically performed by analyzing the coupling efficiency in three different considerations. First, as explained in section 4.5, the analysis was continued by varying the width of spiral patterned coating from 1 to 20 mm segments as shown in Figure 4.6(a). Meanwhile, the unpatterned was analyzed by varying the ZnO nanorods coating from 1 to 20 segments which is fully coated as illustrated in Figure 4.6(b). A broad spectrum light source was applied for side coupling in the analysis. Figure 4.10 illustrates the modeling results of normalized coupling output for unpatterned and spiral patterned POF. The normalized coupling output increased greatly for spiral patterned over that derived from unpatterned coatings as the width of ZnO nanorods coating was varied from 0 to 20 mm.

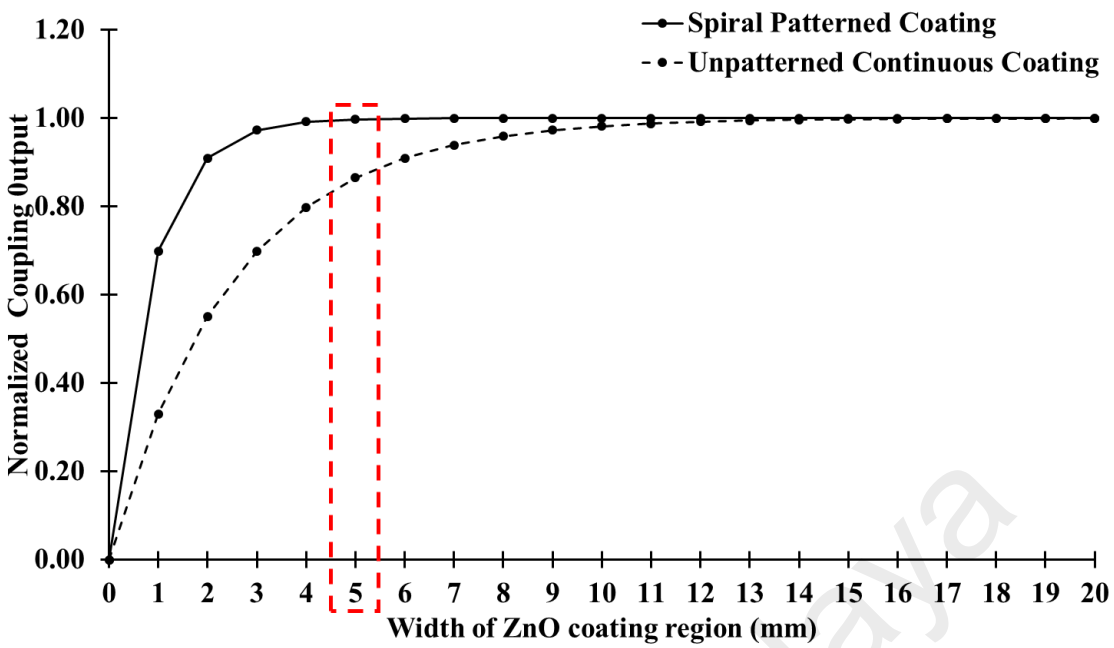

Figure 4.10 The normalized coupling output for unpatterned and spiral patterned coating by varying the width of ZnO nanorod coating on POFs

Spiral patterned POFs coupled more light compared to unpatterned POF for nanorod coating widths less than 5 mm as shown in Table 4.1. The greatest difference in coupling output between patterned and unpatterned coatings was shown at ZnO width equal to 1 mm where $\Delta I_{(1\ mm)} = I_p - I_{up} = 0.369$ due to spiral ZnO coating along the core POF compared to unpatterned coating that had only one patch of ZnO region (1 mm) on the POF. Although $\Delta I_{(1mm)}$ was the highest, the coupling output for spiral pattern was not considered because it was not the maximum value of light side coupling. The spiral pattern coating achieved the maximum value of light side coupling at width equal to 5 mm ($\Delta I_{(5mm)} = I_p - I_{up} = 0.135$). Therefore, despite that $\Delta I_{(5\ mm)}$ was less than $\Delta I_{(1\ mm)}$, the use of maximal light side coupling was more dominant in applications. Meanwhile, the unpatterned coating achieved the maximum value of light side coupling at ZnO coating width longer than spiral patterns. Once the maximum coupling output was reached, the coupling output remained consistent in POF's with both types of coatings at the normalized value equal to 1 even though the width of ZnO coating was varied.

Table 4.1 Differences of normalized coupling output, ΔI between spiral patterned and unpatterned POFs for different widths of ZnO coating from 0 to 7 mm

Widths of ZnO coating region (mm)	Normalized coupling output		
	Spiral pattern, I_p	Unpatterned, I_{up}	$\Delta I = I_p - I_{up}$
0	0	0	0
1	0.699	0.330	0.369
2	0.910	0.551	0.359
3	0.973	0.699	0.274
4	0.992	0.798	0.194
5	**1.000**	**0.865**	**0.135**
6	1.000	0.909	0.091
7	1.000	0.939	0.061

Second, with the coating schemes used in (i), a laser light source (Gaussian beam) was applied and the effects on the coupling efficiency was analyzed for spiral patterned and unpatterned coatings. The source power, P_s in Equation (4.8) was set as follows:

$$P_s = \frac{1}{\sigma\sqrt{2\pi}} \exp\left(-\frac{r^2}{2\sigma^2}\right) \tag{4.9}$$

Where,

σ = Beam waist

r = Distance from the center of the beam

In the modeling, the center of the beam was aligned to be at a border between the exposed POF and jacket as illustrated in Figure 4.11. The same procedures was applied for the modeling with a broad spectrum light source was used in order to observe the coupling efficiency with laser light source. ZnO nanorods coating on POF allows normal incident light to scatter inside the POF at angle greater than the critical angle.

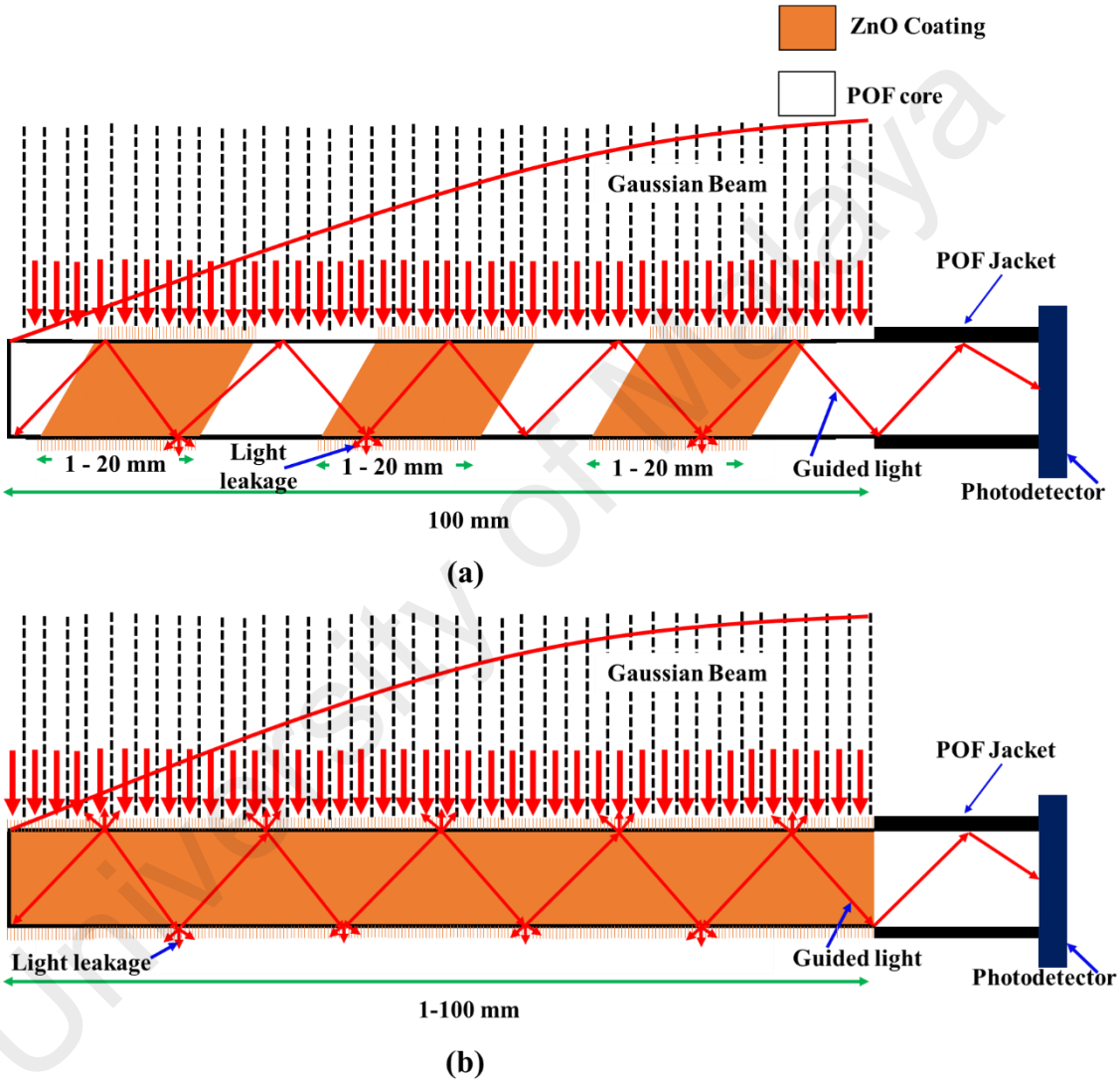

Figure 4.11 (a) Spirally patterned coating of ZnO nanorods on POF and (b) unpatterned coating of ZnO nanorods on POF with a laser light source (Gaussian beam)

Figure 4.12 shows the theoretical coupling efficiencies of spiral patterned and unpatterned coatings. The same response as discussed in previous work (H Fallah et al., 2013) occurred in the analysis which the total power inside the fiber reduced exponentially for the both scheme coatings, due to scattering effects (neglecting visible light absorption by the ZnO nanorods, which is minimal as ZnO is a wide band gap semiconductor). As the width was increased, there was more light leakage through the presence of ZnO coating on POF. However, spiral patterned POF coupled more light compared to unpatterrned POF for all width of ZnO coating region. The peaks of coupling efficiencies for spiral patterned and unpatterned coating were shown at ZnO width equal to 2 mm.

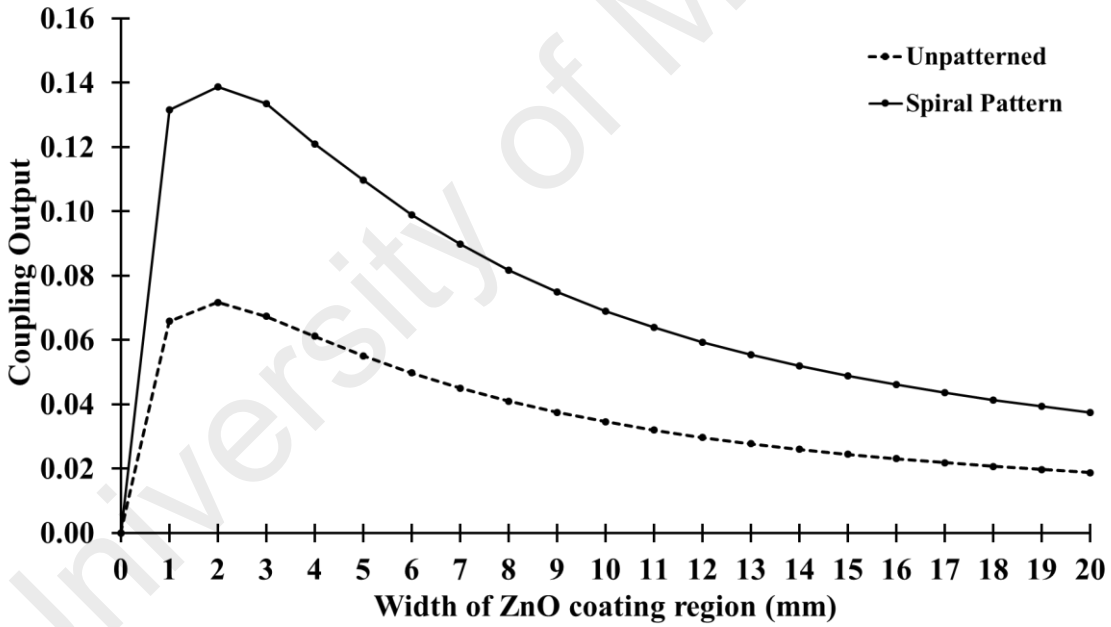

Figure 4.12 The coupling efficiencies for spiral patterned and unpatterned coating excited by a laser light source

Third, the effects on the coupling efficiencies for spiral patterned and unpatterned coatings were evaluated by varying the spacing (uncoated region). Three widths of spiral patterned coating on the POF were fixed at 5 segments and the spacing were varried from 1 to 20 segments and as shown in Figure 4.13(a). Meanwhile, the unpatterned POF was

also analyzed by varying the uncoated region from 1 to 20 segments and a continuous ZnO nanorods coating was created on POF with a width of 5 segments as depicted in Figure 4.13(b). A broad spectrum light source was applied for side coupling in the analysis due to high coupling efficiency as discussed in the first theoretical optimization.

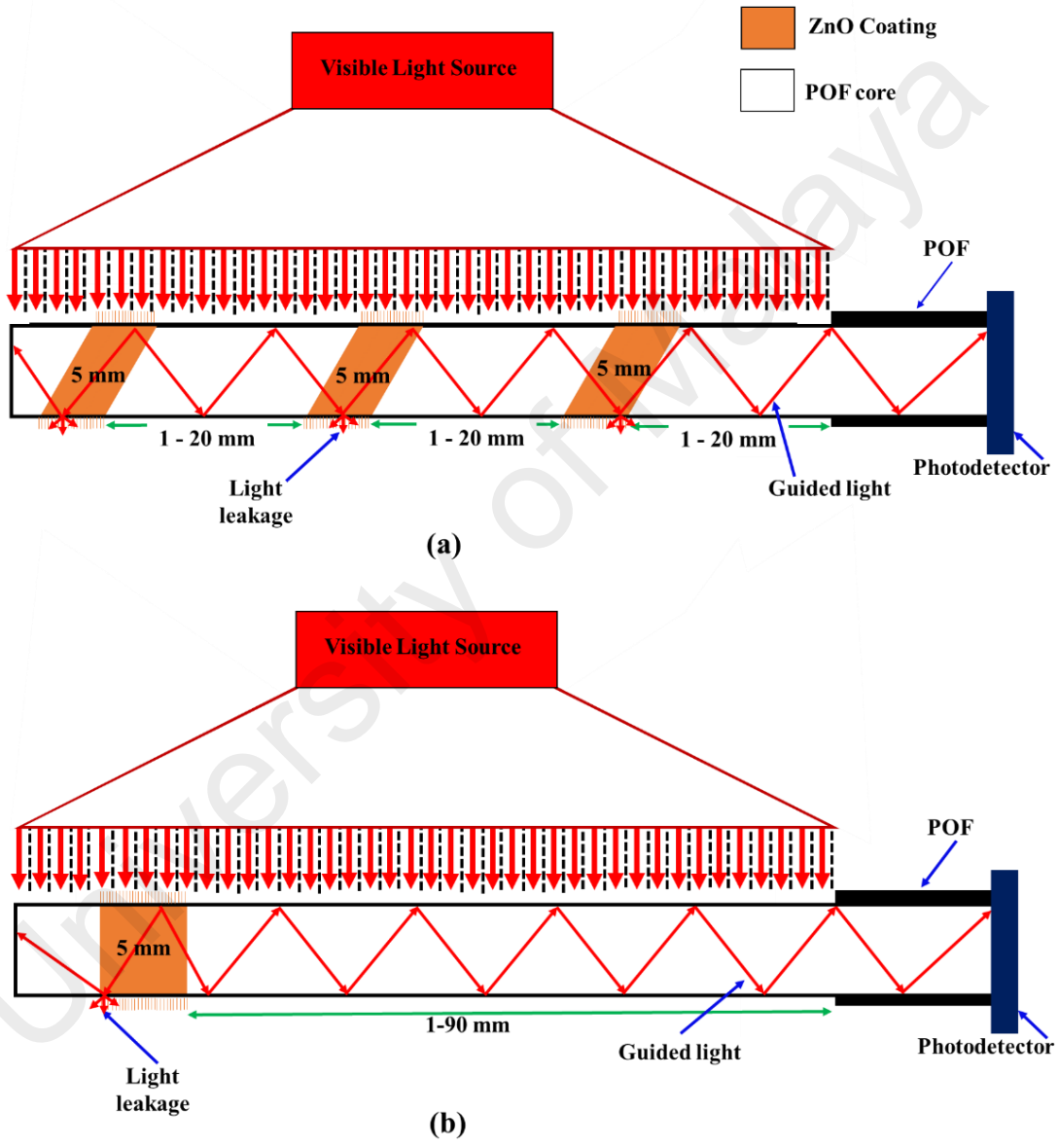

Figure 4.13 Spiral patterned coating of ZnO nanorods (b) unpatterned coating of ZnO nanorods with varied uncoated spacing

The modeling result in Figure 4.14 clearly shows there is no light scattering into POF when the width of uncoated region was varied. The light only coupled within the ZnO coating region and remained steady in uncoated region due to the coupling coefficient, η_z for uncoated region is equal to zero as explained in section 4.5. Although the width of uncoated region was varied, the output remained unchanged for the both coating schemes. The coupling output for spiral patterned coating is higher than unpatterned coating due to more interfacial ZnO coating regions on POF to couple the light.

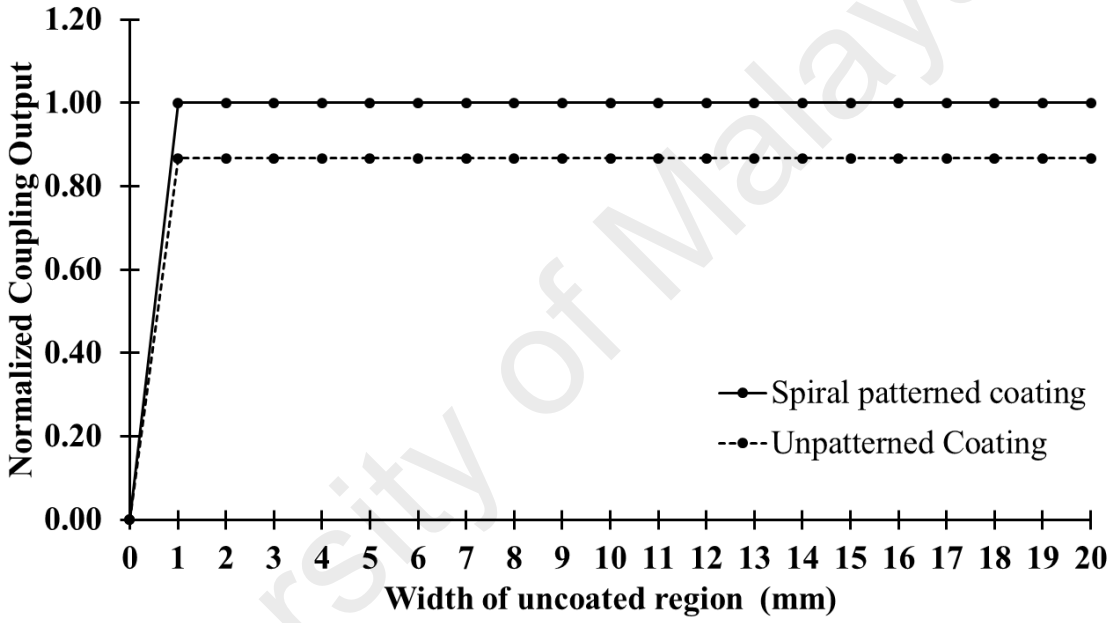

Figure 4.14 The effects on coupling efficiency by varying the uncoated region

4.7 Experimental Optimization of Spiral Patterned Width for Optimal Side Coupling

POF fiber spiral patterning and ZnO nanorod seeding and synthesis procedures were described in detail in the previous chapter. Standard polymethyl methacrylate (SK-80 POF fibers from Mitsubishi Rayon Co., LTD; Japan) were utilized in the experiments to serve as controls and the same fibers were modified to obtain spiral patterned POF with a specified spiral pitch angle, spacing and width. The jacket of the POF were

mechanically stripped to expose the core fiber over a length of 10 cm. The fiber length of 10 cm was chosen in this work in order to have a full illumination of light beam on the stripped fiber from a light source with diameter of 3 cm that was placed in parallel at an optimal distance of 3 cm from the POF surface. Figure 4.15 illustrates the ZnO coating schemes; three widths were varied from 3, 5 to 7 mm for the spiral patterned and unpatterened POF. These width coatings were selected from modelling result in Table 4.1 due to the significant output differences occurred at small width of ZnO coatings. A fully coated POF (100 mm) was also fabricated to complete the validation. Tape-patterned and unpatterned POFs were then placed in a ZnO seed solution and subsequently into the growth solution to form ZnO nanorods. Percent surface coverage and nanorod orientation were evaluated as described in the previous chapter by evaluation of scanning electron micrographs recorded by a Hitachi, 3400N SEM system operating at 20 kV.

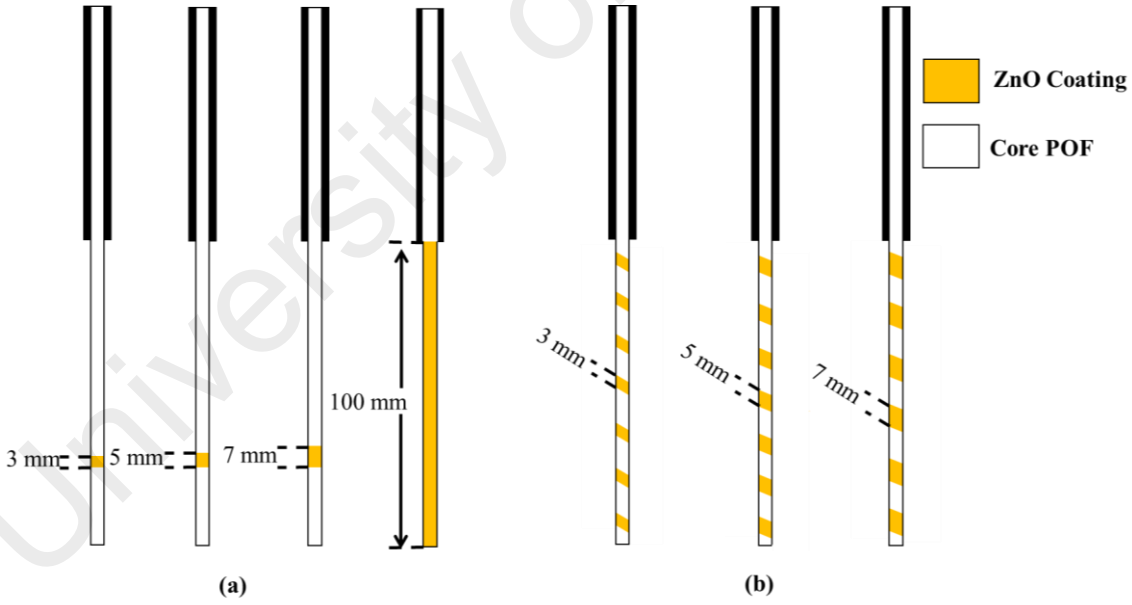

Figure 4.15 Coating schemes (a) unpatterned POFs (b) Spiral patterned POFs

Optimization of optical input through the POF waveguides was realized by correlation with maximal values of the output voltage as depicted in Figure 4.16. A function generator was used to modulate the light from a broadband LED light source

(diameter = 3 cm). Sinusoidal intensity pattern was generated and transmitted through the LED. At the receiver side, peak-to-peak voltage of photodetector output was recorded (not the DC value). This scheme allows minimization of the ambient light effect and external sources. The amplitude of output voltage changes according to the amount of coupling inside the POF. The light source was placed in parallel and ~3 cm from the POF surface. The diameter of the light source was oriented along the longitudinal axis of the POF. The fiber tip was covered to avoid light entering from the end. The analysis was performed on the spiral patterned POFs with three different widths of ZnO coatings (3 mm, 5 mm and 7 mm), the unpatterned POFs with the limited ZnO coating (3 mm, 5 mm, 7 mm) and full coated POF's. Five readings were acquired for each measurement.

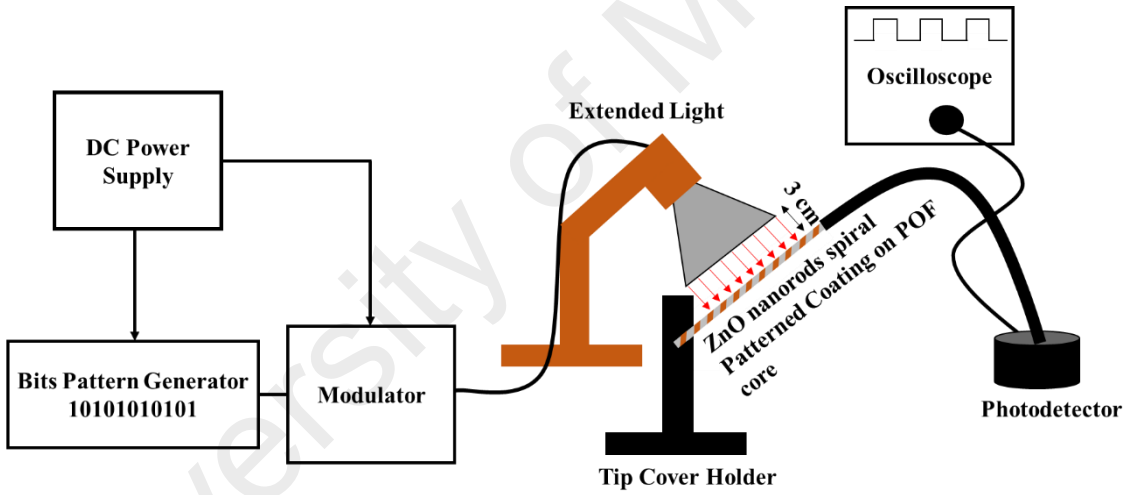

Figure 4.16 Optimization setup to measure the output voltage for unpatterned and spiral patterned ZnO nanorods

Based on the simulation results, 3 mm, 5 mm, and 7 mm coating widths were selected for experimental optimization and application. Figure 4.17 shows the experimental results for spiral patterned and unpatterned POFs. Overall, it can be seen that both coating schemes correlated well with simulations. The results clearly showed that the unpatterned coatings of ZnO nanorods (3 mm, 5 mm and 7 mm) coupled less light compared to spiral patterned POFs. In addition, the full ZnO coated POFs (100 mm)

produced an output voltage that was less than spiral patterned POFs (3 mm, 5 mm or 7 mm) due to less illumination coverage of the visible light source in distance of 3 cm from POF sample as shown in Figure 4.16.

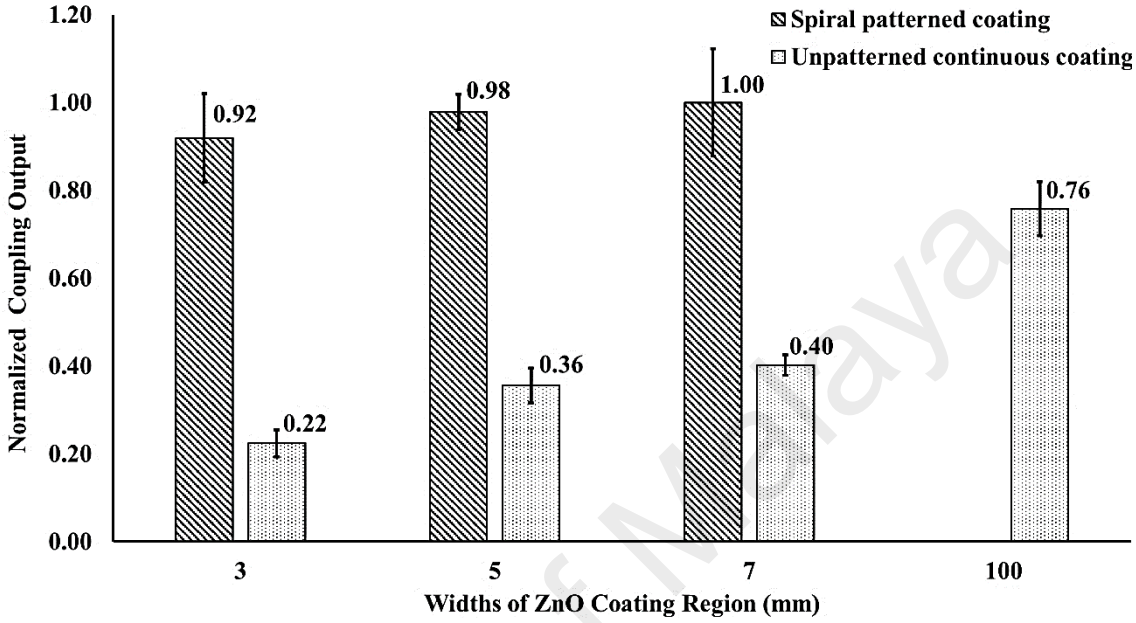

Figure 4.17 The experimental result of spiral patterned and unpatterned coating for 3, 5, 7 and 100 mm

4.8 Summary

The spiral pattern on the POF also provides a higher light intensity multi-channel compared with unpatterned ZnO nanorods POF. Spectral analysis was performed to investigate light transmittance for different wavelength of light sources. It was found that visible white light source significantly coupled the light into the POF compared with infrared laser sources.

The present study also theoretically optimized the width of the ZnO nanorod spiral coating with a visible light source. The effects on light side coupling were analyzed by varying the width of ZnO coating region. A significant improvement was demonstrated by spiral patterned coating at small widths of spiral coating region.

The light side coupling also was theoretically proved with laser light source (Gaussian beam) for spiral patterned and unpatterned coating. It is found that the light exponentially decays when the width of the ZnO coating region was increased due to the distribution of Gaussian beam. Consequently, the both scheme coatings contributed less coupling efficiencies for applications.

The analysis on light side coupling were then performed by varying the uncoated region for the both scheme coatings. There was no any change in amplitude of light when the width of uncoated region was varied. Thus, the width of uncoated region can be ignored in design for optimal efficiency.

Overall, spirally patterned coating theoretically proved an improvement in light guiding compared to unpatterned coating. An optimized width of spiral patterned coating was found to be 5 mm for efficient light coupling. There was reasonable correlation between theory and experiment.

CHAPTER 5: APPLIED LIGHT SIDE COUPLING WITH OPTIMIZED SPIRAL PATTERNED ZINC OXIDE NANOROD COATINGS FOR TEMPERATURE AND MULTIPLE OPTICAL CHANNEL ALCOHOL VAPOR SENSING

5.1 Introduction

Optical sensors, another important application of optical fiber, have also experienced fast development and attracted wide attention in fundamental scientific research as well as in practical applications. Optical fiber can not only transport information acquired by sensors at a high speed and in large volume, but it can also play the role of a sensing element itself. In addition, compared with electric and other types of sensors, optical fiber sensor technology has unique merits, such as immunity from electromagnetic interference (B. Lee, 2003), being waterproof (Saito, Ichikawa, & Oshima, 1987), and resistance to chemical corrosion (Giallorenzi, Bucaro, Dandridge, & Cole, 1986). It has advantages over conventional bulky optical sensors, such as the combination of sensing and signal transmission, smaller size (Cullum & Vo-Dinh, 2000), and the possibility of building distributed systems (Mendez, Morse, & Mendez, 1990). Optical fiber sensor technology has been used in various areas of industry, transportation (Oehme & Wolfbeis, 1997), communication (Hill, Fujii, Johnson, & Kawasaki, 1978), security (Szustakowski, Ciurapinski, Palka, & Zyczkowski, 2001), and defence (Cooper, Elster, Jones, & Kelly, 2001), as well as in people's daily life (Hocker, 1979). Its importance has been growing with the advancement of the technology and the expansion of the scope of its application.

However, these optical fiber sensors are usually associated with high cost, high operational power requirements and complexity in operation. Laser light sources are generally used in optical sensing applications but costs related to the laser and mechanical

alignment apparatus can be relatively high (Aneesh & Khijwania, 2011). Application of laser light sources onto coated fibers also poses several problems. Inequality of beam distribution onto the fiber and small beam diameter can lead to fluctuations, non-representation and low intensity (Dickey et al., 2000). Broadband visible light source methods are simpler and less expensive to operate but suffer from low sensitivity. However, specially coated optical fibers are able to improve the sensitivity of visible light source methods. A new broadband visible light source sensor system that utilizes light side coupling to ZnO nanorod coated POF is proposed. The ZnO rods act as scattering elements that induce light transmission into the POF.

Here, in experiments using light side coupling method, molecules of ZnO on POF which is composed of discrete electric charges illuminated by an electromagnetics wave (visible light), electric charges in the ZnO coating layer are set into oscillatory motion by the electric field of the incident light. Accelerated electric charges scatter light into POF. In addition, the excited ZnO nanorods may transform part of incident light into other form called absorption. This phenomena is called extinction that was applied to the spiral patterned coating of ZnO nanorods on POF as a temperature sensor and multiple optical channel waveguide sensor for detection of alcohols in the visible wavelength domain were demonstrated based on a need to develop a low-cost, high sensitivity and uncomplicated sensor system.

5.2 SEM images of Optimized Spiral Patterned Zinc Oxide Nanorod Coatings for Sensing Applications

Figure 5.1 shows the SEM image of optimized spiral patterned coating of ZnO nanorods for temperature and multiple optical channel alcohol vapor sensing. The SEM image in Figure 5.1(a) with magnification set at 10.00 kX clearly shows the spiral

patterned ZnO nanorods coating on POF. In the low-magnification image given below, the width of ZnO coating is 5 mm and the uncoated spacing is 10 mm in width.

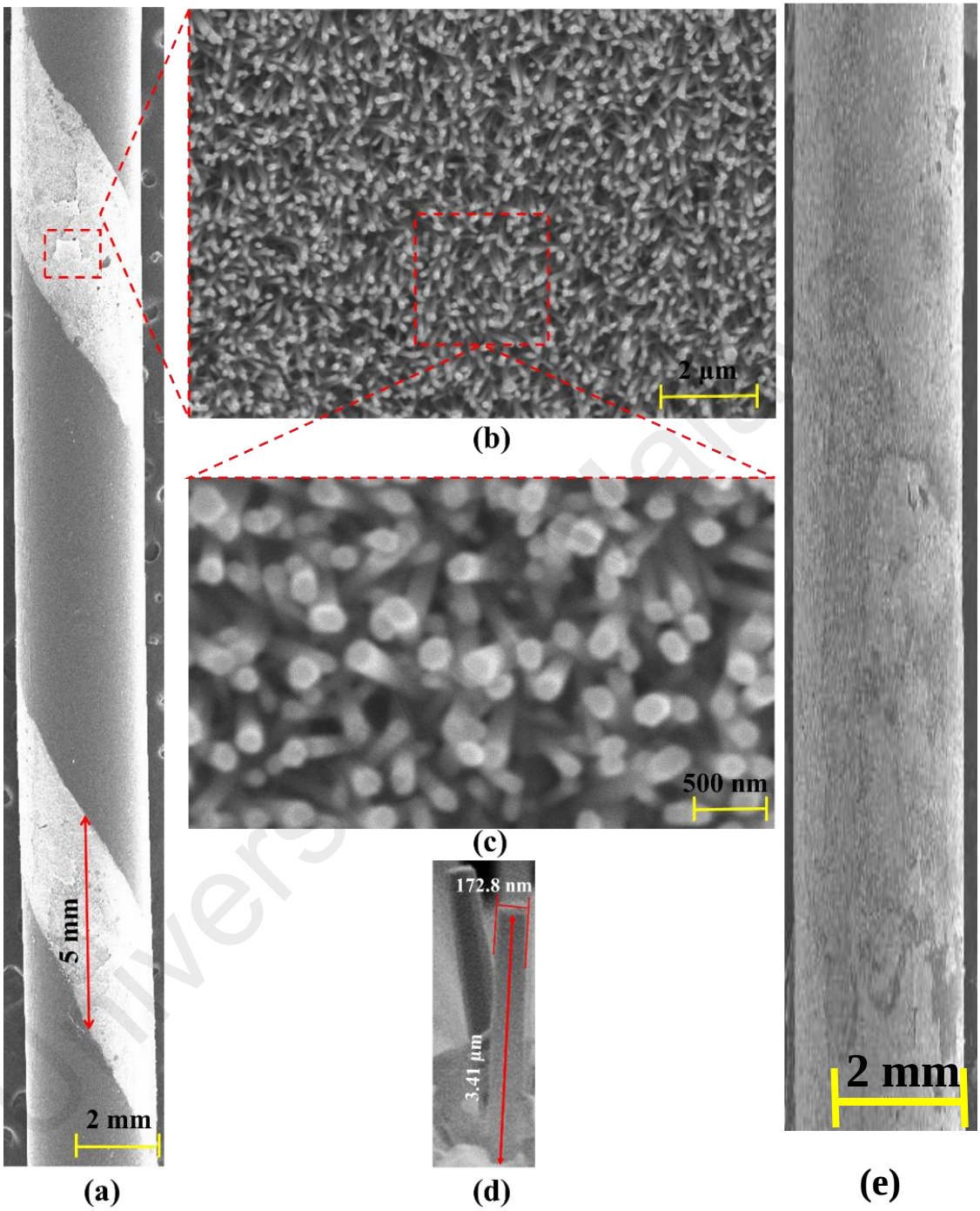

Figure 5.1 (a) The optimized spiral patterned ZnO nanorod coatings, (b) the perpendicular growth of ZnO nanorods on POF at low magnification (c) at high magnification (d) hight and diameter of the ZnO nanorod and (e) ZnO continuous coating on unpatterned POF

In Figure 5.1(b), ZnO nanorods can be seen growing perpendicular to the surface of the POF, an important geometry to enhance the light scattering mechanism for light side coupling into the POF. Moreover, the growth of ZnO nanorods on POF surface in Figure 5.1(b) observed at magnification of 15.00 kX reveals high density (85 nanorods / 3.62 X 10^{-12} m^2 = 23.50 X 10^6 nanorods/μm^2) and uniform distribution. Figure 5.1(c) shows the growth of ZnO nanorods with magnification of 30.00 kX. From the SEM images, the obtained ZnO nanorods were about 3.41 µm ± 0.05 µm in length and 172.8 nm ± 20 nm in diameter as shown in Figure 5.1(d).

5.3 Applied Light Side Coupling With Optimized Spiral Patterned Zinc Oxide Nanorod Coatings for Temperature Sensing

Conventional temperature sensors have their limitations if large distances have to be covered such as in many distributed measurements, electromagnetic interference leads to the loss of signal to noise ratio, explosive environments does not allow safe use of resistive devices and often in a plurality of applications they do not match when light-weight structures are desired. The fiber optic sensors market is a multi-billion dollar business which is prognosed to grow further and fiber optic based temperature sensors are an important class therein as they are immune to electro-magnetic interference and are thus robust and accurate in high-RF environments. Several measurement principles have been described in the literature for measuring temperature sensors such as intensity modulated fiber optic displacement sensor (FODS) (Rahman, Harun, Saidin, Yasin, & Ahmad, 2012), lifetime measurements (Z. Zhang, Grattan, & Palmer, 1992), microfiber loop resonator (MLR) (Harun, Lim, Damanhuri, & Ahmad, 2011) and stimulated brillouin scattering (Kurashima, Horiguchi, & Tateda, 1990), interferometer (H-Romano

et. al, 2015) and multicore fiber structure (A-Lopez et. al., 2014). Although, the temperature sensing using polymer-coated microfiber interferometer reported by I. H. Romano et al has a high sensitivity but it is not able to sense temperature changes at higher range due to low melting point of the polymer. In order to be economically advantageous, an optical fiber temperature sensor must be robust, easy-to-use, fast, accurate, stable over a wide measurement range and suitable for a large variety of applications (Li et al., 2012). In an application, many commercial electronic components can be damaged due to exposure to high temperature (> 70˚C) and some can be damaged by exposure to low temperatures (< 0˚C) (Mishra, Keimasi, & Das, 2004). Semiconductor devices and LCDs (liquid crystal displays) are examples of commonly used components that are susceptible to large temperature variations. In these cases, temperature sensing is indeed important so that appropriate measures can be incorporated to prolong the life of these devices. Optical fiber based temperature sensors are the only possibility in the presence of electromagnetic fields such as in microwave fields, power plants or explosion-proof areas and wherever measurement with electrical temperature sensors is not possible such as in high tension cable lines, airplanes, spacecrafts, electrical motors etc (Ramakrishnan, Rajan, Semenova, & Farrell, 2016).

In a previous report, temperature sensing was demonstrated using ZnO thin films where spectral absorption changes in ZnO was monitored (Hvedstrup Jensen, 1974). In this work we present optimized simple yet sensitive spiral patterned ZnO nanorod coatings on POF based temperature sensor capable of utilizing ambient light coupled through the nanorods into the fibers for sensing. Sensing performances of ZnO nanorod coatings, spirally patterned on POF fibers are presented and the results are compared to the sensing characteristics of the unpatterned fibers. Uncoated POF (bare) were not considered for this application since it does not show any scattering effects due to side coupling of light (Aneesh & Khijwania, 2011; Rahim et al., 2016).

5.3.1 Experiment of Temperature Sensing

The proposed temperature sensor is schematically illustrated in Figure 5.2. For maximal temperature detection, an aluminium rod with dimension of 0.3 and 10 cm in length was used. The aluminium rod is placed vertically on a hot plate and in closed contact with the physical POF coated with ZnO nanorods. For temperature monitoring, a thermocouple (type J) was fixed in closed contact with the POF as well. The thermocouple has a resolution of 1 ˚C and is able to measure the temperature within a range of 0 ˚C to 500 ˚C. A modulator circuit was used to minimize the noise in the measurement, the white-light LED current driver was modulated with a periodical pattern signal generated by a signal generator. The magnitude of light side coupling was measured by connecting one of the POF to photodector and displayed in millivolt (mV) on oscilloscope under illumination of the modulated visible white light source on the POF. The other one of the POF tip was covered during the experiments to avoid light entering directly through the tips. Then, temperature sensing measurement was carried out by varying temperature from 20 ˚C to 100 ˚C. Five readings were recorded for each measurement. The sensitivity (*S*) was obtained through the slope of sensing response for spirally patterned and unpatterned ZnO nanorod coated POF devices.

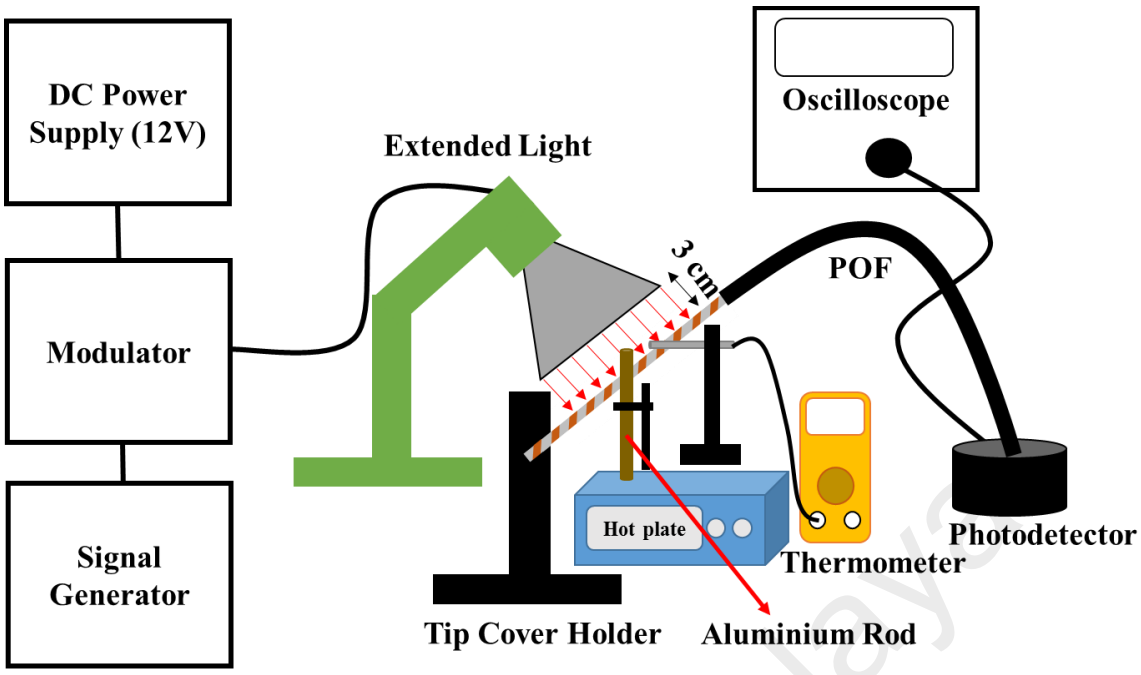

Figure 5.2 Experimental setup for the proposed temperature sensor towards light side coupling

5.3.2 Results and Discussions

The real time responses of the ZnO nanorod coated optical fiber sensor to temperature changes from 20 ˚C to 100 ˚C were recorded towards light side coupling. The measurements were conducted by exposing the spirally patterned and unpatterned ZnO nanorods coated POFs to temperature under visible light illumination. It was found that the both coating schemes showed obvious output voltage changes upon exposure to temperature as depicted in Figure 5.3. It is well known that the thermo-optic coefficient of the POF is an order of magnitude higher than that of glass optical fiber (GOF), and the refractive index (RI) of POF is affected by temperature variation. Therefore, the temperature dependence must be taken into account for POF based RI sensors. Several reports are available studying the temperature dependence of the RI sensors based on GOF technology (Han, Lee, & Lee, 2004; P. Wang, Semenova, & Farrell, 2008; P. Wang, Semenova, Wu, Zheng, & Farrell, 2010). As explained in section 4.4, the spirally

patterned ZnO nanorod coating leads to an increase in coupling of the light source compared to the unpatterned POF's due to the higher interfacial ZnO regions on the POF.

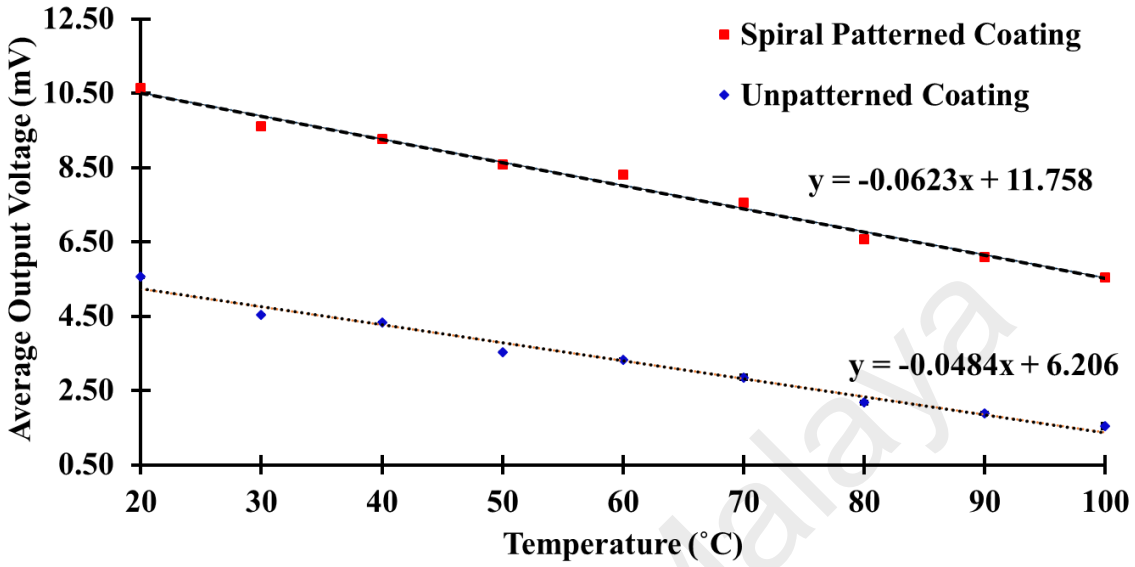

Figure 5.3 The response of spiral patterned coating and unpatterned coating in temperature sensing.

Earlier work showed that absorptivity of ZnO had a linear dependence on temperature using reflection measurements (Hvedstrup Jensen, 1974) and refractive index of ZnO coating layer changed at different temperature (Sanjeev & Kekuda, 2015). Figure 5.4 presents the sensing mechanism of the temperature sensor in this work using extinction concept which is the attenuation of light by scattering and absorption as it traverses the ZnO nanorods (Near, Hayden, & El-Sayed, 2012). Before visible light illumination was applied onto ZnO nanorods, light does not scatter into the POF as shown in Figure 5.4 (a). As visible light illuminates continuously onto the ZnO coating layer at a temperature of 20 ˚C, light scattered into the POF and a high intensity of guided light was detected due to low light absorption inside ZnO coating layer as illustrated in Figure 5.4 (b). When the POF coated with ZnO nanorods was closely touched to the heated aluminium rod following the continuous light illumination, the absorption of light inside

the ZnO nanorods coating increased and the amount of light scattering into the POF relatively reduced with increasing temperature within the range as depicted in Figure 5.4(c). Consequently, the intensity of guided light inside the POF decreased due to less light coupling. The excitation of oxygen molecules increased and obviously more energy was required that contributed to a high absorption inside ZnO nanorods coating layer.

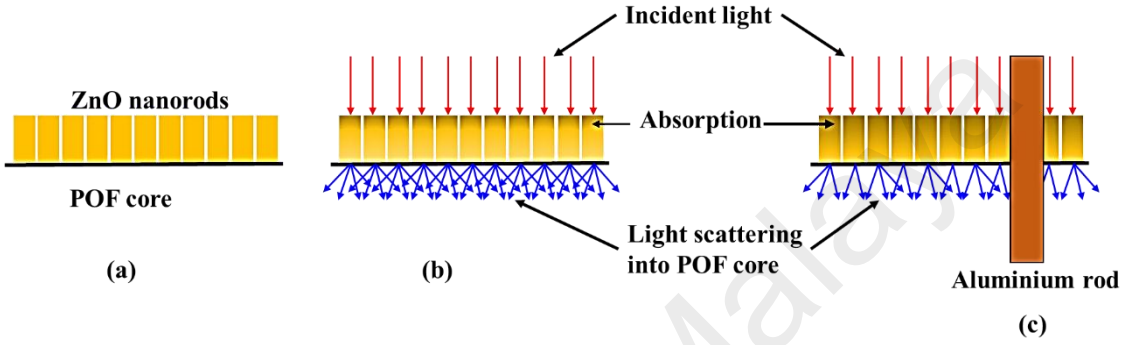

Figure 5.4 The temperature sensing mechanism (a) before light illumination (b) upon light illumination and (c) aluminum rod in close proximity to ZnO nanorods coating layer.

Figure 5.5 shows the sensitivities of the optical sensor coated with ZnO nanorods. In the case of spirally patterned coating, the sensor response to temperature changes was found to be 0.0623 mV/˚C. However, when the unpatterned coating was exposed to temperature changes, the sensitivity decreased to 0.0484 mV/˚C due to less coupling light inside POF. Moreover, spirally patterned coating consists of two exposed elements; ZnO nanorods coating and uncoated regions (polymer). Thermal effect can be effectively sensed by spiral patterned POF because the uncoated regions contributes also to optical loss which is dependent on temperature. The loss is reported to increase with increasing temperature (Husdi, Nakamura, & Ueha, 2004; Minakawa et al., 2014). In the temperature sensing, sensitivity was measured to be a factor of 1.3 times better for spiral patterned coatings as opposed to unpatterned coatings. Moreover, this temperature sensor demonstrated a higher sensitivity compared to other optical fiber temperature sensors

which usually use common sensing method by introducing light from one end and collecting at the other end (Ju, Watekar, & Han, 2009; Rahman, Harun, Saidin, et al., 2012). It was observed that the spiral patterned coating is able to monitor temperature to 0.1284 ˚C resolution and unpatterned coating has a resolution of 0.2273 ˚C. Based on this performance, the optimized spiral patterned ZnO nanorod coating was further used for multiple optical channel alcohol vapor sensing.

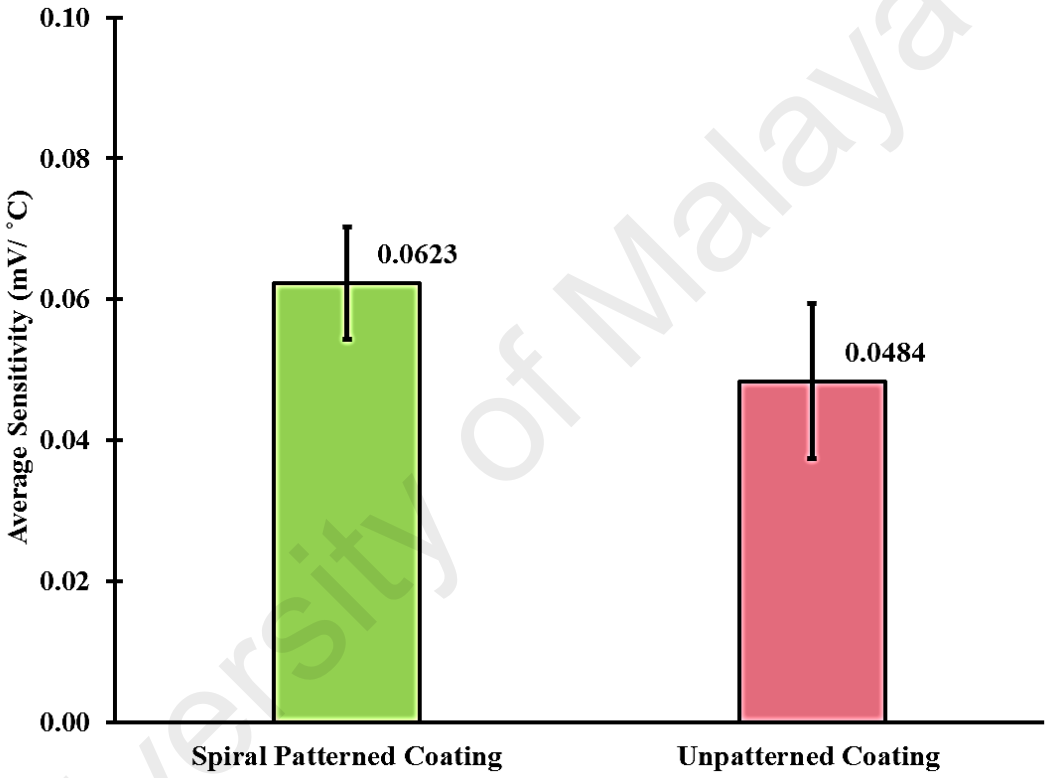

Figure 5.5 The sensitivity of spiral patterned and unpatterned coating in temperature sensing

5.4 Applied Light Side Coupling With Optimized Spiral Patterned Zinc Oxide Nanorod Coatings for Multiple Optical Channel Alcohol Vapor Sensing.

A chemical sensor is a device that transforms chemical information in the form of concentration of a specific material into an analytically useful signal (Hulanicki, Glab, & Ingman, 1991). A large number of commercially available chemical measurement

systems are found in the market today and can be classified by the type of analytical signal required for measurement. For optical-based instrumentation, these include, among others, absorbance (Puyol et al., 2005), luminescence (Leiner, 1991), light scattering (McFarland & Van Duyne, 2003), and fluorescence (Liebsch, Klimant, Krause, & Wolfbeis, 2001). Due to the simplicity of directing light into a sensing platform, optical fibers have found applications for the measurement of chemicals in food (McCorkle et al., 2005; Morisawa & Muto, 2012; Narsaiah, Jha, Bhardwaj, Sharma, & Kumar, 2012; Shenhav et al., 2013), security industry safes (Clevenson, Desjardins, Gan, & Englund, 2013) and clinical materials (Shenhav et al., 2013). Nowadays, optical fiber sensors have been integrated with nanotechnology in utilizing visible light as light source for various sensing applications.

In the experiment, the responses of alcohol vapors were observed in spectral of visible wavelength towards light side coupling. The behavior of light scattering changed when the spiral patterned ZnO nanorods coating on POF exposed to alcohol vapors. The performances of the optical sensor were investigated as a multiple optical channel sensing in visible wavelength.

5.4.1 Experiment of Multiple Optical Channel for Alcohol Vapor Sensing

Figure 5.6 shows the experimental setup used for optical sensing of alcohols. The apparatus consisted of a spectrometer (USB4000, Ocean Optics) and a sensing chamber (0.18 m x 0.2 m x 0.27 m). A visible white light source with wavelength 380 to 750 nm was used to induce light side coupling. The intensity of the white light source was modulated with a periodical pattern using the modulator in order to minimize the background effect. It is worth mentioning that here a spectrometer was connected to the end of the POF in order to record the spectrum of the coupled light. During the investigation of sensor performance, ambient air was passed through the sensing chamber

at room temperature (ca. 26 ºC) and relative humidity of 45% until a steady state condition (0 ppm) was obtained. The white light source was placed 3 cm from the POF surface. A known amount of alcohol was vaporized and introduced into the sensing chamber as the target gas. Three kinds of alcohol were tested: 1. ethanol [CH_3CH_2OH] (Merck KGaA, Germany, 99.8 %), 2. methanol [CH_3OH] (J.T.Baker, USA, 99.8%) and 3. isopropanol [C_3H_7OH] (Merck KGaA, Germany, 99.5%). The spectral response towards alcohol vapor was recorded every 10 seconds from 0 ppm to 300 ppm. In the experiment, the concentration (C) of target alcohol vapor in ppm was computed using the following equation (Peng et al., 2010).

$$C = \frac{T \times V_t \times D_t}{V_c \times M_t} \times R \tag{5.1}$$

where T is the operating temperature in Kelvin (K), V_c is the volume (ml) of the diluted target gas which is equal to the volume of the sensing chamber. V_t, D_t and M_t represent the volume (µl), density (g/ml) and molecular weight (g/mol) of the alcohol analyte, respectively. R is the universal gas constant which is equal to 8.2 x 10^4 $JK^{-1}mol^{-1}$.

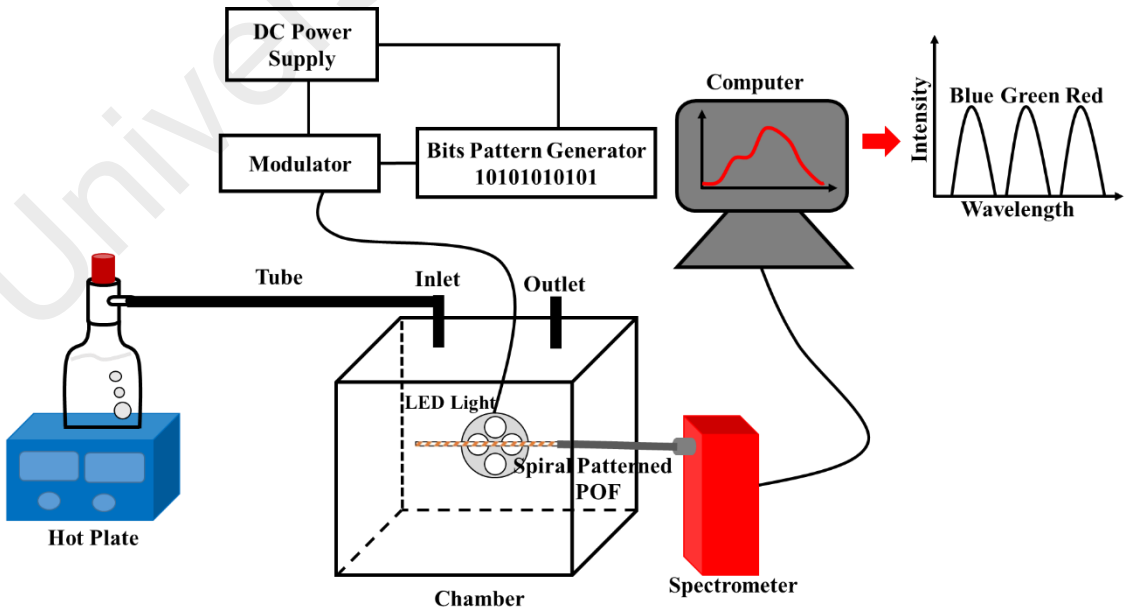

Figure 5.6 Experimental setup to validate the alcohol sensing activities of spiral patterned POF as multiple optical channels

From the recorded visible spectrum (380 nm – 750 nm), the response from three specific ranges (referred to here as channels) was studied - blue (450 – 495 nm), green (495-570 nm) and red (620 – 750 nm). In the channels, the measured transmittance average values and standard deviations were obtained for the all concentrations of the alcohol vapors. The sensing performances in each channels were investigated by analyzing the effects on light intensity towards the all alcohol vapor concentrations. The sensing effects were presented in term of relative intensity modulation (RIM) in arbitrary unit (a.u) (L. Grattan & Meggitt, 2013) that was calculated using the following equation.

$$RIM = \frac{I_{f(av)} - I_{i(av)}}{I_{i(av)}} \tag{5.2}$$

where I_f is the smallest average intensity after injection of alcohol vapor and I_i is the average initial intensity before injection of alcohol vapor under light illumination . The RIMs were obtained for each alcohol vapor response in all three channels. To create an inexpensive multichannel sensing system using red, green and blue LEDs and a simple photodetector, a preliminary reference was developed through division of higher responses from two of the three channels with respect to channel that produces lowest response. It is worth noting here that the aim of this part of the experiment was to study the efficiency of utilizing only three color channels (Red, Green, Blue) for different vapors sensing. This can be possibly extended to the use of RGB LED with lower cost photo-detector instead of a spectrometer.

5.4.2 Results and Discussions

The improved side coupling by the spiral patterned coating of ZnO nanorods on POF is exploited to demonstrate sensor performances in different wavelength domains of visible light called channels to sense three different alcohol vapors (methanol, ethanol and isopropanol) as shown in Figure 5.7. All sensing was accomplished with the optimized spiral ZnO coating width of 5 mm. It was found that the sensor demonstrated three different responses for methanol, ethanol and isopropanol vapors as a function of molecular weights (methanol < ethanol < isopropanol), relative dielectric constants and polarity. The relative dielectric constants of methanol (33), ethanol (24) and isopropanol (20), for example, most likely influenced selective alcohol vapor molecule adsorption onto different crystal faces of the ZnO nanorods (Wiederrecht, 2010). The amount of vapor adsorption coupled with the region of adsorption on the ZnO therefore played the major roles in the attenuation of the coupled light signal. Additionally, the refractive indices of methanol (1.328), ethanol (1.361) and isopropanol (1.377) also affected the interaction of light by varying the refractive index of ZnO nanorods coating (Yebo, Lommens, Hens, & Baets, 2010). Interestingly, in the presence of methanol, the intensity was seen to decrease significantly indicating lower side coupling of light into the POF. This was due to the change in the refractive index of the ZnO coating layer caused by methanol absorption. During sensor recovery, as methanol evaporated from the layer of ZnO nanorods coating, the sensor output was observed to return closely to the initial condition in ca. 7 minutes. For ethanol and isopropanol, the sensor also demonstrated similar response patterns caused by rising adsorption onto ZnO nanorods.

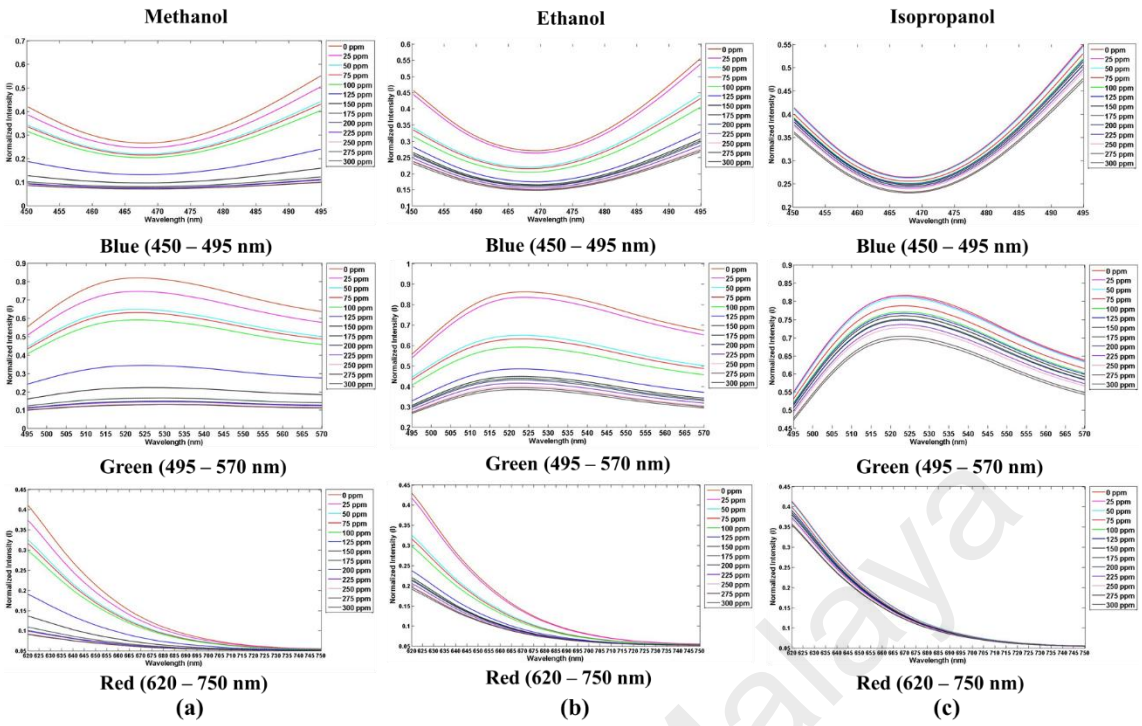

Figure 5.7 Spectroscopy responses of multiple optical channels sensor in blue, green, and red wavelengths for (a) methanol, (b) ethanol and (c) isopropanol

However, the sensor demonstrated slight response to isopropanol vapor molecules compared to ethanol. The recovery time for ethanol and isopropanol were ca. 5 minutes and ca. 3 minutes, respectively. The decrease of light intensity when exposed to the alcohol vapors and the recovery towards initial value is believed to be due to chemisorption process, the interaction of hydrogen-bonding between –OH groups of alcohol molecules with ZnO coating layer (Jaisai, Baruah, & Dutta, 2012). Due to small size of methanol molecules compared to ethanol and the biggest molecule size, isopropanol, the chemisorption process between methanol molecules and ZnO coating layer is very high that took more time to recover relatively to initial value.

The change in the refractive index of the ZnO coating layer due to absorption process that affects the amount of light scattering into POF can be explained clearly using the sensing mechanism depicted in Figure 5.8. Initially, ZnO nanorods were exposed to air at room temperature as shown in Figure 5.8 (a). In this case, ionized oxygen is

chemisorbed onto the surface in its molecular form, O_2^-, as given in Equation (5.3) (Alenezi et al., 2013).

$$O_2 \text{ (gas)} + e^- \leftrightarrow O_2^- \tag{5.3}$$

As the surface is illuminated continuously by visible light as shown in Figure 5.8(b), changes in the carrier density in the ZnO nanorods and the layer of depletion depth occur. Once electron−hole pairs are generated by the visible light, holes migrate to the surface and discharge the adsorbed oxygen molecules. This causes the depth of the depletion layer to decrease, resulting in the desorption of surface oxygen. Over time, unpaired electrons accumulate until the desorption and adsorption of oxygen reaches an equilibrium state. The amount of adsorbed oxygen decreases compared to air conditions as shown in Figure 5.8 (a). The presence of excitons under visible light irradiation leads to the formation of atomic adsorbed oxygen, O^-, which is substantially more chemically active than O_2^- and creates favorable conditions for catalytic reactions (Barry & Stone, 1960; Fan, Srivastava, & Dravid, 2009). This phenomena contributed to the amount of light scattering into optical core fiber by the ZnO nanorods. When gases (such as methanol in this case) are introduced, the adsorbed oxygen on ZnO nanorods took part in the oxidation of methanol in two possible ways (Equation (5.4) and (5.5)) (Patel, Patel, & Vaishnav, 2003). The oxygen ions on the surface of ZnO reacted with the methanol molecules and give up electrons to the conduction band and increase the carrier concentration in the ZnO nanostructure as shown in Figure 5.8(c).

$$CH_3OH + O^- \leftrightarrow HCHO + H_2O + e^- \tag{5.4}$$

$$CH_3OH + O_2^- \leftrightarrow HCOOH + H_2O + e^- \tag{5.5}$$

As a result, scattering attenuation was therefore a function of the type of molecular species adsorbed onto the ZnO surface (e.g. its refractive index, *n*) and the amount of that

material present, allowing these molecules to interact differently with the incoming light. At the same time different organic molecules have different refractive indices, molecule sizes and band-bending occurs at surface which will also affect the interaction of incoming light by varying the *n* of the outer coating differently (Yebo et al., 2010).

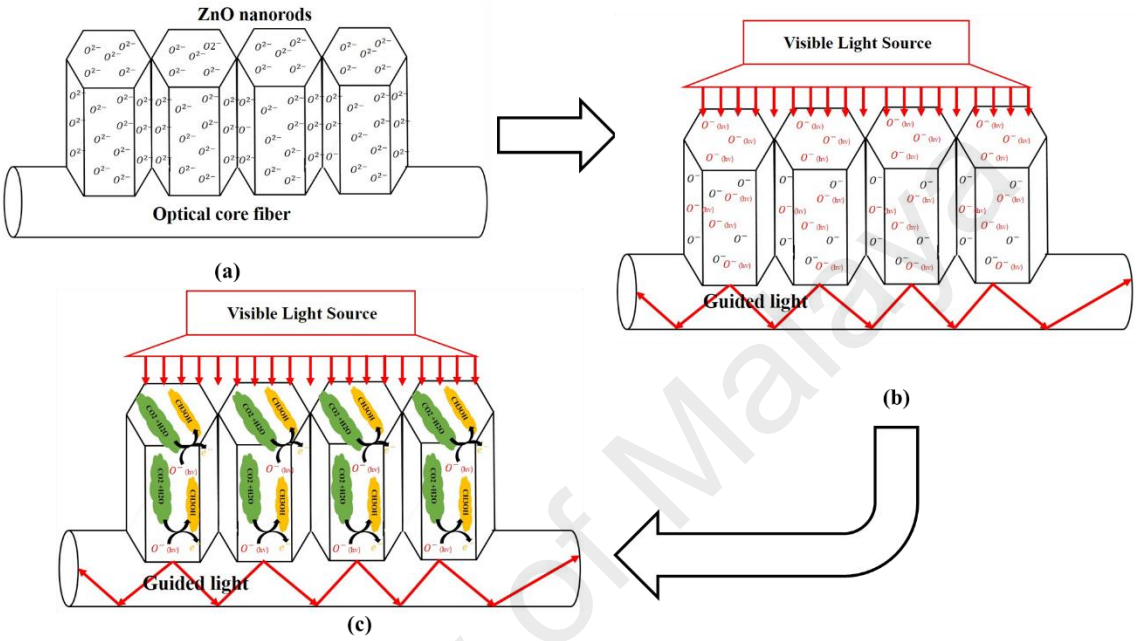

Figure 5.8 Schematic diagram of the alcohol sensing mechanism activated using visible white light illumination (a) in air at room temperature (b) with visible white light and (c) with methanol exposure

As observed from the responses of the sensor in multiple optical channels as shown in Figure 5.9, different wavelengths of light as well contributed to determining the amount of chemical vapor absorption onto ZnO nanorods with attenuated light scattering into the POF. In this result, the green channel presented the largest range of intensity (0.11 – 0.87) followed by the blue channel (0.07 - 0.41) and then, with the lowest intensity, the red channel (0.05 – 0.17). It can be concluded that the intensity of green light in ZnO nanorods dramatically decreased with the increase in vapor concentration as alcohol molecules are adsorbed onto the ZnO coating.

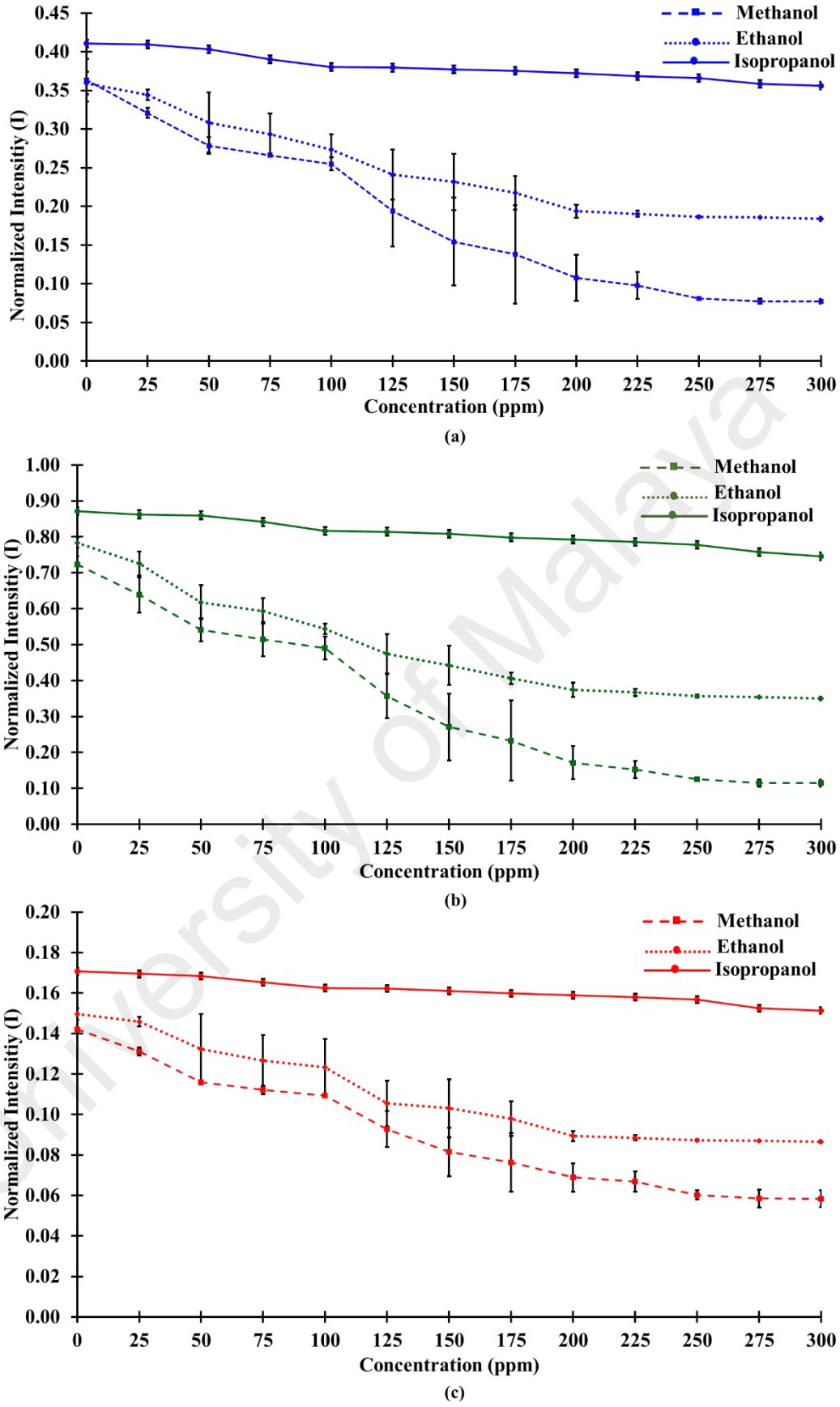

Figure 5.9 The responses of multiple optical channels sensor in channel (a) blue (b) green and (c) red

Subsequently, there was a degree of attenuation of light scattering into POF. It was shown in references (H. Lin et al., 2006; Vanheusden, Warren, Seager, Tallant, Caruso, et al., 1996; Vanheusden, Warren, Seager, Tallant, Voigt, et al., 1996) that the luminance characteristic of ZnO has a significant response in green spectral range due to the strong influence by free-carrier depletion at the particle surface, particularly for small ZnO particles. Moreover, upon exposure to visible light, ZnO nanorod coating will be photoactivated leading to reduced inter - grain barrier height, thereby increasing the density of free carriers in the material. Boiling points of primary alcohols in these experiments are methanol: 65 ˚C; ethanol: 78 ˚C; isopropanol: 82 ˚C which are related anyway to the bond dissociation energies. Hence, the order of sensitivity was in the reverse order. This leads to the specific heats of vaporization which is the lowest for isopropanol (0.471 kJ/g) compared to ethanol (0.925 kJ/g) and methanol (1.22 kJ/g).

Figure 5.10 shows the relative intensity modulations (RIMs) of the multichannel optical sensor for alcohol vapors. The RIMs of the sensor in each channel were calculated using Eq. (5.2). The absolute of the light intensity decreased rapidly with increasing the alcohol vapors concentration from 0 – 300 ppm. The green channel contributed the highest RIMs for all three alcohols. Measurements in the blue light domain showed intermediate RIMs, and lastly, the red channel exhibited significantly lower RIMs of all three light domains for all alcohols tested. For the green channel, the sensor response for methanol was found to be 0.84 a.u. However, when ethanol and isopropanol were tested, the RIM decreased to 0.55 a.u and 0.14 a.u, respectively. In the case of the blue channel, sensor response to methanol also presented the highest RIM of the three alcohols equal to 0.79 a.u. For ethanol and isopropanol, once again, decreased but to lower levels than those observed for the green channel- 0.49 a.u and 0.13 a.u, respectively. The same trends in alcohol RIM based on molecular weight was demonstrated by the red channel but to the lowest levels of the three light domains.

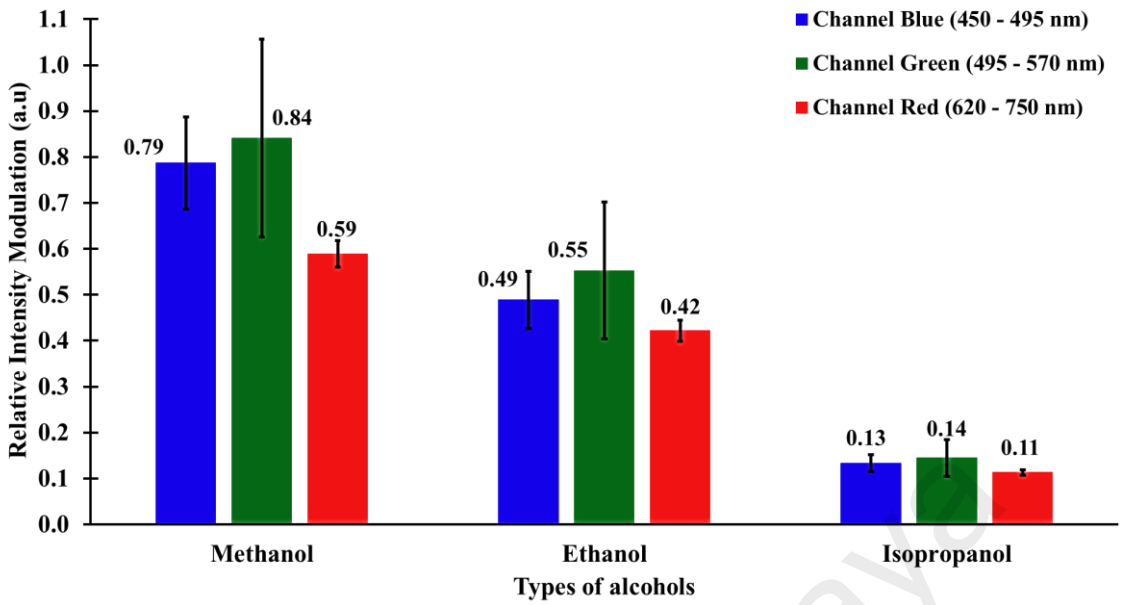

Figure 5.10 The relative intensity modulation (RIM) of multiple optical channels sensor exposed to ethanol, methanol and isopropanol vapors

The optimum RIM for isopropanol is smaller than that of ethanol due to reduced absorption onto the ZnO nanorods by the larger molecular weight and slightly less polar molecule (Alenezi et al., 2013). Channel green demonstrated significant RIMs in sensing the three alcohol vapors because ZnO nanorods have both polar and non-polar surfaces as reported in (M. Huang et al., 2014) where zinc vacancies (VZn) at the nonpolar surfaces are responsible for the green luminescence of ZnO nanostructures (Fabbri et al., 2014). The presence of neutral VZn on ZnO coating generates a multiple effect: the absence of Zn ions leaves out under coordinated O atoms, and the unpaired O electrons give rise to empty states. As a consequence, this leads to a high absorption in green luminescence due to strong O-H chemical bonds (Willander et al., 2010).

A preliminary reference was developed by performing cross validation on channel blue and green with respect to channel red that produced the minimal response for the alcohol vapors as shown in Figure 5.10 in order to create an inexpensive multichannel sensing system using red, green and blue LEDs and a simple photodetector. To observe the response of the sensor as a multichannel device, one of the three channels was set as a reference to accommodate for source fluctuation and environment effect (heat and

vibration for example). The other two readings are normalized to the reference and the RIM of different gas vapors to these channels are examined.

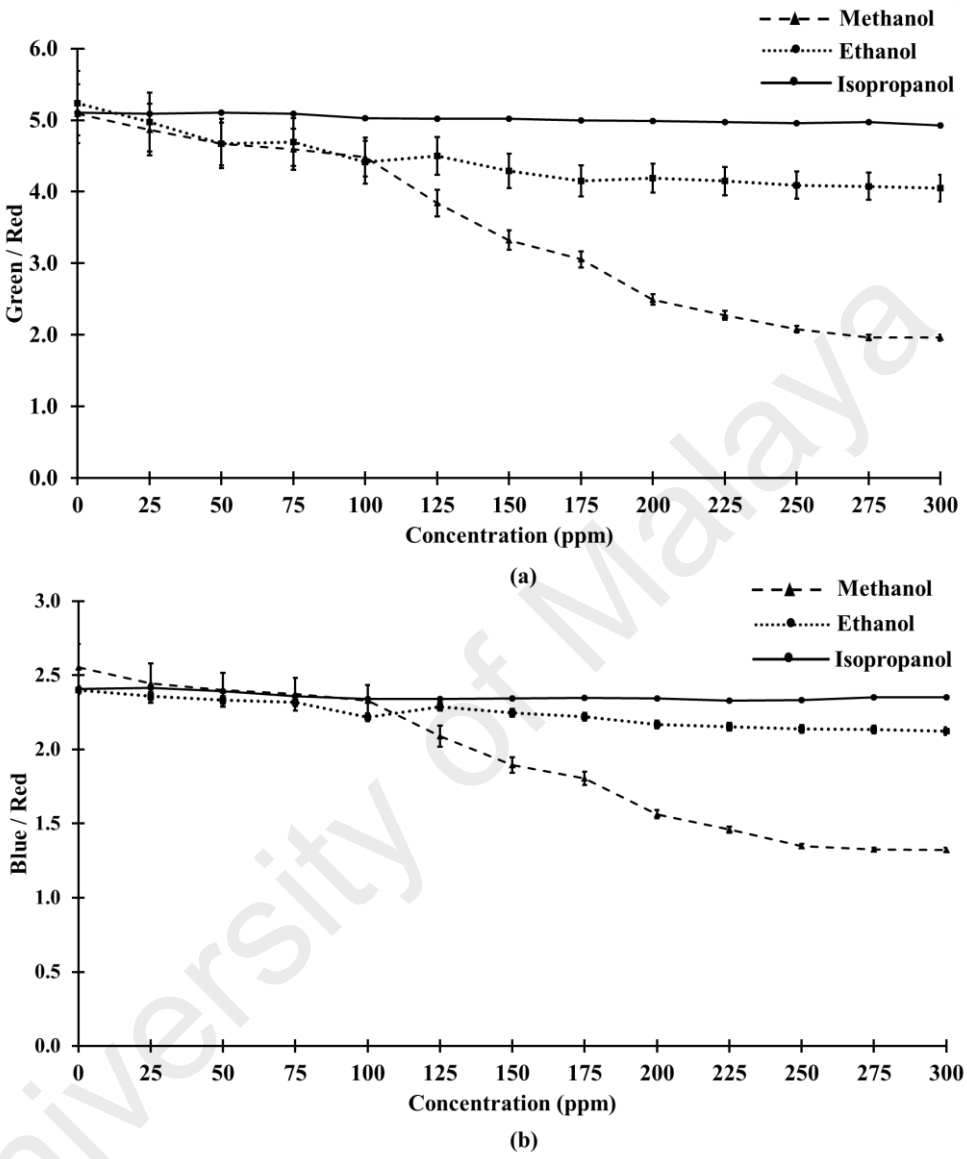

Figure 5.11 The validation of the multiple optical channels sensor for (a) channel blue/ channel red (b) channel green/ channel red

In both validations, the three alcohol vapors illustrated a similar pattern response at two different ranges which were ~1.3 – 2.5 for channel blue/channel red and ~ 2.0 – 5.2 for channel green/ channel red. In these ranges, significant responses were seen clearly in methanol and ethanol sensing compared to isopropanol that showed less response.

5.5 Summary

The study implemented successfully light side coupling with optimized spiral patterned zinc oxide nanorod coatings for temperature and multiple optical channel alcohol vapor sensing. The inherent advantages of optical fibers paired with the transparency of ZnO nanorods in the visible wavelength region were applied to design a simple and cost effective optical sensor. With increasing temperature, the coupled light was found to reduce, which was used for calibrating as a temperature sensor. The spirally patterned ZnO nanorods coating demonstrated significant improvement (1.3 times better sensitivity) in the coupled light power compared to unpatterned coatings, since scattering of light is dependent on the refractive index of ZnO surface and highly sensitive to ZnO absorption. These robust but simple temperature sensors can find wide ranging applications for environmental monitoring (Schroeder, Yamate, & Udd, 1999), biomedical purposes (Korolyov & Potapov, 2012) as well as in environments with electromagnetic pollution and/or explosive conditions. For instance, it can be also used as a visible light photosensitive indicator for those who have photosensitivity diseases related to sunlight or interior lighting. This proposed sensor is able to indicate the intensity level of light at that a particular area due to excitation of ZnO upon receiving photons to scatter light into POF.

Practical application of the special POF system also showed promise as a multiple optical channel sensor for alcohol vapors in the visible range of the spectrum. To explain the mechanism of sensing for alcohols, it was proposed that the light scattering aspect of the ZnO nanorods dependent on changes in the refractive index was affected by adsorption of alcohol species. With regard to sensing performance in the three spectral channels described previously, methanol showed the greatest RIM and range followed by ethanol and isopropanol. In the investigation of a multiple optical channel sensor, the green channel significantly produced higher RIMs in sensing methanol, ethanol and

isopropanol vapors compared to the blue and red channels. Furthermore, a preliminary reference was developed in order to propose a multiple optical channels sensor system using inexpensive color LEDs (blue, green and red) as light sources and a simple photodetector in applications.

CHAPTER 6: CONCLUSION AND FUTURE WORK

This chapter presents the overall summary of the results and conclusions. The research described in this thesis showed a possibility of applying structuring growth of ZnO nanorods on POF for various sensing applications. Although some comprehensive conclusions were able to be drawn, the whole spectrum of questions was not exhausted. The summary of the author's conclusions and experiences is written below in hope that they may be helpful to someone who will continue this research work.

6.1 Conclusion

Structured growth of ZnO nanorods on POF has been successfully performed using hydrothermal method. The size and morphology of the ZnO nanorods could be varied through the changes in the concentration of the reactants, temperature, growth duration and seeding technique. The study also demonstrated controlled light scattering and efficient light coupling into the core modes of the ZnO nanorod coated POF. The hydrothermal growth duration of the ZnO nanorods were found to be important in the light coupling efficiency. From the optical characterization it was seen that the spiral structure growth of the ZnO nanorods on POF for a growth duration of 12 hours at 90 ˚C provided the maximum coupling power. The spiral pattern structure also has an improved transmittance factor of 2.2 compared to the unpatterned coating with an extended light source.

A new theoretical model specifically for light scattering from ZnO nanorods coated POF have been successfully analysed the effect on coupling power by varying the width of spiral structure. From the analysis, the width of spiral patterned ZnO nanorod coatings on POF was optimized theoretically for maximum light side coupling with a constant amplitude of light source and found to be 5 mm. The theoretical model also proved that Gaussian beam was not able to couple light efficiently towards light side

coupling. The width of spiral patterned ZnO nanorods coating on POF was experimentally optimized and the experimental results correlated well with the simulations.

A major highlight of this project was the use of POF as optical sensors using ZnO nanorods. The inherent advantages of optical POF paired with the transparency of ZnO nanorods in the visible wavelength region were incorporated to design a simple and cost effective optical sensor for various applications. One-dimensional nanostructures with very high surface to volume ratio can be attractive candidates for sensing purposes. The possibility of light side coupling shown by the ZnO nanorods coated POF was exploited as an optical temperature sensor. The experiment carried out on temperature sensing showed a decrease in the coupled power as the temperature increases for the both coating schemes. Spiral patterned coating demonstrated higher sensitivity compared to unpatterned coating.

Further, the application was extended to the use of the fabricated POF as multiple optical channel alcohol vapour sensor by utilizing the scattering properties of spiral patterned ZnO nanorods grown on POF. The ZnO nanorod coated POF demonstrated significant change in the coupled power in the presence of ethanol, methanol and isopropanol vapours, since scattering of light is dependent on the nature of the surface and highly sensitive to any changes on the surface. It was found that with increase in the concentration of the alcohol vapours from 25 ppm to 300 ppm, the coupled light decreases. This had a direct impact on the sensitivity. The spectral results were analysed among which methanol gave a strongest response compared to ethanol and isopropanol in three channels: red (620-750 nm), green (495-570 nm) and blue (450-495 nm). With regard to alcohol detection sensitivity by spectral band, the green channel demonstrated the highest RIM values followed by the blue and red channels respectively.

6.2 Future work

As future recommendations, the investigation can be further extended to increase the coupling efficiency by using two or more POF coated with spiral patterned ZnO nanorods coating. In addition, enhancement of the sensor system can be achieved through an integration with an artificial intelligent (AI) system to sense even the smallest of physical parameter changes. In application, the fabricated POF can be used as a probe in optical wireless energy harvesting.

REFERENCES

Abdelghani, A., Chovelon, J., Jaffrezic-Renault, N., Ronot-Trioli, C., Veillas, C., & Gagnaire, H. (1997). Surface plasmon resonance fibre-optic sensor for gas detection. *Sensors and Actuators B: Chemical, 39*(1), 407-410.

Agbabiaka, A., Wiltfong, M., & Park, C. (2013). Small Angle X-Ray Scattering Technique for the Particle Size Distribution of Nonporous Nanoparticles. *Journal of Nanoparticles, 2013*.

Alenezi, M. R., Alshammari, A. S., Jayawardena, K., Beliatis, M. J., Henley, S. J., & Silva, S. (2013). Role of the exposed polar facets in the performance of thermally and UV activated ZnO nanostructured gas sensors. *The Journal of Physical Chemistry C, 117*(34), 17850-17858.

Amin, G., Asif, M., Zainelabdin, A., Zaman, S., Nur, O., & Willander, M. (2011). Influence of pH, precursor concentration, growth time, and temperature on the morphology of ZnO nanostructures grown by the hydrothermal method. *Journal of Nanomaterials, 2011*, 5.

Aneesh, R., & Khijwania, S. K. (2011). Zinc oxide nanoparticle based optical fiber humidity sensor having linear response throughout a large dynamic range. *Applied optics, 50*(27), 5310-5314.

Antonio-Lopez, J. E., Eznaveh, Z. S., LiKamWa, P., Schülzgen, A., & Amezcua-Correa, R. (2014). Multicore fiber sensor for high-temperature applications up to 1000 C. *Opt Lett, 39*(15), 4309-4312.

Antunes, P. F., Varum, H., & Andre, P. S. (2013). Intensity-encoded polymer optical fiber accelerometer. *Sensors Journal, IEEE, 13*(5), 1716-1720.

Ao, W., Li, J., Yang, H., Zeng, X., & Ma, X. (2006). Mechanochemical synthesis of zinc oxide nanocrystalline. *Powder Technology, 168*(3), 148-151.

Aoki, T., Hatanaka, Y., & Look, D. C. (2000). ZnO diode fabricated by excimer-laser doping. *Applied physics letters, 76*(22), 3257-3258.

Arditty, H., Papuchon, M., & Puech, C. (1981). Fiber-optic rotation sensor: Toward an integrated device; A review. *Quantum Electronics, IEEE Journal of, 17*(12), 2454-2454.

Ashfold, M. N., Doherty, R. P., Ndifor-Angwafor, N. G., Riley, D. J., & Sun, Y. (2007). The kinetics of the hydrothermal growth of ZnO nanostructures. *Thin Solid Films, 515*(24), 8679-8683.

Aslam, M., Chaudhary, V., Mulla, I., Sainkar, S., Mandale, A., Belhekar, A., & Vijayamohanan, K. (1999). A highly selective ammonia gas sensor using surface-ruthenated zinc oxide. *Sensors and Actuators A: Physical, 75*(2), 162-167.

Ayouchi, R., Martin, F., Leinen, D., & Ramos-Barrado, J. (2003). Growth of pure ZnO thin films prepared by chemical spray pyrolysis on silicon. *Journal of Crystal Growth, 247*(3), 497-504.

Banerjee, D., Lao, J., Wang, D., Huang, J., Ren, Z., Steeves, D., . . . Sennett, M. (2003). Large-quantity free-standing ZnO nanowires. *Applied physics letters, 83*(10), 2061-2063.

Barry, T., & Stone, F. (1960). *The reactions of oxygen at dark and irradiated zinc oxide surface.* Paper presented at the Proceedings of the Royal Society of London A: Mathematical, Physical and Engineering Sciences.

Baruah, S., & Dutta, J. (2008). Hydrothermal growth of ZnO nanostructures. *SCIENCE AND TECHNOLOGY OF ADVANCED MATERIALS*.

Baruah, S., & Dutta, J. (2009a). Effect of seeded substrates on hydrothermally grown ZnO nanorods. *Journal of Sol-Gel Science and Technology, 50*(3), 456-464. doi: DOI 10.1007/s10971-009-1917-2

Baruah, S., & Dutta, J. (2009b). Hydrothermal growth of ZnO nanostructures. *SCIENCE AND TECHNOLOGY OF ADVANCED MATERIALS, 10*(1), 18. Doi 10.1088/1468-6996/10/1/013001

Baruah, S., K Pal, S., & Dutta, J. (2012). Nanostructured zinc oxide for water treatment. *Nanoscience & Nanotechnology-Asia, 2*(2), 90-102.

Batumalay, M., Harith, Z., Rafaie, H., Ahmad, F., Khasanah, M., Harun, S., . . . Ahmad, H. (2014). Tapered plastic optical fiber coated with ZnO nanostructures for the measurement of uric acid concentrations and changes in relative humidity. *Sensors and Actuators A: Physical, 210*, 190-196.

Benhebal, H., Chaib, M., Salmon, T., Geens, J., Léonard, A., Lambert, S. D., . . . Heinrichs, B. (2013). Photocatalytic degradation of phenol and benzoic acid using zinc oxide powders prepared by the sol–gel process. *Alexandria Engineering Journal, 52*(3), 517-523.

Berginski, M., Hüpkes, J., Schulte, M., Schöpe, G., Stiebig, H., Rech, B., & Wuttig, M. (2007). The effect of front ZnO: Al surface texture and optical transparency on efficient light trapping in silicon thin-film solar cells. *Journal of applied physics, 101*(7), 074903.

Bhattacharyya, P., Basu, P., Saha, H., & Basu, S. (2007). Fast response methane sensor using nanocrystalline zinc oxide thin films derived by sol–gel method. *Sensors and Actuators B: Chemical, 124*(1), 62-67.

Bora, T., Fallah, H., Chaudhari, M., Apiwattanadej, T., Harun, S. W., Mohammed, W. S., & Dutta, J. (2014). Controlled side coupling of light to cladding mode of ZnO nanorod coated optical fibers and its implications for chemical vapor sensing. *Sensors and Actuators B: Chemical, 202*, 543-550.

Bosc, D., & Toinen, C. (1993). Tensile mechanical properties and reduced internal stresses of polymer optical fiber. *Polymer composites, 14*(5), 410-413.

Budiansky, B., Drucker, D., Kino, G., & Rice, J. (1979). Pressure sensitivity of a clad optical fiber. *Applied optics, 18*(24), 4085-4088.

Byrne, C., & Lim, C. L. (2007). The ingestible telemetric body core temperature sensor: a review of validity and exercise applications. *British journal of sports medicine, 41*(3), 126-133.

Cao, H., Zhao, Y., Ong, H., Ho, S., Dai, J. Y., Wu, J. Y., & Chang, R. (1998). Ultraviolet lasing in resonators formed by scattering in semiconductor polycrystalline films. *Applied physics letters, 73*(25), 3656-3658.

Chang, C.-C., Chiu, N.-F., Lin, D. S., Chu-Su, Y., Liang, Y.-H., & Lin, C.-W. (2010). High-sensitivity detection of carbohydrate antigen 15-3 using a gold/zinc oxide thin film surface plasmon resonance-based biosensor. *analytical chemistry, 82*(4), 1207-1212.

Chen, D., Jiao, X., & Cheng, G. (1999). Hydrothermal synthesis of zinc oxide powders with different morphologies. *Solid State Communications, 113*(6), 363-366.

Chen, H., Roco, M. C., Son, J., Jiang, S., Larson, C. A., & Gao, Q. (2013). Global nanotechnology development from 1991 to 2012: patents, scientific publications, and effect of NSF funding. *Journal of nanoparticle research, 15*(9), 1-21.

Chen, J., Zeng, F., Li, D., Niu, J., & Pan, F. (2005). Deposition of high-quality zinc oxide thin films on diamond substrates for high-frequency surface acoustic wave filter applications. *Thin Solid Films, 485*(1), 257-261.

Cherin, A. H. (1983). An Introduction To Optical Fibers.

Chiu, W., Khiew, P., Cloke, M., Isa, D., Tan, T., Radiman, S., . . . Lim, H. (2010). Photocatalytic study of two-dimensional ZnO nanopellets in the decomposition of methylene blue. *Chemical Engineering Journal, 158*(2), 345-352.

Chong, X., Kim, K.-J., Li, E., Zhang, Y., Ohodnicki, P. R., Chang, C.-H., & Wang, A. X. (2016). Near-infrared absorption gas sensing with metal-organic framework on optical fibers. *Sensors and Actuators B: Chemical, 232*, 43-51.

Chong, X., Kim, K.-J., Ohodnicki, P. R., Li, E., Chang, C.-H., & Wang, A. X. (2015). Ultrashort Near-Infrared Fiber-Optic Sensors for Carbon Dioxide Detection. *Sensors Journal, IEEE, 15*(9), 5327-5332.

Clevenson, H., Desjardins, P., Gan, X., & Englund, D. (2013). *Gas sensing using a resilient polymer photonic crystal nanocavity with ultra-high quality factor*. Paper presented at the CLEO: Applications and Technology.

Cooper, K., Elster, J., Jones, M., & Kelly, R. (2001). *Optical fiber-based corrosion sensor systems for health monitoring of aging aircraft.* Paper presented at the AUTOTESTCON Proceedings, 2001. IEEE Systems Readiness Technology Conference.

Cordeiro, C. M., Franco, M. A., Chesini, G., Barretto, E. C., Lwin, R., Cruz, C. B., & Large, M. C. (2006). Microstructured-core optical fibre for evanescent sensing applications. *Opt Express, 14*(26), 13056-13066.

Cullum, B. M., & Vo-Dinh, T. (2000). The development of optical nanosensors for biological measurements. *Trends in biotechnology, 18*(9), 388-393.

Dandridge, A., Tveten, A., & Giallorenzi, T. (1981). Interferometric current sensors using optical fibres. *Electronics Letters, 17*(15), 523-525.

Dandridge, A., Tveten, A., Sigel, G., West, E., & Giallorenzi, T. (1980). Optical fibre magnetic field sensors. *Electronics Letters, 16*(11), 408-409.

Dedova, T., Volobujeva, O., Klauson, J., Mere, A., & Krunks, M. (2007). ZnO nanorods via spray deposition of solutions containing zinc chloride and thiocarbamide. *Nanoscale Research Letters, 2*(8), 391-396.

Dickey, F. M., Weichman, L. S., & Shagam, R. N. (2000). *Laser beam shaping techniques.* Paper presented at the High-Power Laser Ablation.

Docquier, N., & Candel, S. (2002). Combustion control and sensors: a review. *Progress in energy and combustion science, 28*(2), 107-150.

Durana, G., Kirchhof, M., Luber, M., Ocáriz, D., Sáez, I., Poisel, H., . . . Vázquez, C. (2009). Use of a novel fiber optical strain sensor for monitoring the vertical deflection of an aircraft flap. *Sensors Journal, IEEE, 9*(10), 1219-1225.

Dutta, J., & Hofmann, H. (2004). Self-organization of colloidal nanoparticles. *Encyclopedia of nanoscience and nanotechnology, 9*, 617-640.

Dwivedi, Y. S., Sharma, A. K., & Gupta, B. D. (2007). Influence of skew rays on the sensitivity and signal-to-noise ratio of a fiber-optic surface-plasmon-resonance sensor: a theoretical study. *Applied optics, 46*(21), 4563-4569.

Edmonson, J. M. (1991). History of the instruments for gastrointestinal endoscopy. *Gastrointest Endosc, 37*, S27-S56.

Espitia, P. J. P., Soares, N. d. F. F., dos Reis Coimbra, J. S., de Andrade, N. J., Cruz, R. S., & Medeiros, E. A. A. (2012). Zinc oxide nanoparticles: synthesis, antimicrobial activity and food packaging applications. *Food and Bioprocess Technology, 5*(5), 1447-1464.

Fabbri, F., Villani, M., Catellani, A., Calzolari, A., Cicero, G., Calestani, D., . . . Sekiguchi, T. (2014). Zn vacancy induced green luminescence on non-polar surfaces in ZnO nanostructures. *Scientific reports, 4*.

Fallah, H., Chaudhari, M., Bora, T., Harun, S., Mohammed, W., & Dutta, J. (2013). Demonstration of side coupling to cladding modes through zinc oxide nanorods grown on multimode optical fiber. *Opt Lett, 38*(18), 3620-3622.

Fallah, H., Harun, S. W., Mohammed, W. S., & Dutta, J. (2014). Excitation of core modes through side coupling to multimode optical fiber by hydrothermal growth of ZnO nanorods for wide angle optical reception. *JOSA B, 31*(9), 2232-2238.

Fan, S.-W., Srivastava, A. K., & Dravid, V. P. (2009). UV-activated room-temperature gas sensing mechanism of polycrystalline ZnO. *Applied physics letters, 95*(14), 142106.

Fischer, U. H., Haupt, M., Reinboth, C., & Just, J.-U. (2015). *Applying the principles of augmented learning to photonics laboratory work.* Paper presented at the Tenth International Topical Meeting on Education and Training in Optics and Photonics.

Giallorenzi, T. G., Bucaro, J. A., Dandridge, A., & Cole, J. H. (1986). Optical-fiber sensors challenge the competition: Resistance to corrosion and immunity to interference head the list of benefits in detecting stimuli ranging from pressure to magnetism. *Spectrum, IEEE, 23*(9), 44-50.

Giallorenzi, T. G., Bucaro, J. A., Dandridge, A., Sigel Jr, G., Cole, J. H., Rashleigh, S. C., & Priest, R. G. (1982). Optical fiber sensor technology. *Microwave Theory and Techniques, IEEE Transactions on, 30*(4), 472-511.

Giri, A. K., Saha, A., Mondal, A., Ghosh, S. C., Kundu, S., & Panda, A. B. (2015). Rectangular ZnO porous nano-plate assembly with excellent acetone sensing performance and catalytic activity. *RSC Advances, 5*(124), 102134-102142.

Gomez, J., Zubia, J., Aranguren, G., Arrue, J., Poisel, H., & Saez, I. (2009). Comparing polymer optical fiber, fiber Bragg grating, and traditional strain gauge for aircraft structural health monitoring. *Applied optics, 48*(8), 1436-1443.

Gómez, J., Zubia, J., Aranguren, G., Durana, G., Illaro, J., Sáez, I., . . . Hartl, E. (2008). *Comparing polymer optical fiber (POF), fiber Bragg gratings and traditional strain gauge for aircraft structural health monitoring.* Paper presented at the 2008 IEEE Avionics, Fiber-Optics and Photonics Technology Conference.

Gorla, C., Emanetoglu, N., Liang, S., Mayo, W., Lu, Y., Wraback, M., & Shen, H. (1999). Structural, optical, and surface acoustic wave properties of epitaxial ZnO films grown on (0112) sapphire by metalorganic chemical vapor deposition. *Journal of applied physics, 85*(5), 2595-2602.

Grattan, K., & Sun, T. (2000). Fiber optic sensor technology: an overview. *Sensors and Actuators A: Physical, 82*(1), 40-61.

Grattan, L., & Meggitt, B. (2013). *Optical fiber sensor technology: advanced applications-Bragg gratings and distributed sensors*: Springer Science & Business Media.

Hamouda, T., Peters, K., & Seyam, A.-F. M. (2012). Effect of resin type on the signal integrity of an embedded perfluorinated polymer optical fiber. *Smart materials and structures, 21*(5), 055023.

Han, Y.-G., Lee, J., & Lee, S. (2004). Discrimination of bending and temperature sensitivities with phase-shifted long-period fiber gratings depending on initial coupling strength. *Opt Express, 12*(14), 3204-3208.

Harith, Z., Irawati, N., Rafaie, H. A., Batumalay, M., Harun, S. W., Nor, R. M., & Ahmad, H. (2015). Tapered Plastic Optical Fiber Coated With Al-Doped ZnO Nanostructures for Detecting Relative Humidity. *Sensors Journal, IEEE*, *15*(2), 845-849.

Harun, S., Lim, K., Damanhuri, S., & Ahmad, H. (2011). Microfiber loop resonator based temperature sensor. *Journal of the European Optical Society-Rapid publications*, *6*.

Hayashi, N., Mizuno, Y., & Nakamura, K. (2012). Brillouin gain spectrum dependence on large strain in perfluorinated graded-index polymer optical fiber. *Opt Express*, *20*(19), 21101-21106.

Hentschel, C. (1983). Fiber optics handbook.

Hernández-Romano, I., Monzón-Hernández, D., Moreno-Hernández, C., Moreno-Hernandez, D., & Villatoro, J. (2015). Highly sensitive temperature sensor based on a polymer-coated microfiber interferometer. *Ieee Photonics Technology Letters*, *27*(24), 2591-2594.

Hey, J. (1983). From Leonardo to the Graser: light scattering in historical perspective. *S Afr J Sci*, *79*, 11-27.

Hill, K., Fujii, Y., Johnson, D. C., & Kawasaki, B. (1978). Photosensitivity in optical fiber waveguides: Application to reflection filter fabrication. *Applied physics letters*, *32*(10), 647-649.

Hocker, G. (1979). Fiber-optic sensing of pressure and temperature. *Applied optics*, *18*(9), 1445-1448.

Hodgkinson, J., & Tatam, R. P. (2012). Optical gas sensing: a review. *Measurement Science and Technology*, *24*(1), 012004.

Hoo, Y., Jin, W., Ho, H. L., Wang, D., & Windeler, R. S. (2002). Evanescent-wave gas sensing using microstructure fiber. *Optical Engineering*, *41*(1), 8-9.

Huang, J., Lan, X., Wang, H., Yuan, L., Wei, T., Gao, Z., & Xiao, H. (2012). Polymer optical fiber for large strain measurement based on multimode interference. *Opt Lett*, *37*(20), 4308-4310.

Huang, M., Yan, Y., Feng, W., Weng, S., Zheng, Z., Fu, X., & Liu, P. (2014). Controllable tuning various ratios of ZnO polar facets by crystal seed-assisted growth and their photocatalytic activity. *Crystal Growth & Design*, *14*(5), 2179-2186.

Hulanicki, A., Glab, S., & Ingman, F. (1991). Chemical sensors: definitions and classification. *Pure and Applied Chemistry*, *63*(9), 1247-1250.

Hulst, H. C., & Van De Hulst, H. (1957). *Light scattering by small particles*: Courier Corporation.

Husdi, I. R., Nakamura, K., & Ueha, S. (2004). Sensing characteristics of plastic optical fibres measured by optical time-domain reflectometry. *Measurement Science and Technology, 15*(8), 1553.

Hvedstrup Jensen, G. (1974). Temperature Dependence of the Band Gap in ZnO from Reflection Data. *physica status solidi (b), 64*(1), K51-K54.

Ihara, M., Takahiro, I., Kusunoki, T., Ohno, K., Senna, M., Isobe, T., & Konishi, M. (2002). Method for producing light-emitting substance: Google Patents.

Ishigure, T., Horibe, A., Nihei, E., & Koike, Y. (1995). High-bandwidth, high-numerical aperture graded-index polymer optical fiber. *Lightwave Technology, Journal of, 13*(8), 1686-1691.

Ismail, A. A., El-Midany, A., Abdel-Aal, E., & El-Shall, H. (2005). Application of statistical design to optimize the preparation of ZnO nanoparticles via hydrothermal technique. *Materials Letters, 59*(14), 1924-1928.

Jaisai, M., Baruah, S., & Dutta, J. (2012). Paper modified with ZnO nanorods–antimicrobial studies. *Beilstein journal of nanotechnology, 3*(1), 684-691.

Janotti, A., & Van de Walle, C. G. (2009). Fundamentals of zinc oxide as a semiconductor. *Reports on Progress in Physics, 72*(12), 126501.

Jeunhomme, L. B. (1983). Single-mode fiber optics. Principles and applications. *Optical Engineering, New York: Dekker, 1983, 1*.

Jiang, C., Kuzyk, M. G., Ding, J.-L., Johns, W. E., & Welker, D. J. (2002). Fabrication and mechanical behavior of dye-doped polymer optical fiber. *Journal of applied physics, 92*(1), 4-12.

Jing, Q., Fu, W., Li, W., Yang, H., Li, M., Ma, J., . . . Zhang, Y. (2012). Synthesis of snowflake-like multi-layered ZnO with controllable pore sizes and its photocatalytic property. *Applied surface science, 258*(8), 3604-3610.

Jo, S., Lao, J., Ren, Z., Farrer, R., Baldacchini, T., & Fourkas, J. (2003). Field-emission studies on thin films of zinc oxide nanowires. *Applied physics letters, 83*(23), 4821-4823.

Ju, S., Watekar, P. R., & Han, W.-T. (2009). *Highly sensitive temperature sensor using fiber Bragg grating on Pb/Ge-codoped fiber.* Paper presented at the National Fiber Optic Engineers Conference.

Kao, C. K. (1983). Optical Fiber Systems: Technology, Design, and Application.

Keiser, G. (2000). Optical fiber communication. *NY: McGraw-Hill*.

Kerker, M. (1969). The scattering of light: Academic Press, New York.

Kiesel, S., Peters, K., Hassan, T., & Kowalsky, M. (2007). Behaviour of intrinsic polymer optical fibre sensor for large-strain applications. *Measurement Science and Technology, 18*(10), 3144.

Kim, J. H., Kim, E. M., Andeen, D., Thomson, D., DenBaars, S. P., & Lange, F. F. (2007). Growth of Heteroepitaxial ZnO Thin Films on GaN-Buffered Al2O3 (0001) Substrates by Low-Temperature Hydrothermal Synthesis at 90° C. *Advanced Functional Materials, 17*(3), 463-471.

Kim, T.-U., Kim, J.-A., Pawar, S., Moon, J.-H., & Kim, J. H. (2010). Creation of nanoscale two-dimensional patterns of ZnO nanorods using laser interference lithography followed by hydrothermal synthesis at 90 C. *Crystal Growth & Design, 10*(10), 4256-4261.

Kołodziejczak-Radzimska, A., & Jesionowski, T. (2014). Zinc oxide—from synthesis to application: a review. *Materials, 7*(4), 2833-2881.

Kong, T., Chen, Y., Ye, Y., Zhang, K., Wang, Z., & Wang, X. (2009). An amperometric glucose biosensor based on the immobilization of glucose oxidase on the ZnO nanotubes. *Sensors and Actuators B: Chemical, 138*(1), 344-350.

Kong, Y., Yu, D., Zhang, B., Fang, W., & Feng, S. (2001). Ultraviolet-emitting ZnO nanowires synthesized by a physical vapor deposition approach. *Applied physics letters, 78*(4), 407-409.

Korolyov, V., & Potapov, V. (2012). Biomedical Fiber-Optic Temperature and Pressure Sensors. *Biomedical Engineering*, 1-4.

Koziol, K., Boskovic, B., & Yahya, N. (2011). Carbon and Oxide Nanostructures: Synthesis, Characterisation and Applications. *Columbia: Henry Dickens & Co*.

Kraft, M. (2006). VIBRATIONAL SPECTROSCOPIC SENSORS Fundamentals, Instrumentation and Applications *Optical Chemical Sensors* (pp. 117-155): Springer.

Krč, J., Zeman, M., Kluth, O., Smole, F., & Topič, M. (2003). Effect of surface roughness of ZnO: Al films on light scattering in hydrogenated amorphous silicon solar cells. *Thin Solid Films, 426*(1), 296-304.

Krebs, F. C., Thomann, Y., Thomann, R., & Andreasen, J. W. (2008). A simple nanostructured polymer/ZnO hybrid solar cell—preparation and operation in air. *Nanotechnology, 19*(42), 424013.

Kumar, S., & Swaminathan, S. (2016). *Design of liquid temperature sensor based on bending loss phenomenon of plastic optic fiber and electro-optic effect of Mach-Zehnder interferometer.* Paper presented at the SPIE Photonics Europe.

Kumar, S. A., & Chen, S. M. (2008). Nanostructured zinc oxide particles in chemically modified electrodes for biosensor applications. *Analytical Letters, 41*(2), 141-158.

Kurashima, T., Horiguchi, T., & Tateda, M. (1990). Distributed-temperature sensing using stimulated Brillouin scattering in optical silica fibers. *Opt Lett, 15*(18), 1038-1040.

Lacy, E. (1982). Fiber Optics Prentice-Hall. *Englewood Cliffs, New Jersey*, 70.

Lagakos, N., & Bucaro, J. A. (1981). Pressure desensitization of optical fibers. *Applied optics, 20*(15), 2716-2720.

Law, M. K., Bermak, A., & Luong, H. C. (2010). A sub-μmW embedded CMOS temperature sensor for RFID food monitoring application. *IEEE journal of solid-state circuits, 45*(6), 1246.

Lee, B. (2003). Review of the present status of optical fiber sensors. *Optical fiber technology, 9*(2), 57-79.

Lee, B. H., Kim, Y. H., Park, K. S., Eom, J. B., Kim, M. J., Rho, B. S., & Choi, H. Y. (2012). Interferometric fiber optic sensors. *Sensors (Basel), 12*(3), 2467-2486.

Lee, J.-R., Dhital, D., & Yoon, D.-J. (2011). Investigation of cladding and coating stripping methods for specialty optical fibers. *Optics and Lasers in Engineering, 49*(3), 324-330.

Leiner, M. J. (1991). Luminescence chemical sensors for biomedical applications: scope and limitations. *Analytica chimica acta, 255*(2), 209-222.

Li, X., Lin, S., Liang, J., Zhang, Y., Oigawa, H., & Ueda, T. (2012). Fiber-optic temperature sensor based on difference of thermal expansion coefficient between fused silica and metallic materials. *IEEE Photonics Journal, 4*(1), 155-162.

Liebsch, G., Klimant, I., Krause, C., & Wolfbeis, O. S. (2001). Fluorescent imaging of pH with optical sensors using time domain dual lifetime referencing. *analytical chemistry, 73*(17), 4354-4363.

Liedberg, B., Nylander, C., & Lunström, I. (1983). Surface plasmon resonance for gas detection and biosensing. *Sensors and Actuators, 4*, 299-304.

Liehr, S., & Krebber, K. (2012). Application of quasi-distributed and dynamic length and power change measurement using optical frequency domain reflectometry. *Sensors Journal, IEEE, 12*(1), 237-245.

Liehr, S., Lenke, P., Wendt, M., Krebber, K., Seeger, M., Thiele, E., . . . Münich, J. C. (2009). Polymer optical fiber sensors for distributed strain measurement and application in structural health monitoring. *Sensors Journal, IEEE, 9*(11), 1330-1338.

Liehr, S., Nöther, N., & Krebber, K. (2009). Incoherent optical frequency domain reflectometry and distributed strain detection in polymer optical fibers. *Measurement Science and Technology, 21*(1), 017001.

Liehr, S., Wendt, M., & Krebber, K. (2010). Distributed strain measurement in perfluorinated polymer optical fibres using optical frequency domain reflectometry. *Measurement Science and Technology, 21*(9), 094023.

Lilienfeld, P. (2004). A blue sky history. *Optics and photonics news, 15*(6), 32-39.

Lin, F.-C., Takao, Y., Shimizu, Y., & Egashira, M. (1995). Hydrogen-sensing mechanism of zinc oxide varistor gas sensors. *Sensors and Actuators B: Chemical, 25*(1), 843-850.

Lin, H., Cheng, C., Chou, Y., Huang, L., Chen, Y., & Tsen, K. (2006). Enhancement of band gap emission stimulated by defect loss. *Opt Express, 14*(6), 2372-2379.

Lipfert, J., Columbus, L., Chu, V. B., Lesley, S. A., & Doniach, S. (2007). Size and shape of detergent micelles determined by small-angle X-ray scattering. *The Journal of Physical Chemistry B, 111*(43), 12427-12438.

Lokman, A., Harun, S., Harith, Z., Rafaie, H., Nor, R., & Arof, H. (2015). Inline Mach–Zehnder interferometer with ZnO nanowires coating for the measurement of uric acid concentrations. *Sensors and Actuators A: Physical, 234*, 206-211.

Lv, R.-Q., Zhao, Y., Wang, D., & Wang, Q. (2014). Magnetic fluid-filled optical fiber Fabry–Pérot sensor for magnetic field measurement. *Photonics Technology Letters, IEEE, 26*(3), 217-219.

Lynch, D. K., & Livingston, W. C. (2001). *Color and light in nature*: Cambridge University Press.

Mahato, T., Prasad, G., Singh, B., Acharya, J., Srivastava, A., & Vijayaraghavan, R. (2009). Nanocrystalline zinc oxide for the decontamination of sarin. *Journal of hazardous materials, 165*(1), 928-932.

Mahmood, M. A., Bora, T., & Dutta, J. (2013). Studies on hydrothermally synthesised zinc oxide nanorod arrays for their enhanced visible light photocatalysis. *International Journal of Environmental Technology and Management, 16*(1-2), 146-159.

Maiman, T. H. (1960). Stimulated optical radiation in ruby.

McCorkle, D. L., Warmack, R. J., Patel, S. V., Mlsna, T., Hunter, S. R., & Ferrell, T. L. (2005). Ethanol vapor detection in aqueous environments using micro-capacitors and dielectric polymers. *Sensors and Actuators B: Chemical, 107*(2), 892-903.

McFarland, A. D., & Van Duyne, R. P. (2003). Single silver nanoparticles as real-time optical sensors with zeptomole sensitivity. *Nano Lett, 3*(8), 1057-1062.

McWilliams, K. R., & Lamb, S. (1994). Device for controlling or limiting temperature in an electric cooking appliance: Google Patents.

Mendez, A., Morse, T. F., & Mendez, F. (1990). *Applications of embedded optical fiber sensors in reinforced concrete buildings and structures.* Paper presented at the OE/FIBERS'89.

Mescia, L., & Prudenzano, F. (2013). Advances on optical fiber sensors. *Fibers, 2*(1), 1-23.

Michel, D., Xiao, F., Skillman, L., & Alameh, K. (2016). Surface Plasmon Resonance Sensor for In Situ Detection of Xanthan Gum. *Selected Topics in Quantum Electronics, IEEE Journal of, 22*(3), 1-4.

Miles, D., Cameron, P., & Mattia, D. (2015). Hierarchical 3D ZnO nanowire structures via fast anodization of zinc. *Journal of Materials Chemistry A, 3*(34), 17569-17577.

Minakawa, K., Hayashi, N., Shinohara, Y., Tahara, M., Hosoda, H., Mizuno, Y., & Nakamura, K. (2014). Wide-range temperature dependences of Brillouin scattering properties in polymer optical fiber. *Japanese Journal of Applied Physics, 53*(4), 042502.

Minnaert, M. (2013). *The nature of light and colour in the open air*: Courier Corporation.

Mishra, R., Keimasi, M., & Das, D. (2004). The temperature ratings of electronic parts. *Electronics Cooling, 10*(1), 20.

Montero, D. S., Lallana, P. C., & Vázquez, C. (2012). A polymer optical fiber fuel level sensor: Application to paramotoring and powered paragliding. *Sensors (Basel), 12*(5), 6186-6197.

Morisawa, M., & Muto, S. (2012). Plastic optical fiber sensing of alcohol concentration in liquors. *Journal of Sensors, 2012*.

Mourant, J. R., Hielscher, A. H., Eick, A. A., Johnson, T. M., & Freyer, J. P. (1998). Evidence of intrinsic differences in the light scattering properties of tumorigenic and nontumorigenic cells. *Cancer Cytopathology, 84*(6), 366-374.

Müller, J., Sönnichsen, C., Von Poschinger, H., Von Plessen, G., Klar, T., & Feldmann, J. (2002). Electrically controlled light scattering with single metal nanoparticles. *Applied physics letters, 81*(1), 171-173.

Murdock, R. C., Braydich-Stolle, L., Schrand, A. M., Schlager, J. J., & Hussain, S. M. (2008). Characterization of nanomaterial dispersion in solution prior to in vitro exposure using dynamic light scattering technique. *Toxicological Sciences, 101*(2), 239-253.

Narsaiah, K., Jha, S. N., Bhardwaj, R., Sharma, R., & Kumar, R. (2012). Optical biosensors for food quality and safety assurance—a review. *Journal of food science and technology, 49*(4), 383-406.

Near, R., Hayden, S., & El-Sayed, M. (2012). Extinction vs absorption: which is the indicator of plasmonic field strength for silver nanocubes? *The Journal of Physical Chemistry C, 116*(43), 23019-23026.

Nylander, C., Liedberg, B., & Lind, T. (1982). Gas detection by means of surface plasmon resonance. *Sensors and Actuators, 3*, 79-88.

Oehme, I., & Wolfbeis, O. S. (1997). Optical sensors for determination of heavy metal ions. *Microchimica Acta, 126*(3-4), 177-192.

Ohno, H., Naruse, H., Kihara, M., & Shimada, A. (2001). Industrial applications of the BOTDR optical fiber strain sensor. *Optical fiber technology, 7*(1), 45-64.

Olmo, I. F., Chacon, E., & Irabien, A. (2001). Influence of lead, zinc, iron (III) and chromium (III) oxides on the setting time and strength development of Portland cement. *Cement and Concrete Research, 31*(8), 1213-1219.

Patel, N., Patel, P., & Vaishnav, V. (2003). Indium tin oxide (ITO) thin film gas sensor for detection of methanol at room temperature. *Sensors and Actuators B: Chemical, 96*(1), 180-189.

Pauporté, T., & Lincot, D. (2000). Electrodeposition of semiconductors for optoelectronic devices: results on zinc oxide. *Electrochimica Acta, 45*(20), 3345-3353.

Peng, L., Zhai, J., Wang, D., Zhang, Y., Wang, P., Zhao, Q., & Xie, T. (2010). Size-and photoelectric characteristics-dependent formaldehyde sensitivity of ZnO irradiated with UV light. *Sensors and Actuators B: Chemical, 148*(1), 66-73.

Peters, K. (2010). Polymer optical fiber sensors—a review. *Smart materials and structures, 20*(1), 013002.

Polsongkram, D., Chamninok, P., Pukird, S., Chow, L., Lupan, O., Chai, G., . . . Schulte, A. (2008). Effect of synthesis conditions on the growth of ZnO nanorods via hydrothermal method. *Physica B: Condensed Matter, 403*(19), 3713-3717.

Purica, M., Budianu, E., & Rusu, E. (2001). ZnO thin films on semiconductor substrate for large area photodetector applications. *Thin Solid Films, 383*(1), 284-286.

Puyol, M., Villuendas, F., Domínguez, C., Cadarso, V., Llobera, A., Salinas, I., . . . Alonso, J. (2005). Absorbance-based integrated optical sensors *Frontiers in Chemical Sensors* (pp. 1-44): Springer.

Rahim, H. R. B. A., Manjunath, S., Fallah, H., Thokchom, S., Harun, S. W., Mohammed, W. S., . . . Dutta, J. (2016). Side coupling of multiple optical channels by spiral patterned zinc oxide coatings on large core plastic optical fibers. *IET Micro & Nano Letters, 11*(2), 122-126.

Rahman, H. A., Harun, S. W., Saidin, N., Yasin, M., & Ahmad, H. (2012). Fiber optic displacement sensor for temperature measurement. *Sensors Journal, IEEE, 12*(5), 1361-1364.

Rahman, H. A., Harun, S. W., Yasin, M., & Ahmad, H. (2012). Fiber-optic salinity sensor using fiber-optic displacement measurement with flat and concave mirror. *Selected Topics in Quantum Electronics, IEEE Journal of, 18*(5), 1529-1533.

Rajan, G. (2015). *Optical Fiber Sensors: Advanced Techniques and Applications* (Vol. 36): CRC press.

Rajan, G., Liu, B., Luo, Y., Ambikairajah, E., & Peng, G.-D. (2013). High sensitivity force and pressure measurements using etched singlemode polymer fiber Bragg gratings. *Sensors Journal, IEEE, 13*(5), 1794-1800.

Ramakrishnan, M., Rajan, G., Semenova, Y., & Farrell, G. (2016). Overview of Fiber Optic Sensor Technologies for Strain/Temperature Sensing Applications in Composite Materials. *Sensors (Basel), 16*(1), 99.

Rasmussen, J. W., Martinez, E., Louka, P., & Wingett, D. G. (2010). Zinc oxide nanoparticles for selective destruction of tumor cells and potential for drug delivery applications. *Expert opinion on drug delivery, 7*(9), 1063-1077.

Rayleigh, L. (1917). On the reflection of light from a regularly stratified medium. *Proceedings of the Royal Society of London. Series A, Containing Papers of a Mathematical and Physical Character, 93*(655), 565-577.

Repins, I., Contreras, M. A., Egaas, B., DeHart, C., Scharf, J., Perkins, C. L., . . . Noufi, R. (2008). 19· 9%-efficient ZnO/CdS/CuInGaSe2 solar cell with 81· 2% fill factor. *Progress in Photovoltaics: Research and applications, 16*(3), 235-239.

Rothmaier, M., Luong, M. P., & Clemens, F. (2008). Textile pressure sensor made of flexible plastic optical fibers. *Sensors (Basel), 8*(7), 4318-4329.

Saito, Y., Ichikawa, O., & Oshima, T. (1987). Waterproof optical fiber cable and method of the production thereof: Google Patents.

Samarasekara, P., Yapa, N., Kumara, N., & Perera, M. (2007). CO2 gas sensitivity of sputtered zinc oxide thin films. *Bulletin of Materials Science, 30*(2), 113-116.

Sanjeev, S., & Kekuda, D. (2015). *Effect of Annealing Temperature on the Structural and Optical Properties of Zinc Oxide (ZnO) Thin Films Prepared by Spin Coating Process.* Paper presented at the IOP Conference Series: Materials Science and Engineering.

Sathitanon, N., & Pullteap, S. (2007). A fiber optic interferometric sensor for dynamic measurement. *measurements, 7*, 8.

Sberveglieri, G. (2012). *Gas sensors: principles, operation and developments*: Springer Science & Business Media.

Schmidt, R. R., & Notohardjono, B. D. (2002). High-end server low-temperature cooling. *IBM Journal of Research and Development, 46*(6), 739-751.

Schroeder, R. J., Yamate, T., & Udd, E. (1999). *High pressure and temperature sensing for the oil industry using fiber Bragg gratings written onto side hole single mode fiber*. Paper presented at the PROCEEDINGS-SPIE THE INTERNATIONAL SOCIETY FOR OPTICAL ENGINEERING.

Seaman, W. E. (1997). Electronically controlled container for storing temperature sensitive material: Google Patents.

Shan, C., Liu, Z., & Hark, S. (2008). Temperature dependent photoluminescence study on phosphorus doped ZnO nanowires. *Applied physics letters, 92*(7), 73103-73103.

Shenhav, A., Brodie, Z., Beiderman, Y., Garcia, J., Mico, V., & Zalevsky, Z. (2013). Optical sensor for remote estimation of alcohol concentration in blood stream. *Optics communications, 289*, 149-157.

Shinde, S., Shinde, P., Bhosale, C., & Rajpure, K. (2008). Optoelectronic properties of sprayed transparent and conducting indium doped zinc oxide thin films. *Journal of Physics D: Applied Physics, 41*(10), 105109.

Silva-López, M., Fender, A., MacPherson, W. N., Barton, J. S., Jones, J. D., Zhao, D., . . . Bennion, I. (2005). Strain and temperature sensitivity of a single-mode polymer optical fiber. *Opt Lett, 30*(23), 3129-3131.

Singh, R., & Riess, F. (2001). The 1930 Nobel prize for physics: a close decision? *Notes and Records of the Royal Society, 55*(2), 267-283.

Stanković, A., Veselinović, L., Škapin, S., Marković, S., & Uskoković, D. (2011). Controlled mechanochemically assisted synthesis of ZnO nanopowders in the presence of oxalic acid. *Journal of materials science, 46*(11), 3716-3724.

Stefani, A., Andresen, S., Yuan, W., & Bang, O. (2012). Dynamic characterization of polymer optical fibers. *Sensors Journal, IEEE, 12*(10), 3047-3053.

Sugaya, M., Murai, F., Kaneko, Y., Kanetomo, M., Hirasawa, S., Watanabe, T., . . . Kuroda, K. (2002). Substrate temperature control system and method for controlling temperature of substrate: Google Patents.

Sugunan, A., Warad, H. C., Boman, M., & Dutta, J. (2006). Zinc oxide nanowires in chemical bath on seeded substrates: role of hexamine. *Journal of Sol-Gel Science and Technology, 39*(1), 49-56.

Szustakowski, M., Ciurapinski, W., Palka, N., & Zyczkowski, M. (2001). *Recent development of fiber optic sensors for perimeter security.* Paper presented at the Security Technology, 2001 IEEE 35th International Carnahan Conference on.

Takaki, S. (1998). Temperature sensor for medical application: Google Patents.

Tam, K., Cheung, C., Leung, Y., Djurišic, A., Ling, C., Beling, C., . . . Phillips, D. (2006). Defects in ZnO nanorods prepared by a hydrothermal method. *The Journal of Physical Chemistry B, 110*(42), 20865-20871.

Tang, Z., Wong, G. K., Yu, P., Kawasaki, M., Ohtomo, A., Koinuma, H., & Segawa, Y. (1998). Room-temperature ultraviolet laser emission from self-assembled ZnO microcrystallite thin films. *Applied physics letters, 72*(25), 3270-3272.

Tangonan, G. L., Persechini, D., Morrison, R., & Wysocki, J. (1980). Current sensing with metal-coated multimode optical fibres. *Electronics Letters, 16*(25), 958-959.

Tyler, S. W., Selker, J. S., Hausner, M. B., Hatch, C. E., Torgersen, T., Thodal, C. E., & Schladow, S. G. (2009). Environmental temperature sensing using Raman spectra DTS fiber-optic methods. *Water Resources Research, 45*(4).

van Eijkelenborg, M. A., Large, M. C., Argyros, A., Zagari, J., Manos, S., Issa, N. A., . . . de Sterke, C. M. (2001). Microstructured polymer optical fibre. *Opt Express, 9*(7), 319-327.

Vanheusden, K., Seager, C., Warren, W. t., Tallant, D., & Voigt, J. (1996). Correlation between photoluminescence and oxygen vacancies in ZnO phosphors. *Applied physics letters, 68*(3), 403-405.

Vanheusden, K., Warren, W., Seager, C., Tallant, D., Caruso, J., Hampden-Smith, M., & Kodas, T. (1996). *Nature of the green luminescent center in zinc oxide.* Paper presented at the MRS Proceedings.

Vanheusden, K., Warren, W., Seager, C., Tallant, D., Voigt, J., & Gnade, B. (1996). Mechanisms behind green photoluminescence in ZnO phosphor powders. *Journal of applied physics, 79*(10), 7983-7990.

Venkatesh, P. S., & Jeganathan, K. (2013). Investigations on the growth and characterization of vertically aligned zinc oxide nanowires by radio frequency magnetronsputtering. *Journal of Solid State Chemistry, 200*, 84-89.

Vergés, M. A., Mifsud, A., & Serna, C. (1990). Formation of rod-like zinc oxide microcrystals in homogeneous solutions. *Journal of the Chemical Society, Faraday Transactions, 86*(6), 959-963.

Vogler, D., & Sigrist, M. (2006). Near-infrared laser based cavity ringdown spectroscopy for applications in petrochemical industry. *Applied Physics B, 85*(2-3), 349-354.

Wahab, R., Kim, Y.-S., Mishra, A., Yun, S.-I., & Shin, H.-S. (2010). Formation of ZnO micro-flowers prepared via solution process and their antibacterial activity. *Nanoscale Research Letters, 5*(10), 1675-1681.

Wang, L., Kang, Y., Liu, X., Zhang, S., Huang, W., & Wang, S. (2012). ZnO nanorod gas sensor for ethanol detection. *Sensors and Actuators B: Chemical, 162*(1), 237-243.

Wang, M., & Zhang, L. (2009). The influence of orientation on the photoluminescence behavior of ZnO thin films obtained by chemical solution deposition. *Materials Letters, 63*(2), 301-303.

Wang, P., Semenova, Y., & Farrell, G. (2008). Temperature dependence of macrobending loss in all-fiber bend loss edge filter. *Optics communications, 281*(17), 4312-4316.

Wang, P., Semenova, Y., Wu, Q., Zheng, J., & Farrell, G. (2010). Temperature performance of a macrobending single-mode fiber-based refractometer. *Applied optics, 49*(10), 1744-1749.

Wang, W., Wu, N., Tian, Y., Niezrecki, C., & Wang, X. (2010). Miniature all-silica optical fiber pressure sensor with an ultrathin uniform diaphragm. *Opt Express, 18*(9), 9006-9014.

Wang, X., Summers, C. J., & Wang, Z. L. (2004). Large-scale hexagonal-patterned growth of aligned ZnO nanorods for nano-optoelectronics and nanosensor arrays. *Nano Lett, 4*(3), 423-426.

Wang, Z. L. (2004). Zinc oxide nanostructures: growth, properties and applications. *Journal of Physics: Condensed Matter, 16*(25), R829.

Warren-Smith, S. C., Nguyen, L. V., Lang, C., Ebendorff-Heidepriem, H., & Monro, T. M. (2016). Temperature sensing up to 1300° C using suspended-core microstructured optical fibers. *Opt Express, 24*(4), 3714-3719.

Weng, J., Tan, H., Wang, X., Ma, Y., Hu, S., & Wang, X. (2006). Optical-fiber interferometer for velocity measurements with picosecond resolution. *Applied physics letters, 89*(11), 111101.

Whittaker, P. (1998). Iron and zinc interactions in humans. *The American journal of clinical nutrition, 68*(2), 442S-446S.

Wiederrecht, G. (2010). *Handbook of nanoscale optics and electronics*: Academic Press.

Willander, M., Nur, O., Sadaf, J. R., Qadir, M. I., Zaman, S., Zainelabdin, A., . . . Hussain, I. (2010). Luminescence from zinc oxide nanostructures and polymers and their hybrid devices. *Materials, 3*(4), 2643-2667.

Witt, J., Schukar, M., & Krebber, K. (2008). Medicinal textiles with integrated polymer-optical fibers for respiration monitoring. *Tm-Technisches Messen, 75*(12), 670-677.

Wood, A. D., Stankovic, J. A., Virone, G., Selavo, L., He, Z., Cao, Q., . . . Stoleru, R. (2008). Context-aware wireless sensor networks for assisted living and residential monitoring. *Network, IEEE, 22*(4), 26-33.

Woyessa, G., Fasano, A., Stefani, A., Markos, C., Nielsen, K., Rasmussen, H. K., & Bang, O. (2016). Single mode step-index polymer optical fiber for humidity insensitive high temperature fiber Bragg grating sensors. *Opt Express, 24*(2), 1253-1260.

Woyessa, G., Nielsen, K., Stefani, A., Markos, C., & Bang, O. (2016). Temperature insensitive hysteresis free highly sensitive polymer optical fiber Bragg grating humidity sensor. *Opt Express, 24*(2), 1206-1213.

Wu, Y., Lim, C., Fu, S., Tok, A., Lau, H., Boey, F., & Zeng, X. (2007). Surface modifications of ZnO quantum dots for bio-imaging. *Nanotechnology, 18*(21), 215604.

Xiang, B., Wang, P., Zhang, X., Dayeh, S. A., Aplin, D. P., Soci, C., . . . Wang, D. (2007). Rational synthesis of p-type zinc oxide nanowire arrays using simple chemical vapor deposition. *Nano Lett, 7*(2), 323-328.

Xu, J., Pan, Q., & Tian, Z. (2000). Grain size control and gas sensing properties of ZnO gas sensor. *Sensors and Actuators B: Chemical, 66*(1), 277-279.

Xu, S., & Wang, Z. L. (2011). One-dimensional ZnO nanostructures: solution growth and functional properties. *Nano Research, 4*(11), 1013-1098.

Yariv, A., & Winsor, H. V. (1980). Proposal for detection of magnetic fields through magnetostrictive perturbation of optical fibers. *Opt. Lett, 5*(3), 87-89.

Yebo, N. A., Lommens, P., Hens, Z., & Baets, R. (2010). An integrated optic ethanol vapor sensor based on a silicon-on-insulator microring resonator coated with a porous ZnO film. *Opt Express, 18*(11), 11859-11866.

Yi, G.-C., Wang, C., & Park, W. I. (2005). ZnO nanorods: synthesis, characterization and applications. *Semiconductor Science and Technology, 20*(4), S22.

Yokota, M., Okada, T., & Yamaguchi, I. (2007). An optical sensor for analysis of soil nutrients by using LED light sources. *Measurement Science and Technology, 18*(7), 2197.

Zhang, H., Yang, D., Ma, X., Ji, Y., Xu, J., & Que, D. (2004). Synthesis of flower-like ZnO nanostructures by an organic-free hydrothermal process. *Nanotechnology, 15*(5), 622.

Zhang, W., Webb, D. J., & Peng, G.-D. (2012). Investigation into time response of polymer fiber Bragg grating based humidity sensors. *Journal of lightwave technology, 30*(8), 1090-1096.

Zhang, Z., Grattan, K., & Palmer, A. (1992). Fiber optic temperature sensor based on the cross referencing between blackbody radiation and fluorescence lifetime. *Review of scientific Instruments, 63*(5), 3177-3181.

Zhang, Z. F., & Tao, X. M. (2013). Intrinsic temperature sensitivity of fiber Bragg gratings in PMMA-based optical fibers. *Photonics Technology Letters, IEEE, 25*(3), 310-312.

Ziemann, O., Daum, W., Bräuer, A., Schlick, J., & Frank, W. (2000). *Results of a German 6.000 hours accelerated aging test of PMMA POF and consequences for the practical use of POF.* Paper presented at the Proceedings of the 9th International Conference on Plastic Optical Fibres, Boston.

Ziemann, O., Krauser, J., Zamzow, P. E., & Daum, W. (2008a). POF handbook. *Springer*.

Ziemann, O., Krauser, J., Zamzow, P. E., & Daum, W. (2008b). *POF handbook: optical short range transmission systems*: Springer Science & Business Media.

Zubia, J., & Arrue, J. (2001). Plastic optical fibers: An introduction to their technological processes and applications. *Optical fiber technology, 7*(2), 101-140.

Zvyagin, A. V., Zhao, X., Gierden, A., Sanchez, W., Ross, J. A., & Roberts, M. S. (2008). Imaging of zinc oxide nanoparticle penetration in human skin in vitro and in vivo. *Journal of biomedical optics, 13*(6), 064031-064031-064039.

LIST OF PUBLICATIONS, PAPERS PRESENTED AND PATENTS

Journal Publications (ISI)

1) **Rahim, H. R. B. A**., Manjunath, S., Fallah, H., Thokchom, S., Harun, S. W., Hornyak. L. G., Mohammed, W. S., & Dutta, J. (2016). Side coupling of multiple optical channels by spiral patterned zinc oxide coatings on large core plastic optical fibers. *IET Micro & Nano Letters*, *11*(2), 122-126.

2) **Rahim, H. R. B. A**, Lokman. M. Q, Harun. S. W., Hornyak. L. G., Mohammed, W. S., & Dutta, J. (2016). Applied Light Side Coupling With Optimized Spiral Patterned Zinc Oxide Nanorod Coatings for Multiple Optical Channel Alcohol Vapor Sensing. *Journal of Nanophotonics, SPIE*.

3) **Rahim, H. R. B. A**, Lokman. M. Q, Harun. S. W., Mohammed, W. S., & Dutta, J. (2017), Temperature Sensing By Side Coupling Of Light Through Zinc Oxide Nanorods On Optical Fibers, *Elsevier: Sensors and Actuators A: Physical* 257 (2017) 15–19.

4) **Rahim, H. R. B. A, H**., Irawati, N., Rafaie, H. A., Ahmad, H., Harun, S. W., & Nor, R. M. (2015). Detection Of Different Concentrations Of Uric Acid Using Tapered Silica Optical Sensor Coated With Zinc Oxide (ZnO). *Jurnal Teknologi, 74(8).*

5) Lokman, M. Q., **Rahim, H. R. B. A**., Harun, S. W., Hornyak, G. L., & Mohammed, W. S. (2016). Light backscattering (eg reflectance) by ZnO nanorods on tips of plastic optical fibres with application for humidity and alcohol vapour sensing. *Micro & Nano Letters*, *11*(12), 832-836.

6) M. Q. Lokman**, H. R. A. Rahim**, M. Yasin, Z. Jusoh, S. W. Harun. (2016), Evaluation of Light Backscattering by Zinc Oxide Nanorods on Fiber End of Silica Optical Fiber, *Journal of Optoelectronics and Advanced Materials – Rapid Communications*, 10 (11-12), 885 – 888.

7) A. R. Muhammad, M. T. Ahmad, R. Zakaria, **H. R. A. Rahim**, S. F. A. Z. Yusoff, K. S. Hamdan, H. H. M. Yusof, H. Arof, S. W. Harun (2017), Q-Switching Pulse Operation in 1.5-µm Region Using Copper Nanoparticles as Saturable Absorber, *Chinese Physical Letter*, 34(3), 034205-1- 4.

Papers Presented at Conferences

1) **Rafis, H**., Irawati, N., Rafaie, H. A., Ahmad, H., Harun, S. W., & Nor, R. M. "Detection of Different Concentrations of Uric Acid Using Tapered Silica Optical Sensor Coated with Zinc Oxide (ZnO)", Laser Technology and Optic Symposium 2014 (LATOS 2014), Universiti Teknologi Malaysia (UTM).

2) **H. Rafis**, S. Manjunath, Hoorieh Fallah, S.W.Harun, Waleed S. Mohammed, G. Louis Hornyak, Joydeep Dutta "Spiral Structured Growth of ZnO on Plastic Optical Fiber Towards Light Side Coupling ", International Symposium on Modern Optics and Its Applications (ISMOA 2015) in Bandung, Indonesia (2015).

3) **Rafis, A. R. H**., Sulaima, W. H., & Waleed, S. M. (2016, November). Improved optical side coupling efficiency by spiral patterned zinc oxide nanorod coatings on large core plastic optical fiber. In Second International Seminar on Photonics, Optics, and Its Applications *(ISPhOA 2016)* (pp. 101500T-101500T). International Society for Optics and Photonics, SPIE. (1st Poster Award)

4) Pandey, C. A., **Rahim, R**., Manjunath, S., Hornyak, G. L., & Mohammed, W. S. (2015, July). Synthesis and characterization of hydrothermally grown zinc oxide (ZnO) nanorods for optical waveguide application. In International Conference on Photonics Solutions 2015 (pp. 96590X-96590X). International Society for Optics and Photonics, SPIE.

5) **H. Rafis**, S.W.Harun, Waleed S. Mohammed "Multiple Optical Channel Alcohol Vapor Sensing in Visible Wavelength" 2016 Research and Innovation Competition Week, 15-17 Mac 2016. (Silver Medal).

6) S.Thokchom, D. Lourembam , R. Borgohain , **H. R. B. A. Rahim**, Waleed S. M, S. Baruah, ZnS coated ZnO nano-rods on Optical fiber for Gas sensing, In International Conference on Advances Nanotechnology 2017 (iCAN2017), Sustainable Nanotechnology Organization.

Patents

1) Coated Plastic Optical Fiber (PI 2016701346), University of Malaya, Intellectual Properties of Malaysia (2016).

2) Multiple Channel Optical Sensing towards Light Side Coupling, University of Malaya, Intellectual Properties of Malaysia (2016).

3) A Backscattering Light in Optical Sensor System, University of Malaya, Intellectual Properties of Malaysia (2016).